



Novel Wave Phenomena in Classical Vibrations

Yao-Ting Wang

A Thesis submitted to The University of Birmingham
for the Degree of Doctor of Philosophy

Metamaterial Research Centre
School of Physics and Astronomy
College of Engineering and Physical Science
The University of Birmingham

July 2017

UNIVERSITY OF
BIRMINGHAM

University of Birmingham Research Archive

e-theses repository

This unpublished thesis/dissertation is copyright of the author and/or third parties. The intellectual property rights of the author or third parties in respect of this work are as defined by The Copyright Designs and Patents Act 1988 or as modified by any successor legislation.

Any use made of information contained in this thesis/dissertation must be in accordance with that legislation and must be properly acknowledged. Further distribution or reproduction in any format is prohibited without the permission of the copyright holder.

Contents

Abstract	i
List of Publications	iii
Declaration	iv
List of Figures	v
List of Symbols & Abbreviations	viii
Acknowledgement	xi
Chapter 1 Introduction	1
1-1: Background and Motivation	1
1-2: Overview of Thesis.....	3
Chapter 2 Literature Reviews	4
2-1: Berry Phase.....	4
2-1.1: Brief Mathematical Review for Topology	4
2-1.2: Basic Concepts of Berry Phase.....	5
2-1.3: Berry Phase and Chern Number in Crystalline Solids	9
2-1.4: Bulk-Edge Correspondence.....	13
2-2: Graphene and Topological Insulator	14
2-2.1: Tight-Binding Description of Graphene.....	14
2-2.2: Flat Edge States in Graphene Nano-Ribbon (GNR).....	18
2-2.3: Rashba and Dresselhaus Spin-Orbit Coupling	21
2-2.4: Haldane Model	23
2-2.5: Kane-Mele Model.....	26

2-3: Z_2 Topological Invariant.....	30
2-3.1: Z_2 Invariant in the KM Model.....	30
2-3.2: Kramers Theorem.....	32
2-3.3: Time-Reversal Polarisation and Z_2 Invariant	32
2-3.4: Z_2 Invariant in Three Dimensions and Fu-Kane-Mele (FKM) Model	38
2-4: Parity-Time Symmetric Physics	42
2-4.1: Parity and Time-Reversal Symmetry	42
2-4.2: PT Symmetric System in Quantum Mechanics.....	44
2-4.3: PT Symmetric System in Optics and Acoustics	47
2-4.4: Exceptional Points and Rings.....	53
2-5: Chapter Summary.....	58
Chapter 3 Novel Phenomena in Normal Spring-Mass Systems	61
3-1: Mechanical Graphene.....	61
3-2: Topological Mechanical Waves	66
3-3: Effective Spin-Orbit Coupling in Mechanical Graphene	77
3-4: Mechanic Spin-Hall Effect.....	83
3-5: Chapter Summary.....	88
Chapter 4 Topological Elasticity	89
4-1: Introduce to Elastic Waves.....	89
4-2: Topological Shear Modes.....	94
4-3: Elastic Topological Insulators	102
4-4: Chapter Summary.....	110

Chapter 5 Rotation Induced PT Symmetric Acoustics	112
5-1: Introduction	112
5-2: Rotation Induced Dispersion	114
5-3: Pairs of Exceptional Rings	123
5-4: Chapter Summary.....	129
Chapter 6 Conclusion and Future Work	131
6-1: Conclusion.....	131
6-2: Future Work.....	132
Bibliography	137

Abstract

Since the first topological phase transition was proposed by Kosterlitz and Thouless in 1973, it has opened a new era in condensed-matter physics and expanded physicists' understanding in material classification. In the meantime, due to the progress on the sample preparation, graphene has attracted great attentions because it has some fascinating phenomena such as the exhibition of Dirac degeneracies. As the spin-orbit coupling is considered, graphene becomes the first feasible platform to study spintronics in a real two-dimensional material. Aside from that, inspired by Haldane's influential model, quantum spin Hall effects, which exist one-way reflection-free transports along the truncated boundaries for both spin degree of freedom, was predicted in graphene if only taking intrinsic spin-orbit coupling into account. Having been significantly successful, the development of topological quantum matters prompts the exploration of topological phenomena within other physical systems. Particularly in photonics, several exciting results have been discovered like photonic counterpart of topological insulators or Weyl semimetals. However, for elastic solids, its complexity in theoretical analysis and experimental realisation slows down the exploration of corresponding topological nature. Here, from discrete spring-mass systems to continuous elastic solids, we analytically and numerically discuss the possibility of achieving topological phases. Originating from time-reversal symmetry breaking via applying external fields, a unidirectional and backscattering-immune edge state arises owing to the topological protection. Also, the proposed arguments are verified by numerical calculation of practical mechanical crystals and elastic composites. We believe these studies pave the way for the future researches in topological elasticity.

On the other hand, in the past decades, the requirement of Hermiticity for a Hamiltonian

has been renewed by another discipline called parity-time (PT) symmetry. PT symmetry, which is a weaker restriction than Hermiticity, allows real eigenvalues in a non-Hermitian Hamiltonian. However, it is challenging to introduce the PT condition into quantum mechanical systems. An alternative setup consisting of two coupled gain/loss optical channels was studied because of the similar mathematical expression between quantum and optic systems under paraxial approximation. In addition, at certain scenarios, PT symmetric phase experiences spontaneous symmetry breaking, resulting in the emergence of exceptional points that possesses infinite group velocity. Note that the group velocity for a non-Hermitian system is no longer stands for the energy flow, since it is invalid for the law of energy conservation in an open system. In this thesis, we consider an acoustic metamaterial made of periodically arranged spinning cylinders. By virtue of the rotational Doppler effects, the dispersion relation near the rotating velocity of rods is significantly influenced by the rotation. The frequency shifts cause a PT symmetric Hamiltonian so that, at specific points, the spontaneous PT symmetry breaking emerges and exceptional points arise. Lastly a possible setup is discussed for the future experimental realisation.

List of Publications

1. **Y. T. Wang**, K. H. Fung, D. Zhao, S. Zhang, Z. Q. Zhang, C. T. Chan, “Pairs of Exceptional Rings in Acoustic Metamaterials Made of Spinning Cylinders”, *in preparation*
2. Y. W. Tsai, **Y. T. Wang**, P. G. Luan, S. Zhang, “Topological Shear Waves in a Phononic Crystal”, *in preparation*
3. **Y. T. Wang** and S. Zhang, “Elastic Spin-Hall effect in Mechanical Graphene”, *New J. Phys.* Vol. 18, 113014 (2016)
4. **Y. T. Wang**, P. G. Luan, S. Zhang, “Coriolis force induced topological order for classical vibration”, *New J. Phys.* Vol. 17, 073031. (2015)

Declaration

I hereby declare that I am the sole author of this thesis, which is collection of my own researches during the PhD career. Several new discoveries are included within chapters three to five, and there exists no plagiarism and fraud throughout the entire dissertation.

Although I independently completed the most of studies, the results regarding topological mechanical edge states and topological shear modes were achieved in collaboration with Dr. Pi-Gang Luan and Ms. Ya-Wen Tsai during their visit at University of Birmingham. Also, the investigations in Chapter five were accomplished under the supervision of Professor Kin Hung Fung, Zhao-Qing Zhang, and Che Ting Chan in the course of my stay as a visiting internship student at Hong Kong University of Science and Technology.

List of Figures

Fig. 2.1: Hairy-ball theorem.....	5
Fig. 2.2: Poincaré Sphere.....	8
Fig. 2.3: Bulk-edge Correspondence.....	14
Fig. 2.4: The geometry of graphene.....	15
Fig. 2.5: First Brillouin zone of graphene.....	18
Fig. 2.6: Labelling approach for zigzag graphene nanoribbon.....	20
Fig. 2.7: Edge states of graphene.....	21
Fig. 2.8: Spin locking effect for Dresselhaus and Rashba SOC.....	23
Fig. 2.9: Haldane model.....	25
Fig. 2.10: Kane-Mele Model.....	28
Fig. 2.11: Edge States with Distinct Z_2 index.....	29
Fig. 2.12: The zeros of $P(k)$ in the topological insulating phase.....	31
Fig. 2.13: Two evolution types of TRP.....	37
Fig. 2.14: Schematic figures of TRIMs.....	38
Fig. 2.15: Bulk band structure of 3D topological insulators.....	40
Fig. 2.16: Projected band structures of 3D topological insulators.....	41
Fig. 2.17: Energy levels of the Hamiltonian (2-75).....	45
Fig. 2.18: Schematic figure of coupled gain-loss waveguides.....	48
Fig. 2.19: Schematic picture of the acoustic PT channel.....	49
Fig. 2.20: Spectra and EPs in PT acoustics.....	52
Fig. 2.21: Experimental setup and phase diagram of high-order EPs.....	54
Fig. 2.22: Phase rigidity and Riemann surface.....	56

Fig. 2.23: A ring of EPs.	57
Fig. 3.1: Mechanical graphene.....	63
Fig. 3.2: Edge states of mechanical graphene.....	66
Fig. 3.3: Projected frequency bands for a mass-spring ribbon (P breaking).....	67
Fig. 3.4: Projected frequency bands for a mass-spring ribbon (TR breaking).....	69
Fig. 3.5: Chern number calculation for bands.....	70
Fig. 3.6: Snapshots of edge states in a spring-mass strip.....	71
Fig. 3.7: Gapless edge states in mechanical graphene (zigzag).....	75
Fig. 3.8: Gapless edge states in mechanical graphene (braided).....	76
Fig. 3.9: Mechanical Graphene with transverse elastic constants.	79
Fig. 3.10: Phonon dispersion and spin texture.....	82
Fig. 3.11: A schematic sketch of the initial displacement distribution.....	84
Fig. 3.12: Elastic spin Hall effect.....	85
Fig. 3.13: The cavity-phononic crystal.	88
Fig. 4.1: A 2D gyromagnetic phononic crystal.....	96
Fig. 4.2: Bulk band diagrams and gapless edge states (2D).	99
Fig. 4.3: Bulk band diagrams and gapless edge states (Finite Thickness).....	101
Fig. 4.4: One-way transport of shear modes.	102
Fig. 4.5: Topologically non-trivial bandgap and gapless edge states.	107
Fig. 4.6: TR Symmetry-protected edge states.....	108
Fig. 4.7: Elastic metamaterials.....	109
Fig. 5.1: A schematic plot and low-frequency dispersion.	116
Fig. 5.2: The approximate values:.....	119
Fig. 5.3: Transmittance spectrum.....	125
Fig. 5.4: A pair of ERs.	127
Fig. 5.5: Phase rigidity.....	128

Fig. 5.6: Another pair of ERs.....	129
Fig. 6.1: A mechanical Benzene.	133

Lists of Symbols & Abbreviations

List of Symbols

Symbols	Meanings
χ	Euler characteristic
\mathcal{K}	Gaussian curvature
g	Genus
π	Circumference/diameter
i	Imaginary unit
\hbar	Planck constant
H	Hamiltonian
Hat “^” on any character	Operators
any character in “ \rangle ”	Ket in Dirac notation
any character in “ \langle ”	Bra in Dirac notation
e^{\square} or $\exp[\square]$	Natural exponential function
ε_n	Energy eigenvalues
γ	Berry phase
\mathcal{A}	Berry connection
Ω	Berry curvature
\mathcal{R}	Arbitrary parameter space
\mathbf{A}	Vector potential
\mathbf{B}	Magnetic field
Φ_B	Magnetic flux
θ_{solid}	Solid angle
e	Electronic charge
m	Electronic mass
V	Potential energy
j_H	Hall current
G_H	Hall conductance
C_n	Chern/TKNN number
k	wavevector
\mathbf{E}	Electric field
v_n	Anomalous velocity
\mathbf{R}	Distance of nearest neighbour
a	Lattice constant
$c^\dagger (c)$	Creation(annihilation) operator
σ_x	x component of Pauli matrix
σ_y	y component of Pauli matrix
σ_z	z component of Pauli matrix
μ_B	Bohr magneton

t	hopping parameter/time
ϕ	Phase of hopping parameter
m_{eff}	Effective mass term
λ_{SO}	Strength of intrinsic SOC
λ_D	Strength of Dresselhaus SOC
λ_R	Strength of Rashba SOC
$\hat{\Theta}$	Time-reversal operator
$\{v_0; v_1 v_2 v_3\}$	Z_2 topological indices
$\Gamma_{n_1 n_2 n_3}$	Time-reversal invariant momenta
$\hat{\Pi}$	Parity/inversion operator
\mathbf{r}	Position (operator)
\mathbf{p}	Momentum (operator)
n	Refraction index
β	Propagation constant
κ	Coupling coefficient
ρ	Density
B	Bulk modulus
S	Scattering matrix
Γ_1, Γ_2	Dissipation term
r_j	Phase rigidity
ξ, η	Dynamic distances for rigid bodies
M	Mass of a bead
K	Elastic constant of a spring
ω	Angular frequency
Q	Charge
\mathbf{W}	Angular velocity
ρ_c	Stokes' parameter
u_{ik}	Strain tensor
σ_{ik}	Stress tensor
λ, μ	Lamé constants
p	pressure
$u_i, i = x, y, z$	Dynamic distance in solids
c_{ij}	Component of stiffness matrix
b	Magneto-elastic constant
\mathbf{m}	Magnetisation
g_r	Electronic gyromagnetic ratio
\mathbf{M}_s	Saturation Magnetisation
D	Exchange field
N_x, N_y, N_z	Demagnetisation factors
c_l, c_t	Longitudinal and transverse velocities
\mathbf{G}	Reciprocal lattice
\mathbf{v}	Velocity field in fluid

List of Abbreviations

Abbreviations	Original words
TR	Time-reversal
2D	Two-dimensional
PT	Parity-time
ER	Exceptional Ring
TKNN	Thouless-Kohmoto-Nightingale-den Nijs
MoS ₂	Molybdenum disulfide
GNR	Graphene nano-ribbon
KM	Kane-Mele
(H)BZ	(Half) Brillouin zone
1D	One-dimensional
TRP	Time-reversal polarisation
TRIM	Time-reversal invariant momenta
3D	Three-dimensional
FKM	Fu-Kane-Mele
(N)NN	(Next) Nearest-neighbour
SOC	Spin-orbit coupling
P	Parity
EP	Exceptional point
TE(TM)	Transverse electric(magnetic)
LT	Longitudinal-transverse
L	Longitudinal
T	Transverse
h.c.	Hermitian conjugate
(E)SHE	(Elastic) spin-Hall effect
YAG	Yttrium aluminium garnet
PC	Phononic crystal
ME	Magneto-elastic
FEM	Finite element method
MST	Multiple scattering theory
EMT	Effective medium theory
R.H.S.	Right hand side
L.H.S.	Left hand side
YIG	Yttrium iron garnet
QED	Quantum electrodynamics

Acknowledgement

Firstly, I would like to thank Professor Shuang Zhang for his kindness and tolerance to my aggressive personality, and also his prevision to the future scientific topic. His phenomenal instincts of physics always prevent me deviating from the path of research. In addition, I would like to express my gratitude to Dr. Wenlong Gao as an incredible group member. Both of us were mutually benefited from many inspirational discussions during the period we were in Birmingham. Throughout the years in Birmingham, the informal subgroup meeting at diverse coffee shops greatly helped me release the stress accumulated by the tough PhD life so I would like to thank all the members of this afternoon coffee break.

My special thanks give to my girlfriend, Ying-Chu who has been loving me for over twelve years since her freshman year at college. Her unconditional and selfless love supports me to walk through every difficulty in the foreign land. I absolutely will not forget my amazing parents. Mum, as a former professional chef, taught me lots of cooking skills which tremendously help me survive in the UK. Being not only a father but a wisdom mentor, dad always polishes my sharp angles, enlightens me via his experience, and makes me a better individual for society.

Lastly, I want to give my thanks to the Taiwanese Ministry of Education which provided three-year full scholarship for my PhD programme at University of Birmingham.

Chapter 1 Introduction

1-1: Background and Motivation

Over the past decades, the progress of topological nature in matter, such as quantum Hall effect and Z_2 topological insulators, has attracted substantial attention because it opens a window for the study of this unprecedented material phase [1-3]. Amongst all the fascinating phenomena, topological protection, a reflection-immune property against impurity or disorder in matters, is a main feature occurring in this type of materials. This special scattering-immunity states of electronic waves are probably the most impressive discovery in topological matters because it was observed in superconductors. For finding the fundamental concepts in topological nature, the theoretical study shows that time-reversal (TR) symmetry breaking plays an essential role to open a non-trivial energy gap, which is a fundamental condition bringing about the topologically protected edge states. The requirement of breaking TR symmetry can be realised by applying an external magnetic field or using the materials with strong intrinsic spin-orbit couplings.

On the other hand, the breakthrough of graphene preparation in 2004 has provided an elegant approach to realise this material. Graphene, which is a practical material with purely two-dimensional (2D) structure, possesses an interesting aspect that its low-energy approximation has the form as the same as massless Dirac equation [4]. This similarity gives rise to many of unusual properties for the electrons in graphene. One of them is that, despite governed by the same relativistic equation, the Dirac fermion in graphene with moving speed is much slower than the speed of light [4]. Additionally, the discovery of flat edge state in the band diagram of graphene initiates the study of its topological nature. Electrons with certain

energy will accumulate on the edges because of the zero group velocity of flat edge states [4]. If we further consider the intrinsic spin-orbit coupling inside the carbon atoms, topologically non-trivial gap can be lifted so that flat edge states can be converted into crossing ones. This is the fundamental idea of topological insulator first proposed by Kane and Mele in 2005 [5-6].

Recently, the rapid development of topological properties in condensed matter also arouse great interest in unveiling topological phenomena in other physical systems. In 2008, S. Raghu et. al [7-8] and Z. Wang et. al [9] simultaneously proposed the optical analogue of quantum Hall effect achieved theoretically by a gyromagnetic photonic crystal. Afterwards, Z. Wang and his colleagues at MIT research groups have realised topologically protected one-way edge states in experiments [10]. Also, for the photonic analogue of topological insulators, two approaches were proposed via employing photonic crystals composed of metamaterials [11] and coupled helical waveguides [12]. Nevertheless, only few researches focused on the analogues of classically vibrating systems, such as pressure acoustics [13] as well as mechanical oscillations [14-15]. Especially for elastic waves, it is challenging to achieve physics with topological nature due to its complexity caused by modes coupling. Owing to the rich of undiscovered topological physics in mechanical and elastic crystals, I decide to choose this subject as new physics and potential uses of elastic solids remains to be revealed.

In addition to the research of topological phenomena in classical regime, in this thesis two topics are included: spin-Hall effects and parity-time (PT) symmetric systems. Spin-Hall effects are phenomena of spin-orbit coupling leading to transverse spin currents caused by electrical currents and vice versa [16]. Despite its short history originating from the first experimental observation, spin-Hall effects are already prevailing in the field of spintronics as fundamental techniques of a spin-current receiver or generator. Apart from the triumph in electronic systems, recently physicists have realised a well-known phenomenon in optics

named Imbert-Fedorov shift, which is the photonic counterpart of spin-Hall effect [17]. Next, PT symmetric physics, which is firstly proposed by C. Bender [18] in 1998, generates real energy eigenvalues without the requirement of Hermitian Hamiltonian. This astonishing conclusion challenges a textbook hypothesis proposed by P. A. M. Dirac in which the operator of any observable must be Hermitian. Since then, the exploration of systems with PT symmetry becomes a significant topic in quantum mechanics [19], and it has extended to optical regime [20]. Consequently, inspired by this intriguing effect, in the following contents we will make the extension of studies to classical vibration, such as acoustic systems.

1-2: Overview of Thesis

In this thesis, the main body includes four chapters. Firstly, fundamental information in chapter two paves the way for the studies presented in the subsequent contents. Particularly, the condensed-matter theory described by the perspectives of topology, the crystals affected by spin-orbit coupling, as well as PT symmetric physics are outlined. Based on the previous discussion, mechanical crystals consisting of mass beads and springs are developed in chapter three with the discovery of topological chiral edge states and the elastic version of spin-Hall effect. Chapter four puts the focus of the subject on elastic solids with the theoretical prediction of a topologically non-trivial phase for pure shear waves and 2D elastic topological insulators. In chapter five, with the rotational Doppler effects in acoustics, non-dispersive materials will be transformed into dispersive ones in terms of the spinning velocity. Furthermore, a sonic crystal made of spinning cylinders can lead to pairs of exception rings (ERs) owing to the nature of an open system. The concluding chapter of the thesis provides a review of all proposed results and the outlook of potential subjects.

Chapter 2 Literature Reviews

2-1: Berry Phase

2-1.1: Brief Mathematical Review for Topology

Before the physics of this chapter, we briefly introduce an essential mathematical theorem called “Gauss-Bonnet theorem”, which combines the geometry and topology. The description of Gauss-Bonnet theorem is:

“If one takes the integral of Gaussian curvature over a closed surface, this integration divided by 2π defines a topological index called Euler characteristic/index which is equal to $2 - 2g$. [21]”

Here g means genus: the number of holes in an object. The equivalent mathematical expression of above description is given by

$$\chi = \frac{1}{2\pi} \int_s \mathcal{K} \cdot ds = 2 - 2g \quad (2-1)$$

where χ is Euler characteristic and \mathcal{K} is Gaussian curvature. Taking a sphere as an example, since there is no hole in it, the Euler index equals 2, matching the result of $\chi = (2\pi)^{-1} R^{-2} 4\pi R^2 = 2$. For a torus, according to Eq. (2-1), simply we know Euler characteristic is zero. In addition to Gauss-Bonnet Theorem, there is a relevant theorem called “hairy ball theorem” that can be considered as the visualising version of Gauss-Bonnet theorem. As shown in Fig. 2.1, if one considers that tangent vector fields continuously distribute on a closed surface. For a sphere, regardless of the arrangement, there exist two singularities that

correspond to the result of Euler characteristic; for a torus, the field distribution covers all the surface smoothly without having a singular point. In other words, hairy-ball theorem directly connects the number of singularities in a closed surface with Euler characteristic in topology. In the next section, a concept in physics referred as Berry phase is discussed. Due to the same mathematical expressions, Berry mechanism shows a one-to-one correspondence to Euler characteristic, which links physics with topology.

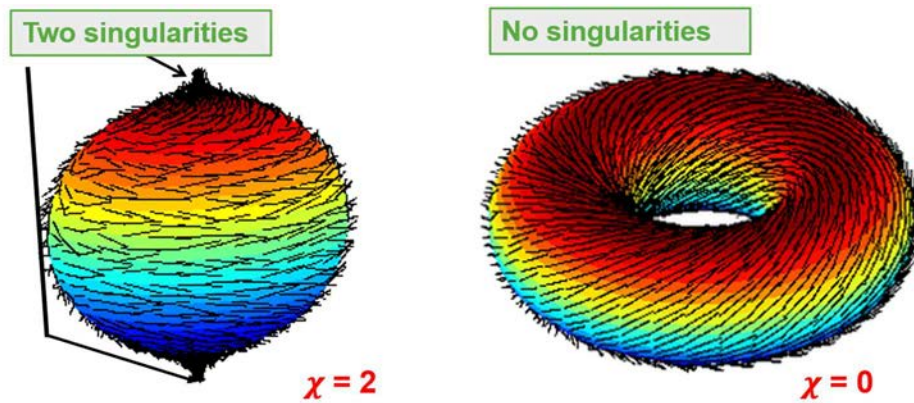


Fig. 2.1: Hairy-ball theorem. Tangent vector fields distributed on distinct closed surfaces. (a) Two singularities are clearly shown on the top and bottom of the sphere. The number of singularities is exactly equal to Euler characteristics (b) There exist no singular points on a torus, matching the result given by Gauss-Bonnet theorem. [22]

2-1.2: Basic Concepts of Berry Phase

We begin by Schrödinger equation which can be written as

$$i\hbar\partial_t|\psi\rangle = \hat{H}|\psi\rangle \quad (2-2)$$

and its general time-dependent solution is

$$|\psi\rangle = \exp[i\gamma_n(t)] \exp\left[\frac{-i}{\hbar} \int_0^t dt' \varepsilon_n(t')\right] |n\rangle \quad (2-3)$$

ε_n is the eigenvalue of Hamiltonian, namely, $\hat{H}|n\rangle = \varepsilon_n|n\rangle$. The second exponential term is a time-evolution solution and the first one is usually neglected because the initial phase can be

set as zero. However, in 1984, M. Berry pointed out that this phase is crucial if a closed path is taken adiabatically in parametric space [23]. Here we emphasise the meaning of ‘adiabatically’, that is, the parameter changes gradually in the system. Thus, energy transition of distinct states will not occur in the course of varying operation. Its literal use is not identical to the one in thermodynamics in which denotes there is no energy exchange during the process. In a closed loop, this phase term $\gamma_n(t)$ can be presented as [23]

$$\gamma_n(t) = \oint_c \mathcal{A}(\mathcal{R}) \cdot d\mathcal{R} = \int_s \Omega(\mathcal{R}) \cdot ds, \quad (2-4)$$

where

$$\mathcal{A}_n(\mathcal{R}) = i \langle n(\mathcal{R}) | \nabla_{\mathcal{R}} | n(\mathcal{R}) \rangle, \quad (2-5)$$

$$\Omega_n(\mathcal{R}) = i \langle \nabla_{\mathcal{R}} n(\mathcal{R}) | \times | \nabla_{\mathcal{R}} n(\mathcal{R}) \rangle. \quad (2-6)$$

Here $\gamma_n(t)$ is usually called Berry flux, Berry phase or geometric phase, whilst $\Omega_n(\mathcal{R})$ is Berry curvature or Berry field and $\mathcal{A}_n(\mathcal{R})$ is Berry connection. Note that, as Eq. (2-4) has the same formalism as Eq. (2-1), one can intuitively expect that Berry phase divided by 2π could also result in an index. This index is referred as Chern number, which is the interpretation of quantum Hall effect. We will see it in the upcoming content. Additionally, because of the formal similarity between the expression of Berry phase and magnetic flux in electromagnetism, it is evident that Berry curvature $\Omega_n(\mathcal{R})$ is a gauge invariant but $\mathcal{A}_n(\mathcal{R})$ is a gauge dependent. To verify, as scalar quantity $\zeta(\mathcal{R})$ can be introduced subsequently which satisfies the relation of gauge transformation $\mathcal{A}_n(\mathcal{R}) \rightarrow \mathcal{A}_n(\mathcal{R}) + \nabla_{\mathcal{R}} \zeta(\mathcal{R})$ such that the geometrical phase γ_n accumulated along the path is eliminated and the wave function in Eq. (2-3) will not be changed.

This helps to simplify the problem by choosing a proper $\zeta(\mathcal{R})$ in different systems.

Furthermore, one can define a gauge field tensor evaluated from the Berry connection as: [23]

$$\Omega_{\mu\nu}^n(\mathcal{R}) = \frac{\partial \mathcal{A}_\nu^n(\mathcal{R})}{\partial \mathcal{R}^\mu} - \frac{\partial \mathcal{A}_\mu^n(\mathcal{R})}{\partial \mathcal{R}^\nu} = i \left[\left\langle \frac{\partial n(\mathcal{R})}{\partial \mathcal{R}^\mu} \middle| \frac{\partial n(\mathcal{R})}{\partial \mathcal{R}^\nu} \right\rangle - \left\langle \frac{\partial n(\mathcal{R})}{\partial \mathcal{R}^\nu} \middle| \frac{\partial n(\mathcal{R})}{\partial \mathcal{R}^\mu} \right\rangle \right] \quad (2-7)$$

Comparing the tensor form $\Omega_{\mu\nu}^n$ and vector form $\mathbf{\Omega}_n$ of Berry curvature, they are related to each other by $\Omega_{\mu\nu}^n = \varepsilon_{\mu\nu\xi} (\mathbf{\Omega}_n)_\xi$, where $\varepsilon_{\mu\nu\xi}$ is Levi-Civita symbol. In addition to the tensor and vector forms, Berry curvature can also be rewritten as a summation of eigenstates by means of the identity $\langle n | \partial_i H | m \rangle = \langle \partial_i n | m \rangle (\varepsilon_n - \varepsilon_m)$: [23]

$$\Omega_{\mu\nu}^n(\mathcal{R}) = i \sum_{m \neq n} \frac{\langle n | \partial_\mu H | m \rangle \langle m | \partial_\nu H | n \rangle - \langle n | \partial_\nu H | m \rangle \langle m | \partial_\mu H | n \rangle}{(\varepsilon_n - \varepsilon_m)^2} \quad (2-8)$$

where $\partial_i = \partial / \partial \mathcal{R}^i$ and $i = u, v$. Eq. (2-8) has a significant advantage in the use of numerical simulation because it is independent from the gauge choice of wave functions. If there are three components in the parameter space, Berry curvature can be viewed as the magnetic field in electromagnetism, e.g. $\Omega_{12}^n(\mathcal{R}) \equiv \Omega_z^n(\mathcal{R}) = \partial_1 \mathcal{A}_2^n(\mathcal{R}) - \partial_2 \mathcal{A}_1^n(\mathcal{R})$. To clarify the mathematical form of Berry mechanism, a comparison of formalism between Berry mechanism and the magnetic field is shown in the following table:

	Berry mechanism	Magnetic field
Connection/Vector potential	$\mathcal{A}_n(\mathcal{R}) = i \langle n(\mathcal{R}) \nabla_{\mathcal{R}} n(\mathcal{R}) \rangle$	\mathbf{A}
Curvature/Magnetic Field	$\mathbf{\Omega}_n(\mathcal{R}) = i \langle \nabla_{\mathcal{R}} n(\mathcal{R}) \times \nabla_{\mathcal{R}} n(\mathcal{R}) \rangle$	$\mathbf{B} = \nabla \times \mathbf{A}$
Phase/Magnetic flux	$\gamma_n(t) = \int_s \mathbf{\Omega}_n(\mathcal{R}) \cdot d\mathbf{s}$	$\Phi_B(t) = \int_s \mathbf{B} \cdot d\mathbf{s}$

Gauge transformation	$\mathcal{A}_n(\mathcal{R}) \rightarrow \mathcal{A}_n(\mathcal{R}) + \nabla_{\mathcal{R}} \zeta(\mathcal{R})$	$\mathbf{A} \rightarrow \mathbf{A} + \nabla \phi$
Gauge invariant quantity	$\Omega_n(\mathcal{R})$	\mathbf{B}
Dirac Monopole*	$\Omega_{\pm}(\mathcal{R}) = \mp \frac{\mathcal{R}}{2\mathcal{R}^2(t)}$	$\mathbf{B} = \frac{\mathbf{r}}{2r^2}$

Table I: Comparison between Magnetic Fields and Berry Mechanism. This table compares vector potentials, magnetic fields, and magnetic flux with Berry mechanism. Considering Berry connection as the vector potential, Berry curvature and phase have one-to-one correspondence to magnetic field and magnetic flux. In addition, due to the same formalism, Berry curvature is a gauge independent quantity like magnetic field. They also share the same field distribution while a monopole is considered.

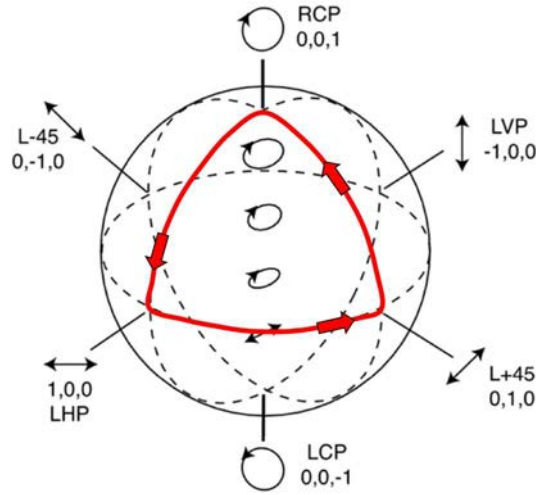


Fig. 2.2: Poincaré Sphere. A polarisation sphere depicts two circular polarisations on north and south pole, and linear polarisations around the equator. Circling a closed red curve on Poincaré sphere, the area of the geodesic triangle defines a solid angle and its magnitude divided by 2 can deduce the geometric phase. [24]

Berry phase is a universal phenomenon that has different physical meanings in distinct systems. Apart from the interpretation in solid-state physics, which will be discussed in next section, it is worth noting that there is another effect caused by Berry phase in polarised optics. If one considers a cycle change of light polarisations, this process is accompanied by a phase

*Dirac monopole, sometimes called “magnetic monopole”, is a hypothetical particle proposed by P. A. M. Dirac for creating the duality of Maxwell equations. According his definition, Dirac monopole has a single, isolated magnet, which can exist only with either north pole or south pole.

shift determined by the geometry of the cycle as indicated on the Poincaré sphere shown in Fig. 2.2. The main result considers a light beam that returns to its initial polarised state via two intermediate polarisations. In 1956, S. Pancharatnam proved that, in such circumstance, the phase is not equal to its original value rather than an increase by $-\theta_{\text{solid}}/2$, where θ_{solid} denotes the solid angle given by geodesic triangle whose vertices are three polarised states on Poincaré sphere [24]. This additional phase was later confirmed by M. Berry himself as the first proposal of geometric phase right after he published his remarkable work in 1984 [23]. Simply put, in polarised optics, the physical meaning of Berry phase is the extra phase term of a loop of polarised state change. Nowadays, the geometric phase in optical regime is also called Pancharatnam-Berry phase to honour Pancharatnam's prevision decades ago.

2-1.3: Berry Phase and Chern Number in Crystalline Solids

After an overview of Berry phase, a periodic potential system, which is widely used for analysing crystalline solids, will be discussed in this section. With an external field, we consider a single electron propagating in periodic potential circumstance and affected by an external vector potential $\mathbf{A}(t)$. Its Hamiltonian therefore yields

$$\hat{H} = \frac{(\hat{\mathbf{p}} - e\mathbf{A})^2}{2m} + V(\mathbf{r}) \quad (2-9)$$

where $V(\mathbf{r} + \mathbf{a}) = V(\mathbf{r})$ is the periodic condition with lattice constant a . The states of this category of Hamiltonian (2-9) satisfy the boundary condition $\psi_n(\mathbf{r} + \mathbf{a}) = \exp(i\mathbf{q} \cdot \mathbf{a})\psi_n(\mathbf{r})$ in accordance with Bloch theorem. If the eigenstates are transferred into Bloch function $u(\mathbf{r})$ using $u_n(\mathbf{r}) = \exp(-i\mathbf{q} \cdot \mathbf{r})\psi_n(\mathbf{r})$, the Hamiltonian reads

$$\hat{H}|u_n\rangle = \left[\frac{(\hat{\mathbf{p}} + \hbar\mathbf{q})^2}{2m} + V(\mathbf{r}) \right] |u_n\rangle = \varepsilon_n(\mathbf{q})|u_n\rangle, \quad (2-10)$$

where $\mathbf{q} = \mathbf{k} - (e/\hbar)\mathbf{A}$ and the Bloch states $u_n(\mathbf{r})$ satisfy the periodic boundary condition

$$u_n(\mathbf{r} + \mathbf{a}) = u_n(\mathbf{r}). \quad (2-11)$$

The boundary condition given by Eq. (2-11) make sure all eigenstates are in the same Hilbert space. One can regard the momentum within the Brillouin zone as parametric space, while u_n is the eigenfunction of the Hamiltonian. Consequently, if a one-dimensional (1D) system is considered as Bloch waves in momentum (\mathbf{q}) space, according to Eq. (2-4), Berry phase is

$$\gamma_n = \int_{-\pi/a}^{\pi/a} i \langle u_n(\mathbf{q}) | \nabla_{\mathbf{q}} | u_n(\mathbf{q}) \rangle \cdot d\mathbf{q}, \quad (2-12)$$

where γ_n in crystalline solid is referred to the Zak phase [22]. For higher dimensional cases, Eq. (2-12) can be generalised as

$$\gamma_n = \int_{BZ} i \langle u_n(\mathbf{q}) | \nabla_{\mathbf{q}} | u_n(\mathbf{q}) \rangle \cdot d\mathbf{q}, \quad (2-13)$$

in which the subscript ‘‘BZ’’ represents the first Brillouin zone.

In Zak’s paper [25], there are three unique features of a single electron moving in crystalline solid. Firstly, in Berry’s original work, the parametric space must be applied from additional physical quantities, e.g. magnetic fields. Yet, the parametric space is indeed the momentum space which is provided by the periodic potential system itself. In other words, any parameter/field implemented externally is dispensable. Secondly, since Brillouin zone can be taken as a torus, taking Berry curvature integration over the entire Brillouin zone naturally happens in a closed surface. Hence, even in a 1D parametric space, a non-zero Berry phase can

be obtained. Finally, Bloch states are equipped with symmetry properties in the Brillouin zone and, as a consequence of the symmetry, Berry phase divided by 2π becomes quantised numbers that imply a one-to-one correspondence to the topology.

In condensed-matter theory, Berry phase plays a significant role in many phenomena. Amongst all the applications of Berry phase, there is a crucial one that can explain the quantised particle transport and anomalous velocity in solids [26]. Hamiltonian (2-9) satisfies $\hat{H}(t) = \hat{H}(t+T)$ in a system under a slowly varying time evolution, such as the low-frequency alternating voltage source. Under this slowly varying condition, the time-dependant Hamiltonian still retains the translational symmetry of the solids. Thus, the instantaneous states retain Bloch wave expression $e^{i\mathbf{q}\cdot\mathbf{r}} |u_n(\mathbf{q}, t)\rangle$ and the Hamiltonian becomes $\hat{H}(\mathbf{q}, t)$. From this description, the wavevector and time are two independent coordinates of a parametric space, i.e. $\mathbf{R} = (\mathbf{q}, t)$. Therefore, the 1D adiabatic transverse current induced by varying external field is given by [26]

$$j_H = -\frac{1}{2\pi} \sum_n \int_{BZ} \Omega_{qt}^n dq, \quad (2-14)$$

where n means the band index beneath Fermi energy. Eq. (2-14) shows that an induced transverse current comes from Berry curvature rather than the gradient of the energy. It is worth noting that, before geometric phase was proposed, Eq. (2-14) had been independently obtained by D. Thouless et. al. [24]. In their ground-breaking article, the conductance in quantum Hall effect can be linked to a universal constant multiplied by the topological integer [27]

$$G_H = -\frac{e^2}{h} \sum_n \frac{1}{2\pi i} \int_{BZ} d^2k \langle \nabla_{\mathbf{k}} n | \times | \nabla_{\mathbf{k}} n \rangle = \sum_n \frac{e^2}{h} C_n \quad (2-15)$$

where e is electron charge, h is Planck constant, and C is called TKNN number. Soon after that, the connection between Berry phase and TKNN number was built. Additionally, as TKNN number $C_n = (2\pi)^{-1} \int_{BZ} d^2k \langle \nabla_{\mathbf{k}} n | \times | \nabla_{\mathbf{k}} n \rangle$ is mathematically identical to the expression of Chern number/invariant in topology, another beautiful connection between math and physics is discovered. To this day, in condensed-matter theory Berry phase and TKNN nu are unified under the same framework of Chern number description which is an integer to categorise the topology of geometry in mathematics. As a result, all the matters with non-zero Chern numbers are referred as topological materials.

Next, for anomalous velocity, since the translational symmetry is not broken by the vector potential \mathbf{A} , \mathbf{q} remains a good quantum number and its time differentiation gives rise to a constant of motion, i.e. $\dot{\mathbf{q}} = 0$ ($i\hbar\dot{\mathbf{q}} = [\hat{H}, \hat{\mathbf{q}}] \rightarrow \dot{\mathbf{q}} = 0$). Therefore, the equation of motion reads $\dot{\mathbf{k}} = (e/\hbar)\mathbf{E}$. Thus, using the relation $\partial/\partial\mathbf{q} = \partial/\partial\mathbf{k}$ and $\partial/\partial t = -(e/\hbar)\mathbf{E} \cdot \partial/\partial\mathbf{k}$, one finds [26]

$$v_n(\mathbf{k}) = \frac{\partial \varepsilon_n(\mathbf{k})}{\hbar \partial \mathbf{k}} - \frac{e}{\hbar} \mathbf{E} \times \boldsymbol{\Omega}_n(\mathbf{k}), \quad (2-16)$$

where \mathbf{E} denotes applied fields and

$$\boldsymbol{\Omega}_n(\mathbf{k}) = i \langle \nabla_{\mathbf{k}} u(\mathbf{k}) | \times | \nabla_{\mathbf{k}} u(\mathbf{k}) \rangle. \quad (2-17)$$

As denoted in Eq. (2-16) and (2-17), besides the normal band contribution, an additional term also contributes the velocity to $v_n(\mathbf{k})$. This velocity induced by the second term of Eq. (2-16), which is called anomalous velocity, is transverse to direction of applied electric fields and leads to the Hall current. All in all, the pivotal physical meaning of transverse Hall currents is the contribution of Berry curvature.

Lastly, we present a brief discussion: how universal spatial inversion/parity (P) and TR symmetries influence Berry curvature/phase [26]. According to Eq. (2-16), this velocity formula must be unchanged under TR and P symmetry if there are no external fields in the system. Due to the TR symmetry, v_n and \mathbf{k} flip sign but the electric field \mathbf{E} remain the same because it is a polar(true) vector; under P symmetry, v_n , \mathbf{k} and \mathbf{E} all change sign. Hence, under the TR-symmetry, Berry curvature given by Eq. (2-17) requires $\mathbf{\Omega}_n(-\mathbf{k}) = -\mathbf{\Omega}_n(\mathbf{k})$; for spatial inversion symmetry, Berry curvature should be an even function, i.e. $\mathbf{\Omega}_n(-\mathbf{k}) = \mathbf{\Omega}_n(\mathbf{k})$. As a crystal with both symmetries, Berry curvature vanishes over the whole Brillouin zone. However, there are many essential physical systems breaking either TR symmetry or P symmetry, e.g. ferromagnetic materials. For these systems, it is necessary to adopt Berry mechanism to explicitly interpret its physical phenomena.

2-1.4: Bulk-Edge Correspondence

In the previous section, we have stated the role of Berry phase in condensed-matter physics. In all above discussions, Eq. (2-15) demonstrates an intimate relationship between Hall conductance and Chern(TKNN) number (Berry phase divided by 2π). Here, we focus on the meaning of Chern number and introduce a crucial theorem referred as *bulk-edge correspondence* that connects Chern numbers calculated from bands with the number of edge states. The description of bulk-edge correspondence is:

“There exist gapless edge states within the bandgap, if and only if a bulk topological index of a gapped system is non-trivial(non-zero). The number of gapless edge states is equivalent to the difference between upper and lower Chern number summation, where upper(lower) bands are defined as the bands higher(lower) than the chosen gap.” [28]

Bulk-edge correspondence gives two essential concepts. Firstly, this theorem explains that, even though the material is a bulk insulator, edge states arise while the boundaries are made, namely, insulator inside but conductor along the boundaries. It can be regarded as a bridge linking Chern number and the emergence of gapless edge states. Consequently, to ensure whether the material is topologically nontrivial or not, firstly, one must find Chern number of the bulk band structure. Secondly, it also states the method of calculating the number of edge states. As depicted in Fig. 2.3, if the summations of upper and lower bands are given, the difference between them determines an integer indicating the number of edge states. With bulk-edge correspondence, we are in a position to study topological properties and the edge states in the following content.

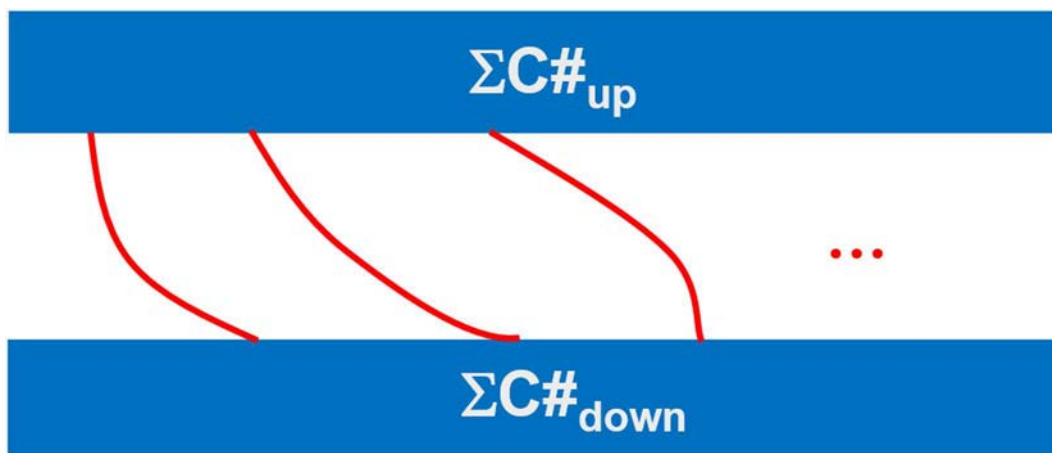


Fig. 2.3: Bulk-edge Correspondence. A schematic plot for bulk-edge correspondence. The blue shaded areas stand for bulk region. By adding up all the Chern numbers higher and lower than the chosen bandgap, their difference defines topological feature of the gap and the number of gapless edge states.

2-2: Graphene and Topological Insulator

2-2.1: Tight-Binding Description of Graphene

A. Geim and K. S. Novoselov proposed a straightforward but efficient approach for the fabrication of graphene in 2004 [29]. Ever since, the study of graphene, especially for its electronic properties, has attracted considerable interest to this practical 2D material. Due to

the C_3 symmetric geometry, a semi-metal graphene exhibits point degeneracies at K points around the first Brillouin zone. In the vicinity of these degeneracies, the behaviour of electrons governed by the formula is as the same as massless Dirac equation [4]. These special point degeneracies, therefore, are referred as Dirac points. Additionally, for graphene terminated with zigzag or bearded edges illustrated in Fig. 2.4a, one can find flat edge states connected to every K point. It makes charge accumulation on the boundary because of zero group velocity. In the following paragraph, we will introduce detailed information regarding aforementioned properties.

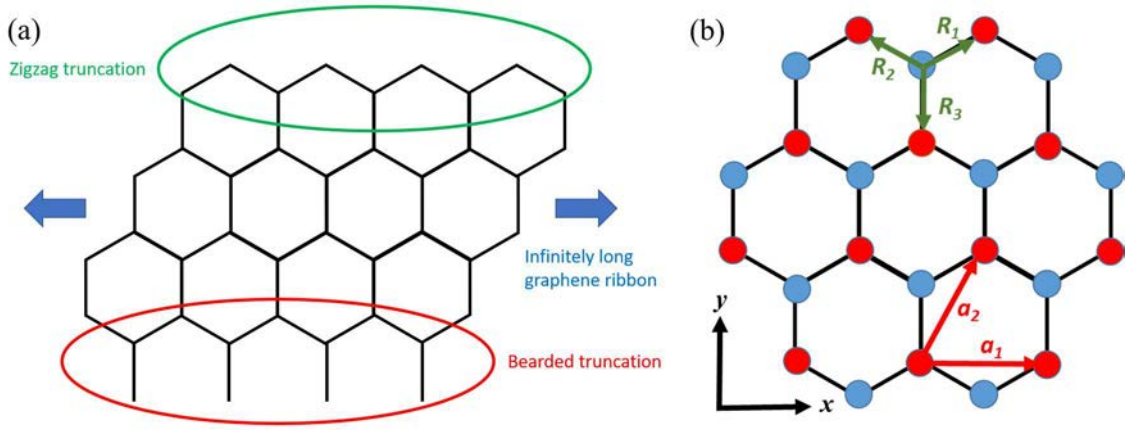


Fig. 2.4: The geometry of graphene. (a) The illustration of two distinct truncations of a graphene nano-ribbon (b) R indicates the bonds to three nearest atoms and a shows lattice vectors. Red and cyan dots represent A and B sublattice atoms, respectively.

Let us begin by tight-binding Hamiltonian of graphene. As shown in Fig. 2.4b, the nearest neighbours vectors give $\mathbf{R}_1 = (\sqrt{3}\hat{x} + \hat{y})a/2$, $\mathbf{R}_2 = -(\sqrt{3}\hat{x} - \hat{y})a/2$, $\mathbf{R}_3 = -a\hat{y}$ and lattice constant vectors are $\mathbf{a}_1 = \sqrt{3}a\hat{x}$ and $\mathbf{a}_2 = (\sqrt{3}\hat{x} + 3\hat{y})a/2$. Considering the nearest-neighbour hopping, the tight-binding Hamiltonian can be written as [4]

$$H = -t \sum_{\langle i,j \rangle} (c_i^\dagger c_j + h.c.), \quad (2-18)$$

where t is the hopping parameter, c_i^\dagger (c_i) is creation (annihilation) operator at position i , and $\langle \rangle$ means electrons interact only with their nearest neighbours. Applying Wannier functions $c_i^+ = N^{-1/2} \sum_k c_k^+ \exp(-i\mathbf{k} \cdot \mathbf{R})$ and substituting it into Eq. (2-18), we obtain

$$H = -t \sum_k \left[a_k^\dagger b_k \left(e^{-i\mathbf{k} \cdot \mathbf{R}_1} + e^{-i\mathbf{k} \cdot \mathbf{R}_2} + e^{-i\mathbf{k} \cdot \mathbf{R}_3} \right) + h.c. \right], \quad (2-19)$$

which can be further simplified through introducing pseudo-spin degree of freedom, so we rewrite it as

$$H = -\frac{t}{2} \sum_{k\alpha\beta} \left[\sigma_{\alpha\beta}^+ a_{k\alpha}^\dagger b_{k\beta} \left(e^{-i\mathbf{k} \cdot \mathbf{R}_1} + e^{-i\mathbf{k} \cdot \mathbf{R}_2} + e^{-i\mathbf{k} \cdot \mathbf{R}_3} \right) + h.c. \right], \quad (2-20)$$

where $\sigma^\pm = \sigma^x \pm i\sigma^y$, σ^i are Pauli matrices. For simplicity, one can define a vector \mathbf{d} such that $d^\pm(\mathbf{k}) = -tf(\mathbf{k})$, $f(\mathbf{k}) = \left(e^{\mp i\mathbf{k} \cdot \mathbf{R}_1} + e^{\mp i\mathbf{k} \cdot \mathbf{R}_2} + e^{\mp i\mathbf{k} \cdot \mathbf{R}_3} \right)$, where

$$d_x(\mathbf{k}) = \left[d^+(\mathbf{k}) + d^-(\mathbf{k}) \right] / 2 = -t \left(\cos \mathbf{k} \cdot \mathbf{R}_1 + \cos \mathbf{k} \cdot \mathbf{R}_2 + \cos \mathbf{k} \cdot \mathbf{R}_3 \right), \quad (2-21)$$

$$d_y(\mathbf{k}) = \left[d^+(\mathbf{k}) - d^-(\mathbf{k}) \right] / 2i = -t \left(\sin \mathbf{k} \cdot \mathbf{R}_1 + \sin \mathbf{k} \cdot \mathbf{R}_2 + \sin \mathbf{k} \cdot \mathbf{R}_3 \right), \quad (2-22)$$

and Hamiltonian becomes $H = \sum_{k\alpha\beta} \mathbf{d} \cdot \boldsymbol{\sigma}_{\alpha\beta} a_{k\alpha}^\dagger b_{k\beta}$. Let $H = \sum_{k\alpha\beta} H_{\alpha\beta}(\mathbf{k}) a_{k\alpha}^\dagger b_{k\beta}$ with

$H(\mathbf{k}) = \mathbf{d}(\mathbf{k}) \cdot \boldsymbol{\sigma}$. If we operate Hamiltonian twice, the energy spectrum in terms of \mathbf{k} is given by [4]

$$\varepsilon_\pm(\mathbf{k}) = \pm \sqrt{d_x^2 + d_y^2} = \pm t \sqrt{3 + 2 \cos(\sqrt{3}k_x a) + 4 \cos\left(\frac{\sqrt{3}}{2}k_x a\right) \cos\left(\frac{3}{2}k_y a\right)}, \quad (2-23)$$

Note that Eq. (2-23) vanishes at K/K' points $(k_x, k_y) = (\pm 4\pi/3a, 0)$ or other points after 60-degree rotation around Γ point as shown in Fig. 2.5, so that the degeneracies of bands are confirmed. Furthermore, we consider a small amount quantity of k space near K points. By taking cosine in a second-order expansion, Eq. (2-23) becomes

$$\varepsilon_{\pm}(\mathbf{k}) = \pm \frac{3}{2} ta \sqrt{\delta k_x^2 + \delta k_y^2} = \pm v |\delta \mathbf{k}|. \quad (2-24)$$

Eq. (2-24) indicates an energy spectrum of massless Dirac fermion. Comparing Eq. (2-24) with (2-23), \mathbf{d} vectors near Dirac points are expressed as

$$d_x^{\pm} = \pm \frac{3ta}{2} \delta k_x, \quad d_y^{\pm} = \frac{3ta}{2} \delta k_y, \quad (2-25)$$

where \pm stands for the two valleys points K and K'. Moreover, the Hamiltonian at K and K' point are respectively defined as

$$H_{\pm}(\mathbf{k}) = v(\pm \delta k_x \sigma_x + \delta k_y \sigma_y). \quad (2-26)$$

For a more general description, we add the z component of Pauli matrix into Eq. (2-26) as [4]

$$H_{\pm}(\mathbf{k}) = v(\pm k_x \sigma_x + k_y \sigma_y) + m_{eff} \sigma_z. \quad (2-27)$$

The term $m_{eff} \sigma_z$ appears provided that the inversion symmetry of the 2D material is broken, e.g. MoS₂. This effective mass term lifts a spin-independent gap, then the graphene becomes a trivial insulator as Fermi level locates in the gap. In short, different sub-lattices break the inversion symmetry which gives rise to a topologically trivial material.

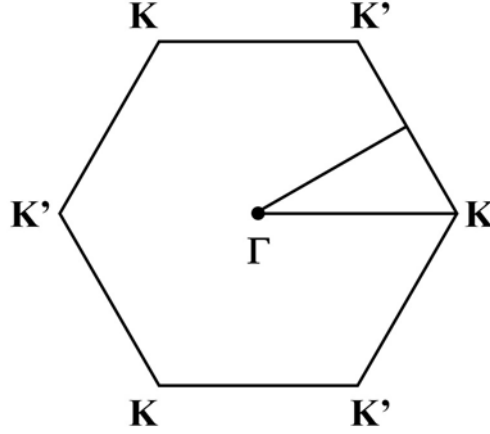


Fig. 2.5: First Brillouin zone of graphene. Γ is the centre of Brillouin zone. K and K' label two kinds of high symmetry points (valleys) around Brillouin vertices.

2-2.2: Flat Edge States in Graphene Nano-Ribbon (GNR)

In the previous section, an infinite 2D graphene is discussed based on the content in [4]. Since the lattice is invariant under lattice translations ($x \rightarrow x+a$, $y \rightarrow y+a$), the reciprocal lattice vectors are good quantum numbers, which give $[k_x, H] = [k_y, H] = 0$. Besides, k_x and k_y commute with each other so that energy eigenvalue can be expressed as $\varepsilon_n(k_x, k_y)$. However, to have an “edge state”, at least a boundary must exist. Hence, for a graphene nano-ribbon (GNR) with a finite width along y direction but infinite length along x direction, the lattice shift in real space can be transform into k_x but k_y cannot. Thus, energy eigenvalue can no longer be represented as $\varepsilon_n(k_x, k_y)$, yet the energy in terms of k_x can still be defined. In this section, numerical calculations are used for finding edge states in the distinct types of GNRs.

Firstly, a zigzag lattice arrangement is shown in Fig. 2.6, one can follow Eq. (2-18) and get tight-binding Hamiltonian [4]

$$H = -t \sum_{m,n} \left[c_A^\dagger(m,n) \{ c_B(m,n) + c_B(m,n-1) + c_B(m-1,n) \} + h.c. \right]. \quad (2-28)$$

Employing Fourier decomposition for Eq. (2-28) results in

$$H = -t \int \frac{dk}{2\pi} \sum_n \left[c_A^\dagger(k, n) \{ c_B(k, n) + c_B(k, n-1) + e^{ika} c_B(k, n) \} + h.c. \right]. \quad (2-29)$$

Using one-particle approximation $|0\rangle\langle 0| = 1$, and insert it into Eq. (2-29) we have

$$H = -t \int \frac{dk}{2\pi} \sum_n \left[\{ (1 + e^{ika}) |a, k, n\rangle\langle b, k, n| + |a, k, n\rangle\langle b, k, n-1| \} \right. \\ \left. + \{ (1 + e^{-ika}) |b, k, n\rangle\langle a, k, n| + |b, k, n-1\rangle\langle a, k, n| \} \right], \quad (2-30)$$

where $|a, k, n\rangle = c_A^\dagger(k, n)|0\rangle$. We assume the wave function is a linear superposition of a and b

state such that $|\Psi(k)\rangle = \sum_n \alpha(k, n)|a, k, n\rangle + \beta(k, n)|b, k, n\rangle$. Since Schrödinger equation in

momentum space is written as $H|\Psi(k)\rangle = \varepsilon(k)|\Psi(k)\rangle$, one can apply the identity

$\langle a, k, n|b, k, n\rangle = 0$, and then obtain

$$H(k)|\Psi(k)\rangle = \sum_n \left[\{ (1 + e^{ika}) \beta(k, n)|a, k, n\rangle + \beta(k, n-1)|a, k, n\rangle \} \right. \\ \left. + \{ (1 + e^{-ika}) \alpha(k, n)|b, k, n\rangle + \alpha(k, n)|b, k, n-1\rangle \} \right]. \quad (2-31)$$

Comparing with $\varepsilon(k)|\Psi(k)\rangle$, we have equations for site A and B

$$-t \left[2e^{ika/2} \cos(ka/2) \beta(k, n) + \beta(k, n-1) \right] = \varepsilon(k) \alpha(k, n), \quad (2-32)$$

$$-t \left[2e^{-ika/2} \cos(ka/2) \alpha(k, n) + \alpha(k, n+1) \right] = \varepsilon(k) \beta(k, n). \quad (2-33)$$

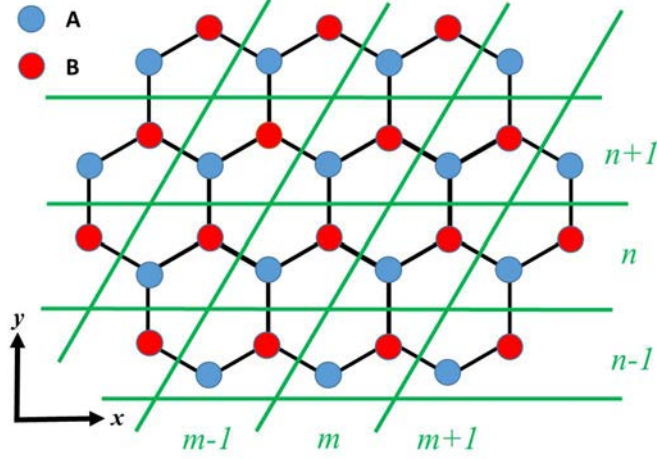


Fig. 2.6: Labelling approach for zigzag graphene nanoribbon. Along x direction the length of ribbon goes to infinite as well as a finite width in the transverse direction.

Note that two equations derived from its Hermitian conjugate are neglected because it is unnecessary to utilise these formulae for the following discussion. Expanding Eq. (2-32) and (2-33) as the matrix form, it can be expressed as

$$\begin{bmatrix} 0 & -2ts & 0 & \cdots \\ -2ts & 0 & -t & 0 \\ 0 & -t & 0 & -2ts \\ \vdots & 0 & -2ts & \ddots \end{bmatrix}_{2N \times 2N} \begin{bmatrix} \alpha_1 \\ \beta_1 \\ \alpha_2 \\ \vdots \end{bmatrix}_{2N} = \begin{bmatrix} \varepsilon & 0 & 0 & \cdots \\ 0 & \varepsilon & 0 & 0 \\ 0 & 0 & \varepsilon & 0 \\ \vdots & 0 & 0 & \ddots \end{bmatrix} \begin{bmatrix} \alpha_1 \\ \beta_1 \\ \alpha_2 \\ \vdots \end{bmatrix}_{2N}, \quad (2-34)$$

where $s = \cos(ka/2)$ and the phase term is neglected since they will not affect the energy band structure. By solving Eq. (2-34), Fig. 2.7a shows the 1D projected band structure, where the projected band structure depicts a sideview from its 2D bulk band structure, i.e. $H(k_x, k_y) \rightarrow H(k_x)$. Evidently, there is a flat band at zero energy between two Dirac points. Furthermore, to verify whether it is an edge state or just a trivial bulk band, Fig. 2.7b illustrates probability density along y direction. Two peaks are observed on both ends; hence the existence of edge states is proved.

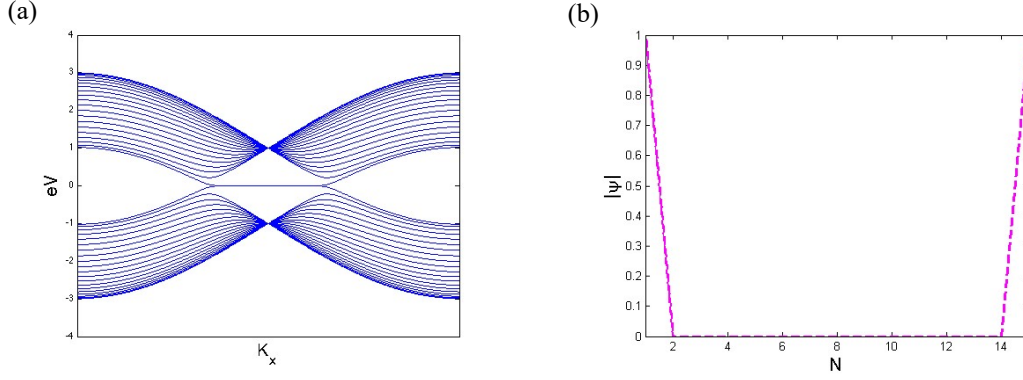


Fig. 2.7: Edge states of graphene. (a) Band diagram of graphene nanoribbon with zigzag termination for $t = a = 1$. (b) Flat edge state is shown in the centre of tight-binding band structure.

2-2.3: Rashba and Dresselhaus Spin-Orbit Coupling

Spin-orbit interaction is one of the major features in quantum mechanics. Due to the relativistic effect, even in absence of an external magnetic field, the electrons moving in the electric field generated from nucleus experience a magnetic field in their reference frame. This field interacting with the spin magnets of electrons results in the coupling between spins and orbital fields, namely, spin-orbit coupling. In quantum mechanics, as a charged particle with momentum \mathbf{p} moving in a magnetic field \mathbf{B} gives rise to Zeeman effect $\mu_B \boldsymbol{\sigma} \cdot \mathbf{B}$. Based on the relation $c\mathbf{B} = -\mathbf{E} \times \mathbf{v}$, the Hamiltonian caused from SOC is given by $H_{SOC} \sim (\mu_B/mc^2) \boldsymbol{\sigma} \cdot (\mathbf{E} \times \mathbf{p})$, which is the origin of fine structure in early quantum mechanical history.

In the above discussion, SOC exists in any atoms and its properties are independent of the spatial symmetry. However, in crystals, besides nuclei's electric field, there is an additional source originated by the gradient of the crystalline potential $\mathbf{E} = -\nabla V$ which generates a SOC term $H_{SOC} \sim -(\mu_B/mc^2) \boldsymbol{\sigma} \cdot (\nabla V \times \mathbf{p})$. Since such SOC Hamiltonian preserves under TR operation, the momentum operator \mathbf{p} must be odd that implies a possibility of linear momentum term in this type of SOC [30]. In 1955, G. Dresselhaus [31] firstly pointed out that, the material

without spatial inversion symmetry such as zinc-blende III–V semiconductor GaAs, its SOC term near Γ point exhibits an expression distinguished from the SOC in atoms. Especially, by applying the external strain along the [001] direction, the SOC Hamiltonian is written as

$$H_D = \lambda_D (\sigma_x p_x - \sigma_y p_y), \quad (2-35)$$

where λ_D denotes Dresselhaus SOC coefficient. In addition to central inversion symmetry breaking, in certain cases inversion symmetry can also be broken. For example, the quantum well breaks spatial inversion symmetry in the growth direction. Y. A. Bychkov and E. I. Rashba [32] proposed that such potential discontinuity at interface generates electric field \mathbf{E}_z , causing a SOC closed to Γ point written by

$$H_R = \alpha_R \boldsymbol{\sigma} \cdot (\mathbf{z} \times \mathbf{p}) = \alpha (\sigma_x p_y - \sigma_y p_x), \quad (2-36)$$

where λ_R denotes the Rashba SOC coefficient. In graphene, as it preserves central inversion symmetry, the strength of Dresselhaus SOC is negligible. On the contrary, Rashba effect dominates the SOC in graphene because the potential rapidly changes within an atomically thin distance. With the existence of strong Rashba SOC, recently scientists have experimentally observed the spin-Hall effect in a suspended graphene monolayer [16]. For other monolayer materials with central symmetry breaking like MoS₂, their SOC terms can be just simply viewed as the combination of both effects.

In addition, both Dresselhaus and Rashba SOC have spin locking effect with the linear momenta \mathbf{p} . Followed by definition of spin expectation $\langle s \rangle = \langle \psi | \boldsymbol{\sigma} | \psi \rangle$, where $|\psi\rangle$ denotes the

eigenfunction defined by Hamiltonian, Fig. 2.8 depicts the spin textures* for both types of SOC and their combination. Fig. 2.8a illustrates a spin texture for Rashba SOC that spin vectors are always perpendicular to the momentum. This unique spin-lock feature is the fingerprint of Rashba SOC. Also, the spin texture of Dresselhaus SOC are shown in Fig. 2.8b. The spin vectors are parallel to k_x and k_y axis but align in different directions. Fig. 2.8c adds the equal magnitude of both SOC's together, making all spin vectors be parallel in $[110]$ direction. It is worth noting that both SOC formalisms are based on the 2D plane waves. When it comes to the realistic system, one should be careful to apply these formulas since inversion symmetry breaking not only generates an extra electric field \mathbf{E}_z , but also makes electron wavefunctions distort, which causes the invalidity of plane-wave approximations. But still, Dresselhaus and Rashba SOC are good approximations that help us study the underlying physics in spintronics.

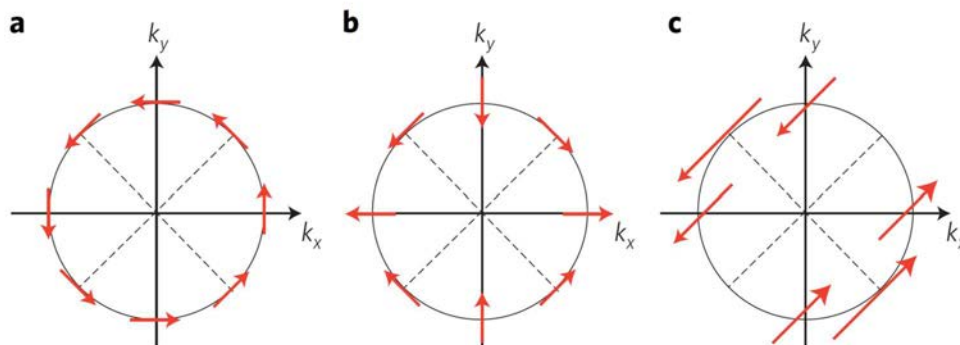


Fig. 2.8: Spin locking effect for Dresselhaus and Rashba SOC. (a) Spin textures for (a) Rashba and (b) Dresselhaus SOC around a \mathbf{k} circle. (c) The addition of both SOC terms.

2-2.4: Haldane Model

Before presenting Haldane model in detail, it is crucial to review the knowledge of quantum Hall effect in 1985. As introduced in chapter one, K. von Klitzing discovered quantum Hall

* The distribution of spin vectors in materials can generate different structures based on the interactions, such as SOC. These structures are so-called spin texture, which is useful to recognise distinct physics in spintronics.

effect [1]. The experiment was achieved under strong external magnetic field and extremely low-temperature environment. The external field is crucial because it is the source of anomalous velocity which generates Hall current in bulk materials. Nevertheless, in 1988, F. D. M. Haldane claimed that it is essential to break TR symmetry for the quantum Hall effect [33] yet the application of magnetic field is just one of the methods to satisfy this condition. As a result, it is likely that a system in the absence of the net magnetic amplitude can still contain quantised Hall conductance. He proposed a solvable tight-binding model, which exhibits no net magnetic field, expressed as [33]

$$H_{\text{Haldane}} = t_1 \sum_{\langle i,j \rangle} c_i^\dagger c_j + t_2 \sum_{\langle\langle i,j \rangle\rangle} e^{-iv_{ij}\phi} c_i^\dagger c_j + m_{\text{eff}} \sum_i (-1)^i c_i^\dagger c_i + h.c., \quad (2-37)$$

where $\langle\langle \ \ \rangle\rangle$ means the next nearest neighbours, t is the hopping parameter between atoms, m in the third term is the same as in Eq. (2-27), and $v_{ij} = \text{sgn}(\mathbf{R} \times \mathbf{r}) = \pm 1$, where \mathbf{R} and \mathbf{r} are unit vectors along two bonds (see Fig. 2.9a). Although the total magnitude is zero, one can assume, in principle, a complex phase $e^{-iv_{ij}\phi}$ is realised by applying staggered magnetic field which is positive near the centre of each hexagon lattice and negative around the edge ($m_{\text{eff}} = 0$). In the same manner, we consider a graphene with the infinite lattice. Its Hamiltonian can be written as

$$H_{\text{Haldane}} = \begin{pmatrix} H_{11} & H_{12} \\ H_{21} & H_{22} \end{pmatrix} = H_0 I + H_x \sigma_x + H_y \sigma_y + H_z \sigma_z. \quad (2-38)$$

Each component in H_{Haldane} is given by

$$H_0 = (H_{11} + H_{22})/2 = -2t_2 \cos \phi \sum_i \cos(\mathbf{k} \cdot \mathbf{r}_i), \quad (2-39)$$

$$H_x = \text{Re}\{H_{21}\} = -t_1 \sum_i \cos(\mathbf{k} \cdot \mathbf{R}_i), \quad (2-40)$$

$$H_y = \text{Im}\{H_{21}\} = -t_1 \sum_i \sin(\mathbf{k} \cdot \mathbf{R}_i), \quad (2-41)$$

$$H_z = (H_{11} - H_{22})/2 = -2t_2 \sin \phi \sum_i \sin(\mathbf{k} \cdot \mathbf{r}_i). \quad (2-42)$$

in which $i = 1, 2, 3$. It is straightforward to calculate the energy eigenvalue of (2-38) that is

$$\varepsilon_{\pm} = H_0 \pm \sqrt{H_x^2 + H_y^2 + H_z^2}. \text{ At K and K' points, } H_x = H_y = 0, \text{ but } H_z \neq 0. \text{ Thus, in between}$$

two bands, there is a gap whose width is equal to

$$\varepsilon_+ - \varepsilon_- = 2|H_z| = 6\sqrt{3}t_2 \sin \phi, \quad (2-43)$$

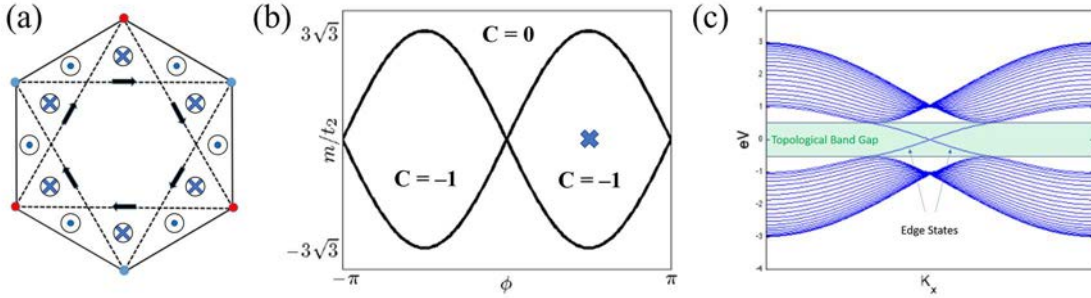


Fig. 2.9: Haldane model. By setting the hopping parameter $t = 1$ and $t_2 = 0.1$, (a) Haldane model indicating nearest-neighbour bonds (black solid lines) and next-nearest-neighbour bonds (dashed lines). Red and blue points, respectively, mark the A and B sub-lattice sites. Arrows for next-nearest-neighbour bonds indicate the directions of positive phase hopping. The dot and cross illustrate the direction of staggered magnetic fields. (b) Phase diagram of the Haldane model and this figure assumes that t_2 is positive. The solid line indicates a topological phase transition boundary. Inside the enclosed region, topological edge states arise due to non-zero Chern number. Correspondingly, (c) the projected band structure calculated by Haldane model [33] with the chosen parameters $m = 0$ and $\phi = \pi/2$ as marked in (b). The green shaded area shows the topologically non-trivial gap and there are a pair of edge states within the gap.

where the signs define upper and lower energy band at K point. Since $\varepsilon_+ = -|\varepsilon_-|$ at two Dirac points, the opposite sign for H_z^K and $H_z^{K'}$ results in energy band inversion. Therefore, TR symmetry has been broken in this model, but the net magnetic field remains zero. This band flips for K and K' point provide an opportunity to turn a flat edge state (if exists) becomes the gapless one within the bulk bandgap. Moreover, we calculate Chern number to check its topological order by using the method mentioned in section 2.1. As shown in Fig. 2.9b,

effective mass m can be set as $m \neq 0$, and then $H_z^K = m_{eff} - 3\sqrt{3}t_2 \sin \phi$ and $H_z^{K'} = m_{eff} + 3\sqrt{3}t_2 \sin \phi$. In the Haldane model, $|m_{eff}| = 3\sqrt{3}t_2 \sin \phi$ gives a topological phase transition curve. As long as $|m_{eff}| < 3\sqrt{3}t_2 \sin \phi$, the system keeps its topological phase, otherwise the system converts into a topologically trivial case. With the parameter $m = 0$ and $\phi = \pi/2$, Fig. 2.9c illustrates a pair of gapless edge states within a topological bandgap.

2-2.5: Kane-Mele Model

Although Haldane indicated an unusual property via a simple staggered magnetic field model, it was quite hard to achieve his model, because in that time arranging stagger magnetic fields was a challenging task. Despite that, inspired by Haldane's work, Kane and Mele gave a possible picture realised by the nature of spin-orbit coupling in graphene in 2005 [5-6]. They proposed a Hamiltonian expressed as [6]

$$H_{KM} = -t_1 \sum_{\langle i,j \rangle} c_i^\dagger c_j + m_{eff} \sum_i (-1)^i c_i^\dagger c_i + i\lambda_{SO} \sum_{\langle\langle i,j \rangle\rangle} v_{ij} c_i^\dagger s_z c_j + i\lambda_R \sum_{\langle i,j \rangle} c_i^\dagger (\mathbf{s} \times \hat{\mathbf{d}}_{ij})_z c_j, \quad (2-44)$$

where $s_z = \pm 1/2$ are spin along $\pm z$ components, m_{eff} is the strength of the effective mass term, λ_{SO} is the spin-orbit coupling hopping parameter, the fourth term is the contribution of the Rashba spin-coupling, and other parameters are same as Eq. (2-37). For brevity, by setting Rashba parameter λ_R equals to zero, one can find that Kane-Mele (KM) model is a special case of Haldane model combining $\phi = \pm \pi/2$, so H_{KM} is written as

$$H_{KM} = \begin{bmatrix} H_\uparrow & 0 \\ 0 & H_\downarrow \end{bmatrix} = \begin{bmatrix} H_{\text{Haldane}}(\phi = \pi/2) & 0 \\ 0 & H_{\text{Haldane}}^*(\phi = -\pi/2) \end{bmatrix}. \quad (2-45)$$

Therefore, KM model is a $4N \times 4N$ matrix with a spin-up element in the up-left block and a spin-down one in the bottom-right block. Since both Hamiltonians are complex conjugates, in the following, only spin-up Hamiltonian is discussed. Keeping $\lambda_R = 0$, we deduce the low-energy spin-dependent Hamiltonian in momentum space

$$H_{SO} = \Delta_{SO} \tau_z \sigma_z S_z, \quad (2-46)$$

where $\Delta_{SO} = 3\sqrt{3}\lambda_{SO}$, $\tau_z = \pm 1$. For spin-up case $S_z = 1$, substituting Eq. (2-46) into Eq. (2-27), and then we have [6]

$$H_+(\mathbf{k}) = v(k_x \sigma_x + k_y \sigma_y) + (m_{eff} + \Delta_{SO}) \sigma_z, \quad (2-47)$$

$$H_-(\mathbf{k}) = v(-k_x \sigma_x + k_y \sigma_y) + (m_{eff} - \Delta_{SO}) \sigma_z. \quad (2-48)$$

As argued in section 2-2.3, if $m_{eff} < \Delta_{SO}$, the topological phase transition occurs and graphene becomes a topological insulator. Using the same procedure in section 2-2.3, we have the spin-dependant Hamiltonian

$$H_\alpha = \begin{bmatrix} m_{eff} - \alpha P_2 & P_1 & P_3 & & & & \\ P_1 & \alpha P_2 - m_{eff} & t & & -P_3 & & \\ P_3 & t & m_{eff} - \alpha P_2 & P_1 & P_3 & & \\ & -P_3 & P_1 & \alpha P_2 - m_{eff} & t & & \\ & & P_3 & t & & \ddots & \end{bmatrix} \quad (2-49)$$

where $\alpha = \pm 1$ standing for spin-up and down; $P_1 = 2t \cos(\sqrt{3}ka/2)$, $P_2 = 2\lambda_{SO} \sin(\sqrt{3}ka)$ and $P_3 = 2\lambda_{SO} \sin(\sqrt{3}ka/2)$. In Fig. 2.10a, solved from Hamiltonian (2-49), gapless edge states in the topologically non-trivial bandgap are shown. The corresponding Chern numbers of bands are equal to the ones given by Haldane's zero-net-magnetic-field model. Interestingly, the TR

symmetry is broken by intrinsic spin-orbit coupling separately for each spin. But if taking the both spin degree of freedom into account, TR symmetry in the system is preserved. In other words, in the Chern insulator point of view, the summation of topological order for every band is zero. The spin Chern number, however, is defined as $\Delta C = C_{\uparrow} - C_{\downarrow}$, which gives an integer two. Consequently, a quantised conductance for electronic transport in graphene is collected. In Fig. 2.10b-c, the system with Rashba SOC and staggered energy terms is considered. As illustrated, two distinct topological phases are presented as the magnitudes of λ_R and λ_v change. For the cases with non-zero λ_R and m_{eff} , the interpretation of spin Chern number difference is no longer valid since the Hamiltonian is not a block-diagonal form anymore. To distinguish its topological phases, another topological invariant is needed for a system exhibiting symmetry-protected edge states such as topological insulators.

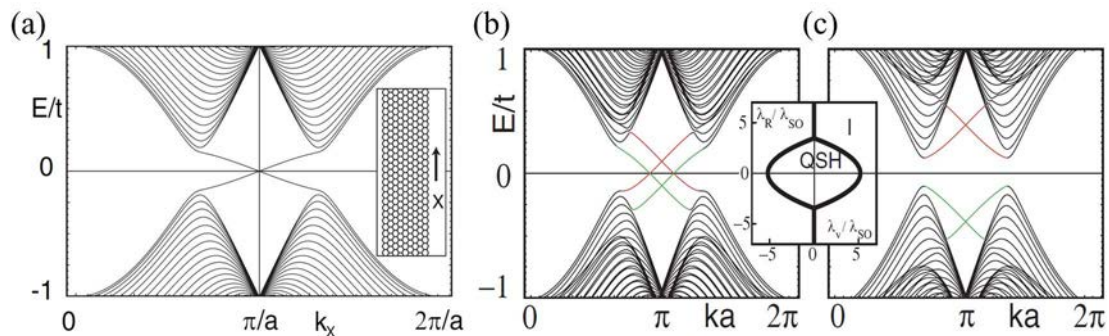


Fig. 2.10: Kane-Mele Model.

(a) KM model in the absence of Rashba and effective mass term, indicating two degenerate pairs of edge state with parameter $\lambda_{so}/t = 0.03$. The inset illustrates a graphene nanoribbon truncated with zigzag boundaries. In the presence of the Rashba and on-site staggered energy terms, as their magnitudes change, the system may experience a topological phase transition from (b) non-trivial bandgap with $\lambda_v/t = 0.1$ to (c) trivial bandgap with $\lambda_v/t = 0.4$, which demonstrate a phase transition that cannot be explained by Chern number interpretation. The SOC parameters for both (b) and (c) cases are given by $\lambda_{so}/t = 0.06$, $\lambda_R/t = 0.05$. The inset between (b) and (c) shows that, inside the quantum spin Hall region, there exist topological insulating phases. Above figures have been reproduced from ref. [5-6]

To clarify the relation between edge states with distinct Z_2 invariants, we consider the edge states in a semi-infinite graphene sheet (one boundary only). In Fig. 2.11, for brevity, we take only one spin degree of freedom as an example. Correspondingly, there exists one edge

state because it is a single boundary system. Due to the bulk band inversion highlighted by green and blue triangles, it results in two different edge state connections leading to the discrepancy of Z_2 topological index. When electrons hit a defect or impurity, at the same Fermi energy point, there is a backscattering mode ($k_x \rightarrow -k_x$) for the electronic transport in a $Z_2 = 0$ system, which stands for a topologically trivial scenario. On the contrary, as non-reflecting modes are supported at the point $-k_x$, electrons “bypass” the disorder in the $Z_2 = 1$ system, which leads a topologically protected transport.

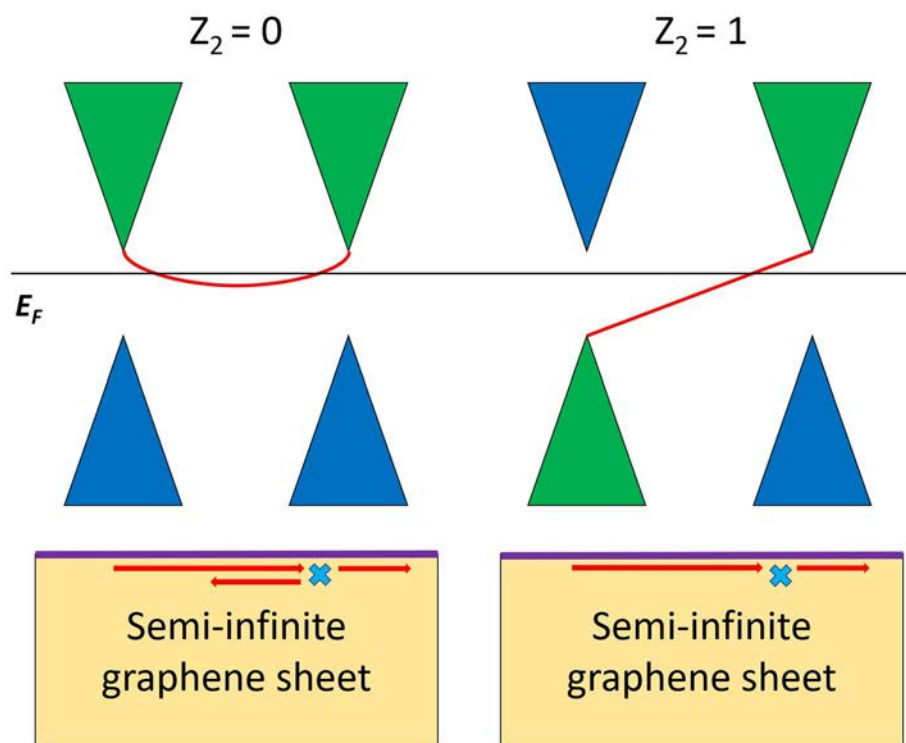


Fig. 2.11: Edge States with Distinct Z_2 index.

The green and blue areas illustrate bulk regions, the red lines and arrows represent edge states, the cyan cross is a defect, and the purple lines highlight the single boundary of a semi-infinite graphene sheet. The left figure indicates a topologically trivial electronic transport since it supports backscattering mode while propagating electrons hit a defect. Yet, the right figure shows a quite different scenario that electrons propagate around the defect without backscattering because no modes supports reflection.

Before ending this section, we want to briefly review the discovery of the topological insulating phase to emphasise its importance in condensed-matter physics. Due to the result of quantum Hall effect, theoretical physicists once thought that the application of magnetic fields

is inevitable. Yet, after Haldane's influential model, even though it was impractical to have staggered magnetic fields in that time, the concept of applying magnetic fields has been replaced with the one of breaking TR symmetry. Ever since, theoretical physicists considered this rule as a sufficient condition to have topological/quantised electronic transports until the proposal of KM model. In KM model, the topologically protected transport is actually guaranteed by TR symmetry. In other words, when TR symmetry is broken, KM model turns into a trivial insulator. With this entirely opposite conclusion, KM model became another conceptual revolution in the history of condensed-matter theory. Additionally, as stated in the previous paragraph, Chern number interpretation could not fully explain the transition between trivial and topological insulating phase. Thus, in the next section, we will discuss a new index called Z_2 topological invariant.

2-3: Z_2 Topological Invariant

2-3.1: Z_2 Invariant in the KM Model

As mentioned at the end of the previous section, the method of total Chern numbers fails to define the result demonstrated by KM model. Although it seems that the interpretation of spin Chern number can explain the topological transport in KM model without staggered and Rashba terms, a new topological order is required to have a generalised description of this novel topological materials. To build a rigorous theory, C. Kane and E. Mele proposed a new type of topological order so-called " Z_2 invariant" that is distinguished from the conventional Chern numbers which can also be referred as " Z invariant", where " Z " means integer as the definition in mathematics. Z_2 invariants describe a simple set containing two elements $[0,1]$. If the Z_2 number of a system is zero/one, it carries a topologically trivial/non-trivial insulating phase. Subsequently, the case with non-trivial Z_2 invariant will be discussed.

In fact, the first example of Z_2 topological materials in the history of physics is KM model. In ref. [6], a matrix $b_{ij} = \langle u_i(\mathbf{k}) | \hat{\Theta} | u_j(\mathbf{k}) \rangle$ is defined, where $\hat{\Theta}$ is the TR operator and $|u_i(\mathbf{k})\rangle = e^{-i\mathbf{k}\cdot\mathbf{r}} |\psi_i(\mathbf{k})\rangle$ is the periodic part of Bloch waves (Bloch wavepacket). It can be readily proved that b_{ij} is an anti-symmetric matrix, i.e. $b_{ij} = -b_{ji}$. As an anti-symmetric matrix, it yields $P(\mathbf{k}) = pf[b_{ij}]$ whilst define Pfaffian of, and then the Z_2 invariant of this system can be decided by solving the zeros of $P(\mathbf{k})$ in half Brillouin zone (HBZ). As demonstrated in [6], zeros of Pfaffian are illustrated in two types as depicted in Fig. 2.12. In Fig. 2.12a, if the zeros discretely distribute in HBZ, the Z_2 number is the parity of the number of zeros enclosed within the path C ; if the zeros occur along a continuous line instead of points as shown in Fig. 2.12b, in this case the Z_2 index are given by the half times of the sign change along the loop C . Combining both cases, the Z_2 index can thus be written as [6]

$$Z_2 = \frac{1}{2\pi i} \oint_C d\mathbf{k} \cdot \nabla_{\mathbf{k}} \ln [P(k + i\delta)] \text{ mod } 2, \quad (2-50)$$

where C is the boundary of HBZ and δ is added to avoid the divergence of integration.

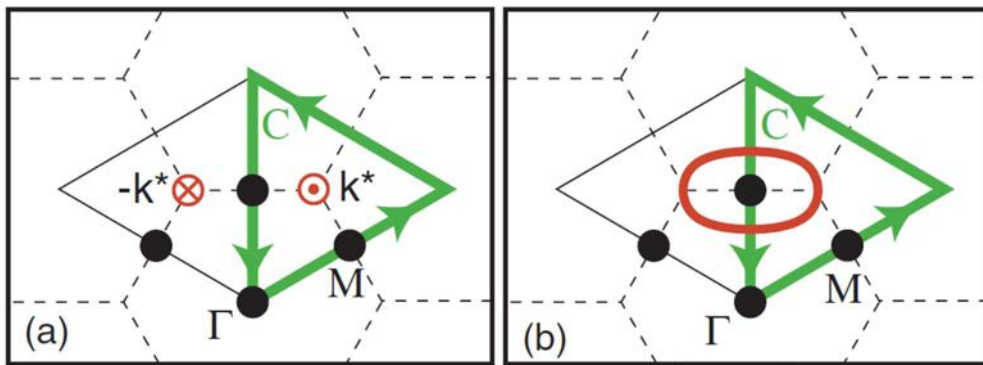


Fig. 2.12: The zeros of $P(\mathbf{k})$ in the topological insulating phase. It emerges at points \mathbf{k} for (a) $m_{eff} \neq 0$ and on the loop for (b) $m_{eff} = 0$. Above figures have been reproduced from ref. [6].

2-3.2: Kramers Theorem

Prior to introducing the meaning of Z_2 topological invariant, a simple but extremely essential theorem named after Hans Kramers [34] needs to be discussed. In quantum mechanics, Kramers theorem states that, if a half-integer-spin system is invariant under TR operation, there are at least a pair of doubly degenerate states. Normally these two degenerate states are called Kramers pair; there are always demonstrated as a match a pair. A straightforward proof is given as follows.

The system is invariant under TR operation, in other words, the TR operator $\hat{\Theta}$ commutes with the Hamiltonian. Thus, the eigenstates $|u\rangle$ have the same energy as $\hat{\Theta}|u\rangle$. Besides, since the TR operator is anti-unitary, the relation $\langle \hat{\Theta}u | \hat{\Theta}v \rangle = \langle v | u \rangle$ holds for an anti-unitary operator and $\langle u | \hat{\Theta}u \rangle = \langle \hat{\Theta}^2 u | \hat{\Theta}u \rangle = -\langle u | \hat{\Theta}u \rangle \rightarrow \langle u | \hat{\Theta}u \rangle = 0$. As a result, eigenstates $|u\rangle$ and $\hat{\Theta}|u\rangle$ are orthogonal and have the identical energy, i.e. they are degenerate states. In the next section, we will show that the relation between Kramers theorem and Z_2 topological index.

2-3.3: Time-Reversal Polarisation and Z_2 Invariant

To clarify the physical meaning of Z_2 invariant, L. Fu and C. Kane proposed a perspective called “time-reversal polarisation (TRP)” that connects the abstract Z_2 concept with an imaginable picture. Firstly, let us review the quantum theory for modern (electric charge) polarisation. Considering a periodic system, the corresponding Bloch function for n th band is $|\psi_n(\mathbf{k})\rangle = e^{i\mathbf{k}\cdot\mathbf{r}} |u_n(\mathbf{k})\rangle$. Thus, one can define Wannier functions in terms of the lattice \mathbf{R} as

$$|\mathbf{R}, n\rangle = \frac{1}{2\pi} \int d\mathbf{k} e^{-i\mathbf{k}\cdot(\mathbf{R}-\mathbf{r})} |u_n(\mathbf{k})\rangle. \quad (2-51)$$

Note that Wannier function is not unique, since it depends on the choice of gauge for $|u_n(\mathbf{k})\rangle$. In ref. [35], the authors gave an instruction of choosing a unitary transformation to optimise the localization of Wannier functions. However, here we only consider the total polarisation which is insensitive to the choice of the gauge. For occupied bands at $\mathbf{R} = 0$, the polarisation is defined by the sum over all the centres of Wannier functions, which yields

$$P = \sum_n \langle 0, n | \mathbf{r} | 0, n \rangle = \frac{1}{2\pi} \oint d\mathbf{k} \cdot \mathcal{A}(\mathbf{k}) \quad (2-52)$$

where $\mathcal{A}(\mathbf{k})$ is the Berry connection as previously stated. To put it simply, in the following only a 1D Brillouin zone is considered and the theory can be readily extended to higher dimensions. If we introduce a parametric space t , the Hamiltonian of systems $H(t)$ changes while t adiabatically evolves. The change of polarisation ΔP is thus given by

$$P(t_2) - P(t_1) = \frac{1}{2\pi} \left[\oint_{c_2} dk A(k) - \oint_{c_1} dk A(k) \right], \quad (2-53)$$

where the loop $c_{1(2)}$ is from $-\pi$ to π for certain $t_{1(2)}$. According to the Stoke's theorem, Eq. (2-53) can be rewritten as

$$P(t_2) - P(t_1) = \frac{1}{2\pi} \int_S dt dk \Omega(t, k), \quad (2-54)$$

where Ω is Berry curvature and S represents the surface spanned by parameter t and wavevector k . For periodic cases $H(t+T) = H(t)$, Eq. (2-54) gives the integral throughout the whole torus with respect to t and k , and it defines a Berry phase as expressed in (2-4). Nevertheless, as the P and TR symmetry are both preserved, the Berry curvature is equal to zero so that the change of polarisation vanishes in this scenario.

With the definition of charge polarisations, it enables the analysis of Z_2 index by extending the similar perspectives. In section 2.2.4, Kramer theorem indicates that there must exist two-fold degeneracy, provided that the system is invariant under TR operation. In this case we assume there is no extra degeneracy except those guaranteed by Kramer theorem. Therefore, the $2N$ eigenstates are split into N pairs that satisfy [35]

$$|u_{-k,n}^I\rangle = -e^{i\zeta_{k,n}} \hat{\Theta} |u_{k,n}^{II}\rangle, \quad (2-55)$$

$$|u_{-k,n}^{II}\rangle = e^{i\zeta_{-k,n}} \hat{\Theta} |u_{k,n}^I\rangle, \quad (2-56)$$

where $n=1\cdots N$. Note that Eq. (2-55) and (2-56) imply that the same labelling eigenstates are distinct in $\pm k$ region such that the Brillouin zone must be cut into half during the analysis. This explains, in the previous section, only half Brillouin boundaries are considered in Z_2 number calculation. Plugging Eq. (2-55) and (2-56) into Eq. (2-53), the partial polarisations labelled by $s = I, II$ read $P^s = (2\pi)^{-1} \int_{-\pi}^{\pi} dk \mathcal{A}(k)$ with $\mathcal{A}^s(k) = i \sum_n \langle u_{k,n}^s | \nabla_k | u_{k,n}^s \rangle$. To keep the polarisation invariant, one should separate the positive and negative k regions that leads to

$$P^I = (2\pi)^{-1} \int_0^{\pi} dk [\mathcal{A}^I(k) + \mathcal{A}^I(-k)]. \quad (2-57)$$

Also, given by Eq. (2-54), the Berry connection obeys the gauge condition

$$\mathcal{A}^I(-k) = \mathcal{A}^{II}(k) - \sum_n \nabla_k \zeta_{k,n}. \quad (2-58)$$

Thus, Eq. (2-58) becomes

$$P^I = (2\pi)^{-1} \left[\int_0^{\pi} dk \mathcal{A}(k) - \sum_n (\zeta_{\pi,n} - \zeta_{0,n}) \right], \quad (2-59)$$

where $\mathcal{A}(k) = \mathcal{A}^I(k) + \mathcal{A}^{II}(k)$. Based on ref. [35], L. Fu and C. Kane suggested that the time-reversed wave functions can be linked to the second term of Eq. (2-59). This time-reversed function is written as

$$w_{mn} = \langle u_{-k,m} | \hat{\Theta} | u_{k,n} \rangle. \quad (2-60)$$

At points $k = 0$ and $\pm\pi$, w_{ij} is an anti-symmetric matrix composed of the direct product of several 2×2 matrices with only $e^{i\zeta_{k,n}}$ and $-e^{i\zeta_{-k,n}}$ on its off-diagonal terms. Moreover, as an anti-symmetric matrix, w_{ij} can be categorised by its Pfaffian. With Eq. (2-60), one could prove that the second term of (2-59) is connected to (2-60) via the equation [35]

$$\frac{\text{Pf}[w(\pi)]}{\text{Pf}[w(0)]} = \exp\left(i \sum_n (\zeta_{\pi,n} - \zeta_{0,n})\right). \quad (2-61)$$

Thus, the second term of (2-59) leads to

$$P^I = (2\pi)^{-1} \left[\int_0^\pi dk \mathcal{A}(k) + i \ln \left\{ \frac{\text{Pf}[w(\pi)]}{\text{Pf}[w(0)]} \right\} \right], \quad (2-62)$$

In the same manner, another partial polarisation P^{II} can be obtained. By following the identical definition, the TRP is the difference

$$\Delta = (2\pi)^{-1} \left[\int_0^\pi dk \mathcal{A}(k) - \int_{-\pi}^0 dk \mathcal{A}(k) + 2i \ln \left\{ \frac{\text{Pf}[w(\pi)]}{\text{Pf}[w(0)]} \right\} \right]. \quad (2-63)$$

Comparing Eq. (2-63) with (2-50), the TRP has the similar mathematical expression as Z_2 number so that this may indicate the equivalence of TRP and Z_2 invariant. Eq. (2-63) can be rewritten associated with w_{mn} as

$$\Delta = (2\pi i)^{-1} \left[\int_0^\pi dk \text{Tr} [w^\dagger \nabla_k w] - 2 \ln \left\{ \frac{\text{Pf}[w(\pi)]}{\text{Pf}[w(0)]} \right\} \right], \quad (2-64)$$

or further simplified as

$$\begin{aligned} \Delta &= (2\pi i)^{-1} \left[\int_0^\pi dk \nabla_k \ln \det [w(k)] - 2 \ln \left\{ \frac{\text{Pf}[w(\pi)]}{\text{Pf}[w(0)]} \right\} \right] \\ &= \frac{1}{\pi i} \left\{ \ln \left[\frac{\sqrt{\det[w(\pi)]} \text{Pf}[w(0)]}{\sqrt{\det[w(0)]} \text{Pf}[w(\pi)]} \right] \right\}. \end{aligned} \quad (2-65)$$

Since the value of $\text{Pf}[w(\pi)]/\sqrt{\det[w(\pi)]}$ must be ± 1 , a simpler expression of TRP yields

$$(-1)^\Delta = \frac{\sqrt{\det[w(0)]}}{\text{Pf}[w(0)]} \frac{\sqrt{\det[w(\pi)]}}{\text{Pf}[w(\pi)]}. \quad (2-66)$$

Eq. (2-63) to (2-66) are the main results which can be used for connecting Z_2 indices with TRP.

To verify it, one can regard parametric space t as time and the function w_{mn} is invariant under TR operation at certain points, e.g. 0 or $\pm\pi$ for the current case.

With the aid of the above discussion, we can argue that the evolution of the Hamiltonian around the cycle can be regarded as the change of the TRP, and half circle of that cycle results in a Z_2 index, which causes a Z_2 spin pump from a topologically non-trivial case. The meaning of this index can be linked to the shift in the Wannier centres during a period. Fig. 2.13a illustrates the centres of Wannier orbitals as a function in terms of time. At three time-reversal invariant points $t=0$, $T/2$, and T , TR symmetry guarantees that Wannier states are formed as a time-reversed pairs. However, for a topologically non-trivial case shown in Fig. 2.13b, Wannier states remain time-reversal pairs but switch partners from $t=0$ to $T/2$. During this process, the TRP evolves along the difference between the positions of TR Wannier states, leading to non-

trivial topological states. In other words, Z_2 invariant can be regarded as a “switch” that tells us whether the topological insulating phase has been turned on or not.

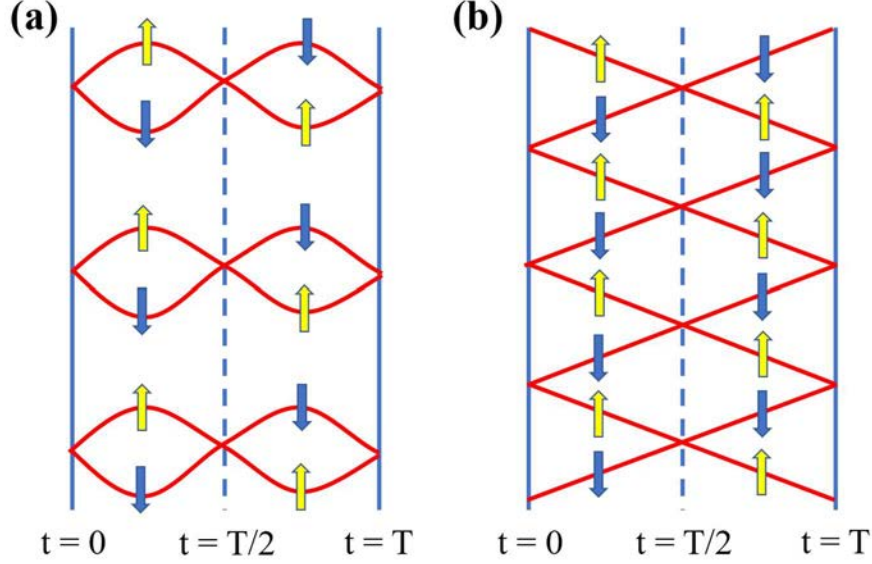


Fig. 2.13: Two evolution types of TRP. Horizontal direction represents parametric axis, say time axis. The vertical axis is considered as Wannier orbits or 1D atomic chains along boundaries. Yellow and cyan arrows respectively demonstrate the evolution of two spin degrees of freedom. (a) Trivial electronic transport: The evolution of electrons returns its initial states. No spin current occurs under this situation, (b) Non-trivial electronic transport: electrons switch partner at every TRIM which causes opposite propagation for two distinct spin currents. [35]

While Wannier state evolves from $t = T/2$ to T , there is another switch making the TRP revisits to its original state. Nevertheless, At the open boundaries, the system will not revisit its initial state but it ends up moving to the next Wannier orbit owing to the crossing at $t=T/2$. To link the topological characteristic with this unusual evolution at boundaries from $t=0$ to $T/2$, we consider the change in the TRP $P_\theta(t)$ yielding [35]

$$\Delta = [P_\theta(T/2) - P_\theta(0)] \text{ mod } 2. \quad (2-67)$$

The difference above is gauge-dependent and it gives a Z_2 topological characteristics which is evaluated by the wave functions $|u_{k,n}(t)\rangle$ mapping onto the torus spanned by two parameters k and t . From Eq. (2-67), this difference is written as

$$(-1)^\Delta = \prod_{i=1}^4 \frac{\sqrt{\det[w(\Gamma_i)]}}{\text{Pf}[w(\Gamma_i)]}. \quad (2-68)$$

Here Γ_i are the “time-reversal invariant momenta” (TRIM), i.e. TR symmetry is preserved at these points. In 2D case, there exist 4 TRIMs in a Brillouin zone as shown in Fig. 2.14a. For 3D cases, 8 TRIMs emerge to categorise three distinct faces surrounded by 4 TRIMs as shown in Fig. 2.14b. Each face defines a Z_2 index so three indices $\{v_1 v_2 v_3\}$ are obtained. Apart from them, the product of all 8 indices defines an additional Z_2 index v_0 so that we obtain a set of Z_2 indices $\{v_0; v_1 v_2 v_3\}$ that classify topological insulating phase in three dimensions. In the next section, a detailed discussion of 3D topological insulators will be given.

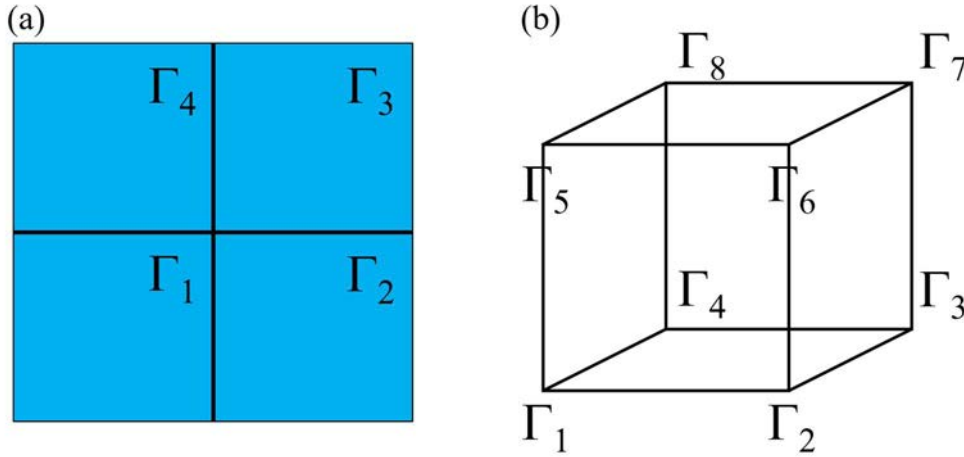


Fig. 2.14: Schematic figures of TRIMs distributing on the (a) 2D and (b) 3D Brillouin zone.

2-3.4: Z_2 Invariant in Three Dimensions and Fu-Kane-Mele (FKM) Model

The content in the previous section can be intuitively extended to three-dimensional (3D) cases [36]. In any 3D periodic system, its TRIM Γ can be generally expressed by their linear combination of reciprocal lattice vectors \mathbf{b}_i as $\Gamma_{n_1 n_2 n_3} = \sum_{i=1}^3 (n_i \mathbf{b}_i) / 2$, where $n_i = 0, 1$. Thus, the TRPs associated with TRIM are given by [36]

$$\delta_{n_1 n_2 n_3} = \sqrt{\det \left[w \left(\Gamma_{n_1 n_2 n_3} \right) \right]} / \text{Pf} \left[w \left(\Gamma_{n_1 n_2 n_3} \right) \right]. \quad (2-69)$$

Here the unitary matrix $w_{mn} = \langle u_m(-\mathbf{k}) | \hat{\Theta} | u_n(\mathbf{k}) \rangle$. At $\mathbf{k} = \Gamma_{n_1 n_2 n_3}$, $w_{mm} = -w_{mm}$, so the Pfaffian $\text{Pf}[w]$ is defined. Note that a wavevector-dependent gauge transformation will change the sign of any product of two δ_i . However, the product of four δ_i , which encloses to a surface shown in Fig. 2.14a, is gauge invariant. This product describes the difference of TRP owing to the change of the flux defining the Z_2 invariant in 2D from two parameters $\Lambda_1 = 0$ to $\Lambda_2 = 0$. As stated previously, above discussion determines the existence of gapless chiral edge states. In 3D, 8 TRIMs are demonstrated in association with primitive reciprocal lattice $\Gamma_{n_1 n_2 n_3} = \sum_{i=1}^3 (n_i \mathbf{b}_i) / 2$, which can be visualised as 8 vertices of a cube in Fig. 2.14b. Each face can be regarded as a 2D Brillouin zone, leading to three indices $\{v_1 v_2 v_3\}$ for corresponding directions. Apart from that, the product of all 8 indices characterises another index, and we have four Z_2 topological indices $\{v_0; v_1 v_2 v_3\}$. Four Z_2 indices $(v_0; v_1 v_2 v_3)$ are defined by [36]

$$(-1)^{v_0} = \prod_{n_j=0,1} \delta_{n_1 n_2 n_3}, \quad (2-70)$$

$$(-1)^{v_i} = \prod_{n_{j \neq i}=0,1, n_i=1} \delta_{n_1 n_2 n_3}. \quad (2-71)$$

v_0 refers to the strong topological Z_2 index whereas v_i is the weak topological Z_2 indices. The values of these Z_2 indices categorise the system into strong topological insulators, weak topological insulators, and trivial insulators [36]. For $v_0 = 1$, the system is a strong topological insulator which possesses Dirac edge states along any momentum direction so that these edge states are the most robust ones; for $v_0 = 0$, it turns out two possibilities: one is a weak

topological insulator that can be regarded as a multiple stack of 2D topological insulator sheets, and another one is a trivial insulator without the exhibition of topologically protected edge states.

As an example, Fu *et. al.* [36] proposed 3D topological insulators known as FKM model, which considers diamonds with non-negligible spin-orbit coupling, whose Hamiltonian is

$$H = t \sum_{\langle i,j \rangle} c_i^\dagger c_j + i \frac{8\lambda_{so}}{a^2} \sum_{\langle\langle i,j \rangle\rangle} c_i^\dagger \mathbf{s} \cdot (\mathbf{d}_{ij}^1 \times \mathbf{d}_{ij}^2) c_j . \quad (2-72)$$

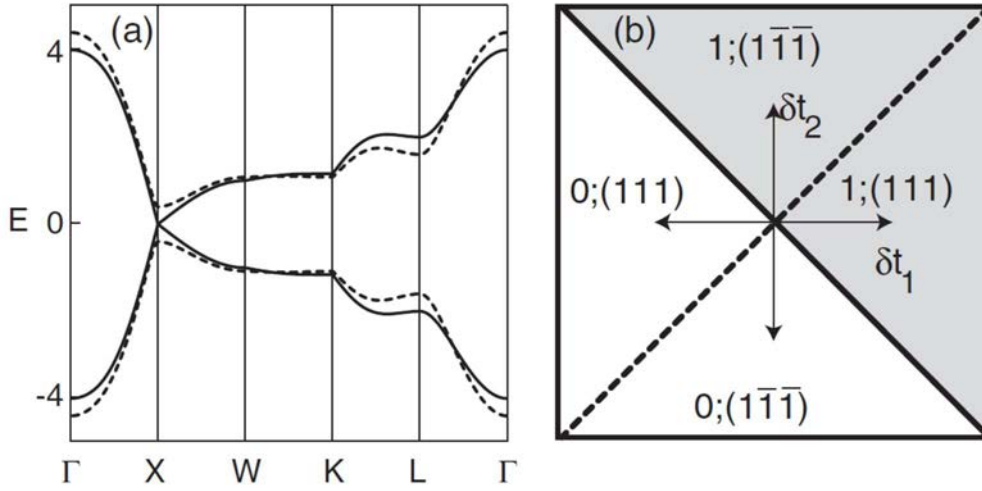


Fig. 2.15: Bulk band structure of 3D topological insulators.

(a) The band structure emulated by Eq. (2-72) with parameters $t = 1$ and $\lambda_{so} = 0.125$. The uppercase letters below it represent high symmetry points of a diamond structure. The dashed line illustrates the energy split due to $\delta t_1 = 0.4$. (b) The phase diagram in accordance with δt_1 (111) and δt_2 ($1\bar{1}\bar{1}$). The shaded area highlights the strong topological insulating phase. Above figures have been reproduced from ref. [36]

The first term is the nearest-neighbour (NN) hopping and the second one is the next-nearest-neighbour (NNN) hopping with intrinsic spin-orbit coupling. a is the lattice constant and $\mathbf{d}_{ij}^{1,2}$ are NN vectors traversed between atom location i and j . By solving the above Hamiltonian, one can obtain its band structures with and without SOC term in Fig. 2.15a. Without perturbed NN hopping parameters, there exists a four-fold degeneracy at X point, while with perturbation,

the degeneracy is gapped that topologically non-trivial edge states may emerge at material boundaries. Fig. 2.15b depicts the phase diagrams of strong and weak topological insulating phases for various perturbations on hopping parameters. In (111) and $(\bar{1}\bar{1}\bar{1})$ direction, a positively perturbed hopping parameter gives rise to strong topological phases, while weak topological phases result from a negative perturbation.

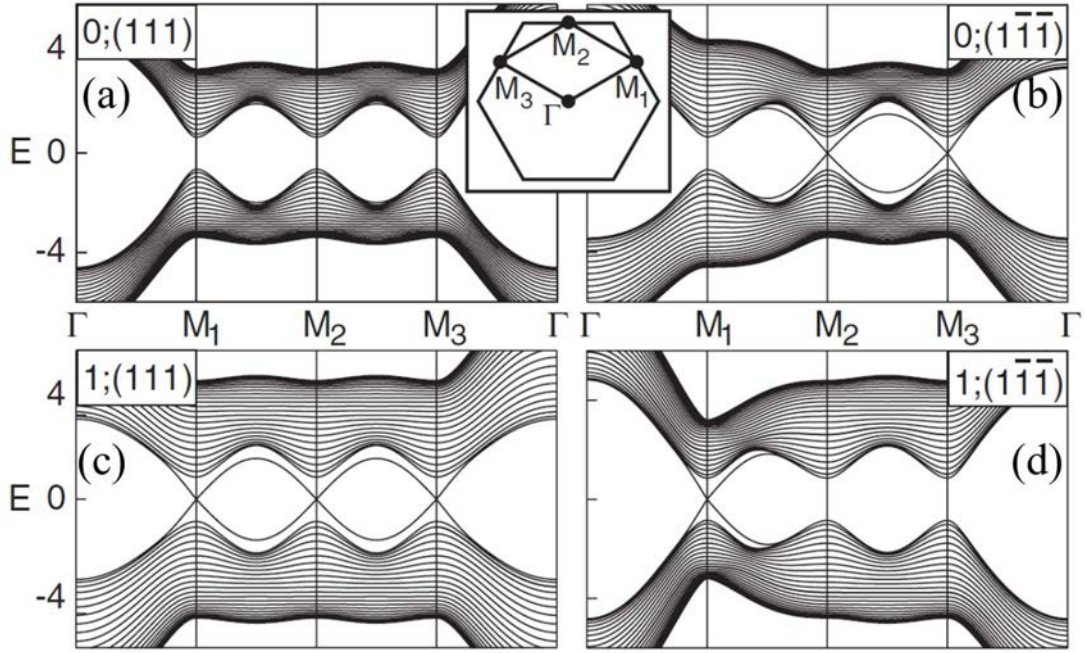


Fig. 2.16: Projected band structures of 3D topological insulators. With the same parameter in Fig. 2.15, for a slab with an 111 -truncated face, Figure (a) to (d) show four distinct topological phases in Fig. 2.15b. With the zero strong Z_2 index, the states in (a) and (b) give an even number of gapless edge states, which respectively correspond to trivial and weak topological insulators; With the non-zero strong Z_2 index, there are an odd number of edge states crossing within the bandgap. The inset is the surface Brillouin zone projected on 111 direction. Above figures have been reproduced from ref. [36]

The projected band structures solved from Hamiltonian (2-72) further prove the previous statements in Fig. 2.15a. For all figures in Fig. 2.16a-d, they are calculated along high symmetry lines and four TRIMs with the cases $\nu_0 = 0, 1$. With the zero strong Z_2 index, an evident full bandgap, which leads to a trivial insulator, can be viewed in Fig. 2.16a. While in Fig. 2.16b, an even number of Dirac cones at TRIMs in Fig. 2.16b show the emergence of weak topological insulators. In addition, as shown in Fig. 2.16c-d, for the case $\nu_0 = 1$ strong

topological insulating phases guarantee an odd number of edge-state crossing at TRIMs. Although this simple diamond model gives a nice pedagogic example for 3D topological insulators, it is unlikely to find the topological insulating phase in real diamond due to its extremely weak spin-orbit interaction. Yet, crystals with similar structures such as Bismuth provide a great candidate to realise 3D topological insulators. In fact, the semiconducting alloy $\text{Bi}_{1-x}\text{Sb}_x$ has been experimentally verified that it possesses strong topological insulating phases [37].

2-4: Parity-Time Symmetric Physics

2-4.1: Parity and Time-Reversal Symmetry

In 1998, Bender and Boettcher challenged the textbook aspects in their remarkable work that the realness of energy eigenvalues must arise from a Hermitian Hamiltonian. They proposed that quantum mechanical systems with a non-Hermitian Hamiltonian can actually have a set of eigenstates with real eigenvalues [18]. Ever since, novel quantum mechanical systems have been constructed based on such Hamiltonians. To give an overview, here we begin by introducing some fundamental concepts for parity (P), time-reversal (TR), and their combination PT symmetries. The PT symmetry of the Hamiltonian means that it commutes with the parity operator (spatial inversion) and $\hat{\Pi}$ the time-reversal operator $\hat{\Theta}$, i.e. $[\hat{H}, \hat{\Pi}\hat{\Theta}] = 0$. The action of the parity operator $\hat{\Pi}$ causes the change of sign of all coordinates $\mathbf{r} \rightarrow -\mathbf{r}$. As a result, three unit vectors pass from a right coordinate system to a left one, polar vectors change their direction to the opposite $\mathbf{r} \rightarrow -\mathbf{r}$, $\mathbf{p} \rightarrow -\mathbf{p}$, $\mathbf{E} \rightarrow -\mathbf{E}$, while axial vectors do not change $\mathbf{B} \rightarrow \mathbf{B}$. Here, \mathbf{r} is the spatial coordinate, \mathbf{p} is the momentum, and \mathbf{E} and \mathbf{B} are electric and magnetic fields. Since the expected value of a physical quantity operator in

quantum mechanics corresponds to its classical magnitude, the classical momentum and coordinate change their signs under spatial inversion. This means that $\langle \mathbf{p} \rangle$ and $\langle \mathbf{r} \rangle$ should also change their signs. Therefore, the momentum and coordinate operators are transformed under spatial inversion by the rule $\hat{\Pi}^+ \hat{\mathbf{r}} \hat{\Pi} = -\hat{\mathbf{r}}$ and $\hat{\Pi}^+ \hat{\mathbf{p}} \hat{\Pi} = -\hat{\mathbf{p}}$, where $\hat{\mathbf{r}}$ and $\hat{\mathbf{p}}$ are the coordinate and momentum operators. Accordingly, the angular momentum operator $\hat{\mathbf{J}}$ remains unchanged under spatial inversion: $\hat{\Pi}^+ \hat{\mathbf{J}} \hat{\Pi} = \hat{\mathbf{J}}$

In addition, the normalisation of the wave function should be preserved under spatial inversion, and therefore the parity operator is unitary $\hat{\Pi}^+ \hat{\Pi} = \hat{\mathbf{1}}$. Since the double application of the parity operation returns the system to the initial state, the only discrepancy shows in the wave functions is a phase factor $\hat{\Pi}^2 \psi(\mathbf{r}, t) = e^{i\theta} \psi(\mathbf{r}, t)$. Since the parity of the wave function should be an observable, the spatial inversion operator fulfils the condition of Hermiticity. The only phase factor for which the spatial inversion operator is unitary and Hermitian, i.e. $\hat{\Pi}^+ = \hat{\Pi}$, thus $\hat{\Pi}^2 \psi(\mathbf{r}, t) = \psi(\mathbf{r}, t)$. Assuming that the wave function is scalar and take linear unitary operator $\hat{\Pi}$ into account, we obtain that $\hat{\Pi} \psi(\mathbf{r}, t) = \psi(-\mathbf{r}, t)$. If the Hamiltonian of a system can be represented in the form of a polynomial in momentum and coordinate operators and $\hat{\Pi}^+ \mathbf{H}(\mathbf{p}, \mathbf{r}, t) \hat{\Pi} = \mathbf{H}(-\mathbf{p}, -\mathbf{r}, t)$. As the system does not change after the inversion of coordinates, we have the $\hat{\Pi}$ -invariant condition $\mathbf{H}(\mathbf{p}, \mathbf{r}, t) = \mathbf{H}(-\mathbf{p}, -\mathbf{r}, t)$.

The action of the time reversal operator $\hat{\Theta}$ means the change $t \rightarrow -t$ in all equations and time dependences of physical quantities. As a result, all physical quantities linearly dependent on the time derivative change their sign under time reversal $\mathbf{p} \rightarrow -\mathbf{p}$, $\mathbf{J} \rightarrow -\mathbf{J}$, whereas the time-independent physical quantities do not change $\mathbf{r} \rightarrow -\mathbf{r}$. Acting the operator onto the displacement, momentum, and angular momentum, we obtain the rules for transformations of

operators under time reversal: $\hat{\Theta}^+ \hat{\mathbf{r}} \hat{\Theta} = \hat{\mathbf{r}}$; $\hat{\Theta}^+ \hat{\mathbf{p}} \hat{\Theta} = -\hat{\mathbf{p}}$; $\hat{\Theta}^+ \hat{\mathbf{J}} \hat{\Theta} = -\hat{\mathbf{J}}$. Time reversal preserves the normalisation of the wave function. It has been well-known that the double action of the time reversal operation returns the system to the states depending on the types of particles, i.e. $\hat{\Theta}^2 \psi(\mathbf{r}, t) = \pm \psi(\mathbf{r}, t)$. If the wave function is a scalar and we take an antilinear and antiunitary operator $\hat{\Theta}$ into account, the time reversal rule for the wave function: $\hat{\Theta} \psi(\mathbf{r}, t) = \psi^*(\mathbf{r}, -t)$ is obtained. Similarly, for parity operator we find $\hat{\Theta}^+ \mathbf{H}(\mathbf{p}, \mathbf{r}, t) \hat{\Theta} = \mathbf{H}^*(-\mathbf{p}, \mathbf{r}, t)$. In the same manner, if the Hamiltonian of a system is invariant under time-reversal operation, i.e. $\mathbf{H}(\mathbf{p}, \mathbf{r}, t) = \mathbf{H}^*(-\mathbf{p}, \mathbf{r}, t)$. By combining conditions caused from P and T operators, we obtain the transformation of the Hamiltonian under the combined action of $\hat{\Pi}$ and $\hat{\Theta}$: $(\hat{\Pi} \hat{\Theta})^+ \mathbf{H}(\mathbf{p}, \mathbf{r}, t) (\hat{\Pi} \hat{\Theta}) = \mathbf{H}^*(\mathbf{p}, -\mathbf{r}, t)$. Therefore, a Hamiltonian is PT symmetric if [18]

$$\mathbf{H}(\mathbf{p}, \mathbf{r}, t) = \mathbf{H}^*(\mathbf{p}, -\mathbf{r}, t). \quad (2-73)$$

For Hamiltonians possessing the form $\hat{\mathbf{H}} = \hat{\mathbf{p}}^2/2m + V(\hat{\mathbf{r}})$ where m is the mass and V is the potential energy of the system, the PT-symmetry condition (2-62) reduces the requirement to

$$V(\mathbf{r}) = V^*(-\mathbf{r}). \quad (2-74)$$

2-4.2: PT Symmetric System in Quantum Mechanics

We are now in the position to discuss Bender's remarkable contribution of rewriting one fundamental assumption in quantum mechanics. Inspired by the work indicating the real and positive spectrum of the Hamiltonian $H = p^2 + ix^3$, Bender and Boettcher generalise the studies to a 1D Hamiltonian which extends the case into the complex plane. Remarkably, they enlarge the playground from the self-adjoint Hamiltonian to non-Hermitian problems whose eigenvalue spectra remains its positive realness. In other words, the Hermiticity is sufficient to

assure real eigenvalues and orthonormality of eigenstates, whereas it is not a necessary condition. The new class of Hamiltonians allows every entry of matrix to contain complex numbers so long as the Hamiltonians commute with PT symmetry, i.e. $[\mathbf{H}, \mathbf{\Pi}\mathbf{\Theta}] = 0$. Replacing Hermiticity with PT symmetric condition, one can construct non-Hermitian Hamiltonians such as the one proposed by Bender which is [18]

$$H = p^2 - (ix)^N, \quad (2-75)$$

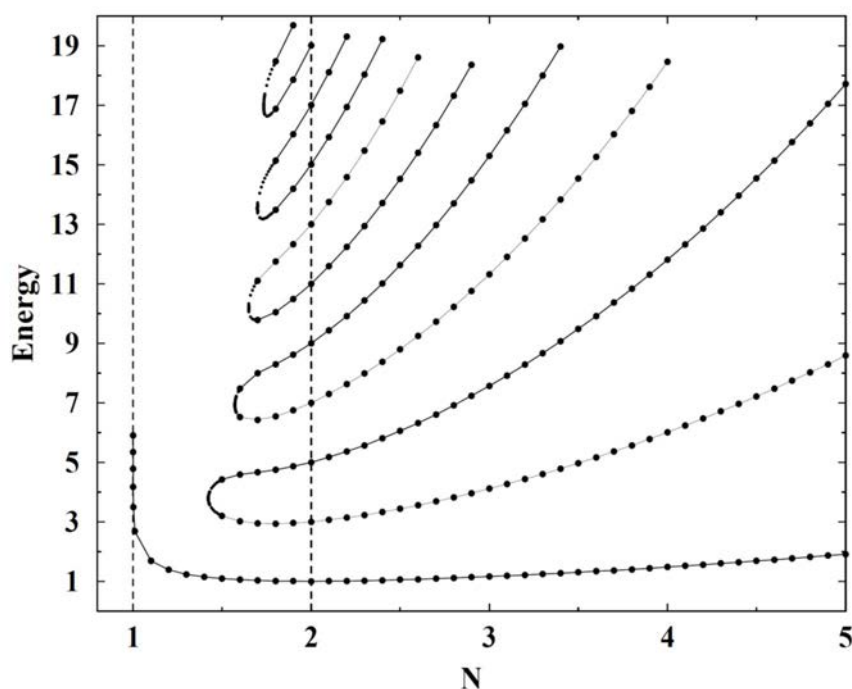


Fig. 2.17: Energy levels of the Hamiltonian (2-75). There are three regions of the energy spectra: Firstly, when $N \geq 2$ the spectrum consists of positive and real value. The lower bound of this region, $N = 2$, is exactly the simple harmonic oscillator whose energy levels equal $E_n = 2n+1$. Next, while $1 < N < 2$, there exist a finite number of real positive but an infinite number of complex eigenvalues. As N reduces from 2 down to 1, the number of real eigenvalues decreases. Below a critical magnitude $N \leq 1.42207$, only the ground-state energy shows realness in eigenvalues. Finally, as N reaches 1, even the ground-state energy diverges, and there is no real eigenvalue for $N \leq 1$. Above figures have been reproduced from ref. [18].

where N is an arbitrary real number. Apparently, Eq. (2-75) reduces to Bessis's case when $N = 3$ and to simple harmonic oscillator potential while $N = 2$. As shown in Fig. 2.17, for the cases $N \geq 2$, their spectra are discretely distributed and consist of an infinite number of real and positive eigenvalues. A spontaneous PT symmetry breaking emerges at $N = 2$. While

$1 < N < 2$, only finite number of real eigenvalues but infinite pairs of complex conjugates exist. Besides, when $N < 1.42207$, only the ground-state energy keeps the property of positive realness and it diverges as N approaches to 1^+ . For $N \leq 1$, there exists no real eigenvalues.

In addition to the numerical results illustrated in Fig. 2.17 for various N values. Here a proof followed by Bender [19] describes an argument that: if PT symmetry is unbroken for a Hamiltonian, its spectrum must be real. Provided that the Hamiltonian of a system commutes with the combined PT operator, quantum mechanics tells us that the eigenstates $|\psi\rangle$ of a Hamiltonian H and PT operator share the same eigenstates, namely

$$H|\psi\rangle = E|\psi\rangle, \quad PT|\psi\rangle = \lambda|\psi\rangle. \quad (2-76)$$

Next, by left multiply PT operator on the second equation of (2-76), as P and TR commute with each other and $P^2 = T^2 = 1$ (spinless), the relation $|\psi\rangle = \lambda^* \lambda |\psi\rangle$ holds so that the eigenvalue λ can be expressed as a phase factor $\lambda = \exp(i\alpha)$. As stated most of quantum mechanics textbooks, eigenstates are gauge-dependent, that is, one can replace the original eigenstate $|\psi\rangle$ with an arbitrary phase $e^{i\phi} |\psi\rangle$ without loss of generality. By taking the phase $\phi = -\alpha / 2$, the eigenvalue problem of PT operators becomes

$$PT|\psi\rangle = |\psi\rangle. \quad (2-77)$$

Next, we left multiply PT operator on the first equation of (2-77). After simple calculation, one readily shows that $E^* |\psi\rangle = E |\psi\rangle$ and thus the eigenvalue E must be real if preserved under PT operation. Note that the above proof proposed by Bender is not rigorous since T^2 is actually equal to minus one for a half-integer spinful system and it does not explain the emergence of a PT symmetry breaking transition. In 2001, Dorey *et. al.* rigorously showed that the eigen-

spectrum of (2-75) is real and positive within the region $N \geq 2$ [18]. Since the proof is barely relevant to this thesis, we will not discuss it in the later sections.

2-4.3: PT Symmetric System in Optics and Acoustics

In the previous paragraph, a non-Hermitian quantum mechanical system can give rise to real spectra provided that its Hamiltonian is invariant under the simultaneous operation of parity and time-reversal symmetry. Moreover, the change of certain parameters may give rise to PT symmetry phase transition from one real solution to one complex-conjugate pair. Nevertheless, the critical requirement for a precisely balanced potential energy $V(\mathbf{r}) = V^*(-\mathbf{r})$ makes experimental realisation nearly impossible in a quantum mechanical system. Interestingly, there is an alternative way that the optical waveguide with the paraxial approximation gives a formally equivalent expression of 1D Schrödinger equation. Hence, a few years after the first PT paper, Guo et. al. [38] proposed an optical realisation governed by the equivalent time-dependent Schrödinger equation yielding

$$-i\partial_z E = (2n_0 k_0) \partial_x^2 E + k_0 n(x) E, \quad (2-78)$$

where k_0 denotes the vacuum wavenumber and $n(x)$ is the perturbation from the ambient refractive index n_0 . Also, the propagation along z direction can be regarded as a temporal evolution of the wavefunctions and the term $k_0 n(x)$ mimics the potential energy in quantum mechanics. Under the condition given by (2-74), one has $n(x) = n^*(-x)$ to assure the invariant of PT symmetry. To satisfy the condition, two single-mode waveguides made of gain and loss dielectrics with $n_{\pm} = n_r \pm i n_i$ can be placed adjacently for having coupled modes. To further

simplify Eq. (2-78), generally the solution for each waveguide has the form $E(x, y, z) = Af(x, y)\exp(i\beta z)$, and then a set of coupled-mode equations can be written as

$$-i\partial_z \begin{bmatrix} A_1 \\ A_2 \end{bmatrix} = \begin{bmatrix} \beta_1 & \kappa \\ \kappa^* & \beta_2 \end{bmatrix} \begin{bmatrix} A_1 \\ A_2 \end{bmatrix}, \quad (2-79)$$

where κ is the coupling coefficient whose value is determined by the overlap integral of the optical fields E_1 and E_2 based on the distance between waveguides. The eigenvalues of Eq. (2-79) are given by

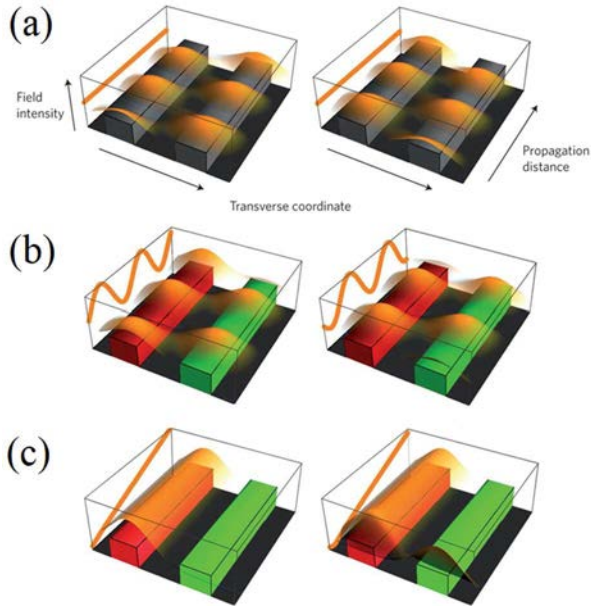


Fig. 2.18: Schematic figure of coupled gain-loss waveguides.

(a) Optical field through coupled waveguide pair, with incident source wave at one end of left waveguide for the left strip and right guide in right strip. (b) Lossless waveguides combined gain and loss waveguide. A PT waveguide, with gain(loss) marked in red(green), shows wave propagation with the similar feature as (a) but varying intensity. Under this circumstance, coupling strength dominates the PT symmetric system i.e. $\kappa > \text{Im}(\beta_1)$. (c) PT waveguides with broken PT symmetry. Waves propagate only in gain channel regardless of energy injected from which waveguides. The orange curves represent the total optical power. It implies the magnitude of gain/loss is stronger than coupling strength ($\kappa < \text{Im}(\beta_1)$). Above figures have been reproduced from ref. [39].

$$k_z = -\left(\frac{\beta_1 + \beta_2}{2}\right) \pm \sqrt{|\kappa|^2 + \left(\frac{\beta_1 - \beta_2}{2}\right)^2}. \quad (2-80)$$

The above equation shows that if $\beta_2 = \beta_1^*$, spontaneous PT symmetry breaking takes place as κ or $\text{Im}(\beta_1)$ changes. When $\kappa > \text{Im}(\beta_1)$, which implies the coupling strength dominates the gain parameters, k_z is real so that the propagating mode arises in both waveguide channels without dissipation. Interestingly, as shown in Fig. 2.18b while the eigenmodes evolve, if a

source is placed at one port, the total strength of electric fields “bounces” between two channels as a function of z because the non-Hermitian Hamiltonian leads to the consequence of non-orthonormality of the associated fields given by $(A_1, A_2) = (1, \pm \exp(\pm i \sin^{-1}(\text{Im}(\beta_1) / \kappa)))$. As $\text{Im}(\beta_1) / \kappa < 1$, the field pattern is changed. Since k_z is now a complex value and the corresponding eigen-fields are $(A_1, A_2) = (1, \pm i \exp(\mp \cosh^{-1}(\text{Im}(\beta_1) / \kappa)))$, the gained waveguide $\text{Im}(\beta_1) < 0$ dominates the propagation. That is to say, in this PT symmetry breaking phase, in the course of the field evolution the wave is independently amplified in gained channel but attenuated in dissipated one. Last, when the ratio $\text{Im}(\beta_1) / \kappa$ is unitary, a transition which connects two real solutions and a complex conjugate pair, occurs as shown in Fig. 2.18c. One can find a detailed discussion regarding this transition in the next section.

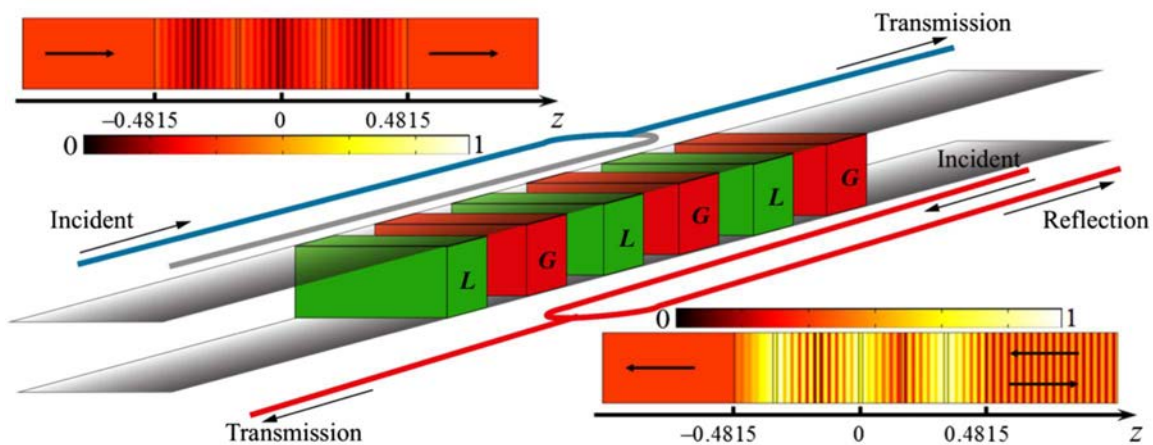


Fig. 2.19: Schematic picture of the acoustic PT channel. The entire system is made of three gain regions (red), three loss regions (green), and five passive regions in between. The incident acoustic wave is ejected from left and the transmission and reflection are illustrated. This PT-symmetric system is especially designed for reflection-less acoustic wave propagation from left. The insets show two normalised amplitude of the pressure field pumping from the left (up-left inset) and right (down-right inset) at the exceptional point. Above figures have been reproduced from ref. [40]

On the other hand, after the remarkable success of PT symmetric optics, the search of other physical counterparts is intuitively anticipated. Pressure acoustics, which possesses similarity corresponding to 2D electromagnetic waves, becomes the first candidate that may

achieve PT symmetric physics. The governed equation for pressure acoustics in homogenous media is given by

$$\frac{1}{\rho} \frac{d^2 P}{dz^2} + \frac{\omega^2}{B} P = 0, \quad (2-81)$$

where P denotes the pressure, ρ is the mass density, and B is the bulk modulus. To obtain the conservation of PT symmetry, the gain/loss media are both required. With regard to a dissipated material, the bulk modulus has a negative imaginary part as one defines the time convention $\exp(-i\omega t)$. However, the lack of acoustic gain media in nature makes the realisation of PT symmetric acoustics experimentally challenging. In 2014, X. Zhu et. al. proposed a possible realisation by means of feedback systems using the active sound-controlling equipment [40]. As shown in Fig. 2.19, the PT acoustic system contains six blocks made of staggered gain and loss portions, thus there are five passive regions between them. Considering the region outside the PT setup, the sound wave can be decomposed into left and right propagating solutions: $P_f^{R(L)} e^{-ikz} + P_b^{L(R)} e^{ikz}$, where the sign $L(R)$ stands for the waves at the left (right) outside of PT area, k is the wavevector, and $P_{f(b)}$ is the amplitude of forward(back-forward) propagating mode. Thus, one can define the scattering matrix of the entire PT setup which yields [40]

$$\begin{bmatrix} P_f^R \\ P_b^L \end{bmatrix} = \begin{bmatrix} t & r_R \\ r_L & t \end{bmatrix} \begin{bmatrix} P_f^L \\ P_b^R \end{bmatrix} = S(k) \begin{bmatrix} P_f^L \\ P_b^R \end{bmatrix}, \quad (2-82)$$

where $r_{L(R)}$ and t respectively represents the (left)right reflection and transmission coefficient.

As mentioned in 2-4.1, applying PT operation on the system, Eq. (2-82) becomes

$$\begin{bmatrix} P_f^{L*} & P_b^{R*} \end{bmatrix}^T = S(k) \begin{bmatrix} P_f^{R*} & P_b^{L*} \end{bmatrix}^T$$

and then we have a condition for PT symmetric acoustic scattering matrix written by

$$S^{-1}(k) = S^*(k), \quad (2-83)$$

or an equivalent condition is

$$r_L r_R^* = 1 - |t|^2, \quad \sqrt{R_L R_R} = |1 - T|, \quad (2-84)$$

with $R_{L(R)} = |r_{L(R)}|^2$ and $T = |t|^2$. With the condition of Eq. (2-83) and (2-84), the construction of scattering can be done based on transfer matrix method. Based on Eq. (2-84), since transmittance T is a real number, the product of two reflections $r_L r_R^* = e^{i(\phi_L - \phi_R)} \sqrt{R_L R_R}$ must be a real number either, which implies the phase difference $\phi_L - \phi_R$ must equal 0 or π . Therefore, the connection between left and right phase is expressed as

$$\phi_L = \phi_R, \text{ if } T > 1$$

$$\phi_L = \phi_R + \pi, \text{ if } T < 1$$

which infers a transition at $T = 1$. Another intriguing phenomenon arising from PT symmetric physics is one-way transport. Note that the unidirectional propagation mentioned here has different mechanisms in comparison with topological cases, which exist at boundaries and does not need any gain/loss medium. As depicted in Fig. 2.20a-b, the phase and the amplitude of reflected and transmitted waves travelling through PT area are calculated, respectively. In Fig. 2.20a, as indicated before, the left reflection has a π phase jump at the frequency around 6k Hz, and both have a $\pm\pi/2$ phase difference with the transmission. This phase discontinuity makes the delay time $\tau = d\phi/d\omega$ go to infinite so that, to be physical, the related amplitude must approach to zero at that frequency point as shown in Fig. 2.20b. In the view of phase transition, the left reflection singular point, which is a transition point between PT unbroken and broken

phase, is named as the exceptional point. Note that exceptional points differ from degeneracy points even though degenerate modes occur in both cases. Generally, excluding the case of accidental degeneracies, degeneracies in real frequency diagrams are stabilised by certain symmetries in parametric space, such as Dirac points we mentioned. Yet, in the case of exceptional points, there exist no degeneracies if one only takes real spectrum into account. Even though we broaden the concept to complex frequency, at exceptional points they are defective modes, making the phase rigidity approach to zero [41]. The formalism of phase rigidity will be discussed in the Sec. 2-4.4.

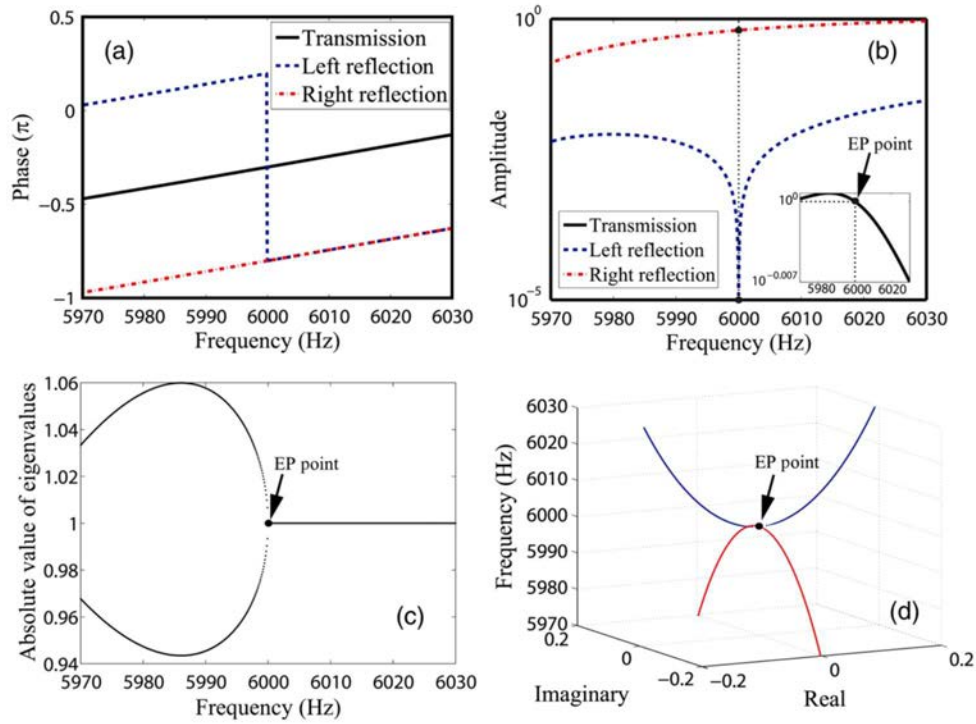


Fig. 2.20: Spectra and EPs in PT acoustics. Phases (a) and amplitude (b) of left-reflected, right-reflected, and transmitted waves of the proposed acoustic PT-symmetric system. At critical frequency 6k Hz, the existence of a EP is shown with the absolute value of eigenvalues in (c) and complex plane in (d), respectively. Above figures have been reproduced from ref. [40]

To give a clear explanation, by solving eigenvalue problem of scattering matrix, the absolute values of eigenvalues illustrated in Fig. 2.20c-d evidently show the emergence of exceptional points located at the singular frequency. Besides, while T is equal to one, Eq. (2-84) indicates that one of the reflections should vanish, which also matches the reflected

singularity. Consequently, the frequency possessing transmission $T = 1$ is the PT symmetry transition for an acoustic system. In the next section, a further discussion of exceptional points will be given.

2-4.4: Exceptional Points and Rings

So far, we have stated that the exceptional point is a transition point connecting broken and unbroken PT symmetric phases. In fact, it is possible to find exceptional points in any non-Hermitian Hamiltonian with an imaginary part difference. Furthermore, in the field of photonic crystals, B. Zhen. *et. al.* [42] broadened this perspective which can spawn a ring of exceptional points out of a Dirac degeneracy at Γ point. In the following content, a brief introduction for non-PT symmetric exceptional points and the exceptional ring will be shown.

To study exceptional points in a non-PT symmetric system, we start with considering a two-by-two Hamiltonian written by

$$H = \begin{bmatrix} a - ib & d \\ d & a - ic \end{bmatrix}, \quad (2-85)$$

where all the parameters are real and Hamiltonian is a PT symmetric type as $c = -b$ implying the use of gain and loss material. After simple derivation, Eq. (2-85) can be split into two terms $H_0 + H'$, in which $H_0 = (i/2) \text{diag}(b+c, b+c)$ and

$$H' = \begin{bmatrix} a + i(b-c)/2 & d \\ d & a - i(b-c)/2 \end{bmatrix}. \quad (2-86)$$

Eq. (2-86) is exactly a PT-symmetric Hamiltonian. As a result, unbalanced imaginary parts of diagonal terms make the research of exceptional points possible even in non-PT symmetric systems. Since the implement of balanced gain/loss materials is challenging in experiments, the extending concept of the imaginary part difference provides more possibilities in the study

of exceptional points. Amongst all the intriguing phenomena, the high-order exceptional point has attracted considerable attention because it can only be generated by the coalescence of two lower-order exceptional EPs. As an example, in the next section we will have an overview of the work proposed by K. Ding *et. al.* [43] who experimentally realised the high-order exceptional points in multiple coupled acoustic cavities.

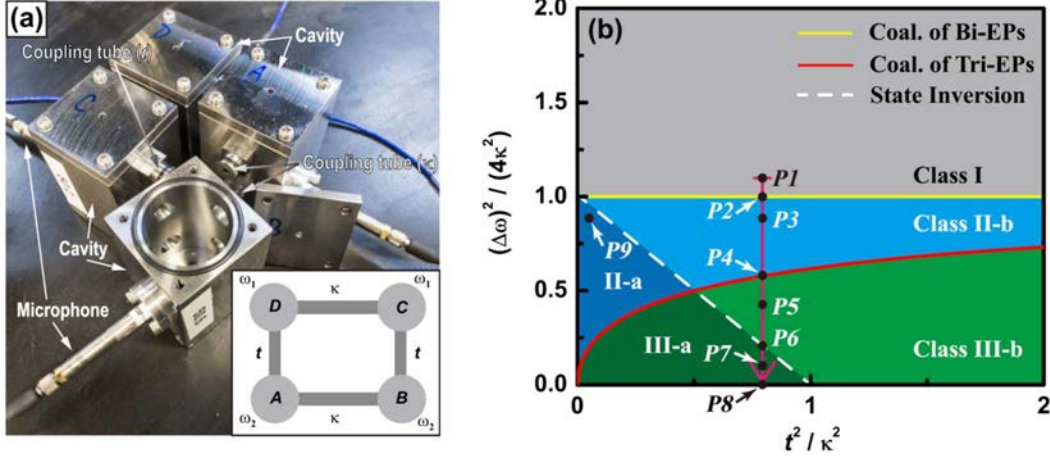


Fig. 2.21: Experimental setup and phase diagram of high-order EPs. (a) A photograph of four coupled acoustic cavity resonators. In inset, a schematic plot of the system. (b) Phase diagram in terms of $\Delta\omega$ and t . The grey, blue, and green regions stand for classes I, II, and III EP formation patterns, respectively. The region of varying classes is separated into three by solid red and yellow lines. The red line labels the coalescence of three EPs and the solid yellow one labels the coalescence of two EPs. The white dashed line, which divide subclasses “a” and “b” into distinct topological nature, indicates the state inversion. Above figures have been reproduced from ref. [43]

As shown in Fig. 2.21a, a lossy four-state system consists of four coupled acoustic cavities is implemented. In such system, there are three classes of EPs that are governed by the Hamiltonian [43]

$$H = \begin{bmatrix} \omega_2 - i\Gamma_1 & \kappa & 0 & t \\ \kappa & \omega_2 - i\Gamma_2 & t & 0 \\ 0 & t & \omega_1 - i\Gamma_1 & \kappa \\ t & 0 & \kappa & \omega_1 - i\Gamma_2 \end{bmatrix}, \quad (2-87)$$

where, Γ and t respectively represents the intrapair and the interpair coupling strength and the loss difference is introduced by adding extra absorption in cavity B and D . The corresponding eigenfrequencies is expressed by

$$\omega_j = \omega_0 - i\Gamma_0 \pm \frac{1}{2}\sqrt{\Delta_1 \pm 4\Delta_2}, \quad (2-88)$$

where $j = 1, 2, 3, 4$, $\omega_0 = (\omega_1 + \omega_2)/2$, $\Gamma_0 = (\Gamma_1 + \Gamma_2)/2$, and

$$\Delta_1 = \Delta\omega^2 - \Delta\Gamma^2 + 4\kappa^2 + 4t^2, \quad (2-89)$$

$$\Delta_2 = 4\kappa^2 t^2 + \kappa^2 \Delta\omega^2 - \Delta\Gamma^2 \Delta\omega^2 / 4, \quad (2-90)$$

with $\Delta\omega = \omega_1 - \omega_2$ and $\Delta\Gamma = \Gamma_1 - \Gamma_2$. Four states are arranged in the following sequence: $j = 1 : (-, +)$, $j = 2 : (-, -)$, $j = 3 : (+, -)$, and $j = 4 : (+, +)$, where the first (second) sign indicates the choice of the sign in Eq. (2-88). With Eq. (2-88) to (2-90), one can further classify the type and the order of EPs via observing the amount of merging EPs. As illustrated in Fig. 2.21b, for class I, two EPs are fairly separated, which means the EPs independently caused from each pair of coupled cavities. By decreasing the value $\Delta\omega/2\kappa$, the system transfers to class II when $\Delta\omega/2\kappa$ reaches one. The line plot in Fig. 2.21b shows that the upper and the lower eigenfrequency branches merge and split into two EPs. If one manipulates the parameter backward (i.e. increase from $\Delta\omega/2\kappa < 1$), two EPs coalesce to a high-order one at the special point $\Delta\omega/2\kappa = 1$. Keeping decreasing $\Delta\omega/2\kappa$ to 0.758, the system meets the third class such that three EPs merge into a higher-order one. We will discuss the order of high-order EPs in the next paragraph.

Mathematically, the order of an EP represents the ratio of the number of Riemann surfaces crossing and how many circles the EP makes the state back to its origin. For example, if the order is 1/2, the state evolves two circles back to its starting point on a one-crossing Riemann surface pair. To determine the order of a specific EP, one way is to evaluate the phase rigidity of two states because its value vanishes where the EPs stand. The phase rigidity is defined as

$$r_j = \langle \tilde{\phi}_j^R | \tilde{\phi}_j^R \rangle^{-1}, \quad (2-91)$$

where $|\tilde{\phi}_j^R\rangle$ denotes normalised eigenvector of a non-Hermitian Hamiltonian, which yields

$$|\tilde{\phi}_j^R\rangle = \frac{|\phi_j^R\rangle}{\sqrt{\langle \phi_j^L | \phi_j^R \rangle}}, \quad (2-92)$$

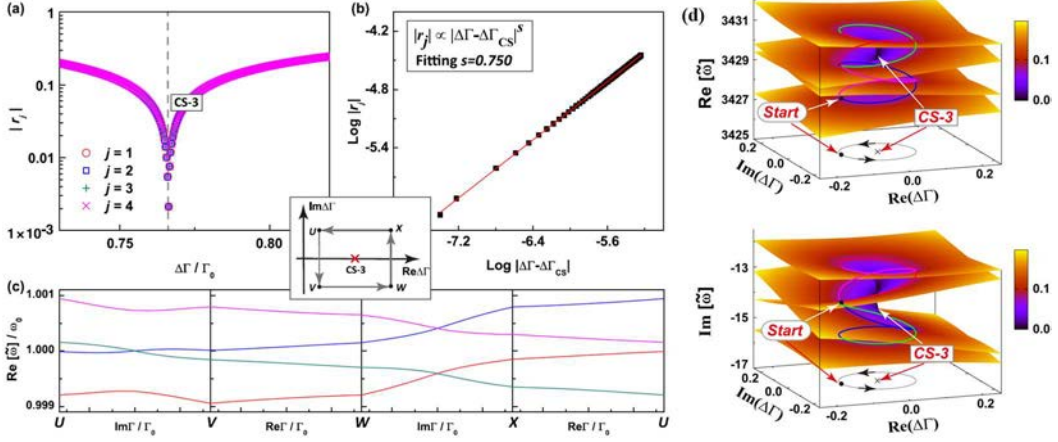


Fig. 2.22: Phase rigidity and Riemann surface. (a) Phase rigidity of the eigenstates as functions of loss. At certain point $\Delta\Gamma = \Gamma_0$ three eigenstates coalesce to a high-order EP. (b) Log-log plot of phase rigidity with respect to $|\Delta\Gamma - \Delta\Gamma_{CS}|$ for the EP shown in (a), and the calculated result fairly fits the solid line with a 3/4 slope. The inset gives a closed loop on the complex- $\Delta\Gamma$ plane, where the EP is enclosed by the loop. (c) Eigenstate trajectories for the loop with direction (U \rightarrow V \rightarrow W \rightarrow X \rightarrow U) in the inset. Four cycles are made with three intersections, resulting in a power law with the order 3/4. (d) The 3D figure of the real and imaginary part of frequency versus complex- $\Delta\Gamma$ plane. At EP four Riemann sheets crossing creates a high-order EP. Above figures have been reproduced from ref. [43]

with $|\phi_j^{R(L)}\rangle$ calculated by right(left) eigenvalue problems. Fig. 2.22 shows the plot of phase rigidity for one high-order EP as discussed in the previous paragraph. As depicted in Fig. 2.22a-b, three EP states merge together and the related phase rigidity is proportional to the power law $|\Delta\Gamma - \Delta\Gamma_{CS}|^{3/4}$; in Fig. 2.22c, around the EP, a state evolves four cycles to return its initial states, and during the evolution, a three-time intersection implies $s = 3/4$. To give a more visualising demonstration, Fig. 2.22d illustrates two 3D plots that four intersect Riemann sheets make the evolution take four circles to its origin, and three crossing lines arise from these sheets around the EP. Consequently, through observing Riemann surfaces, one can visually define the order of EPs.

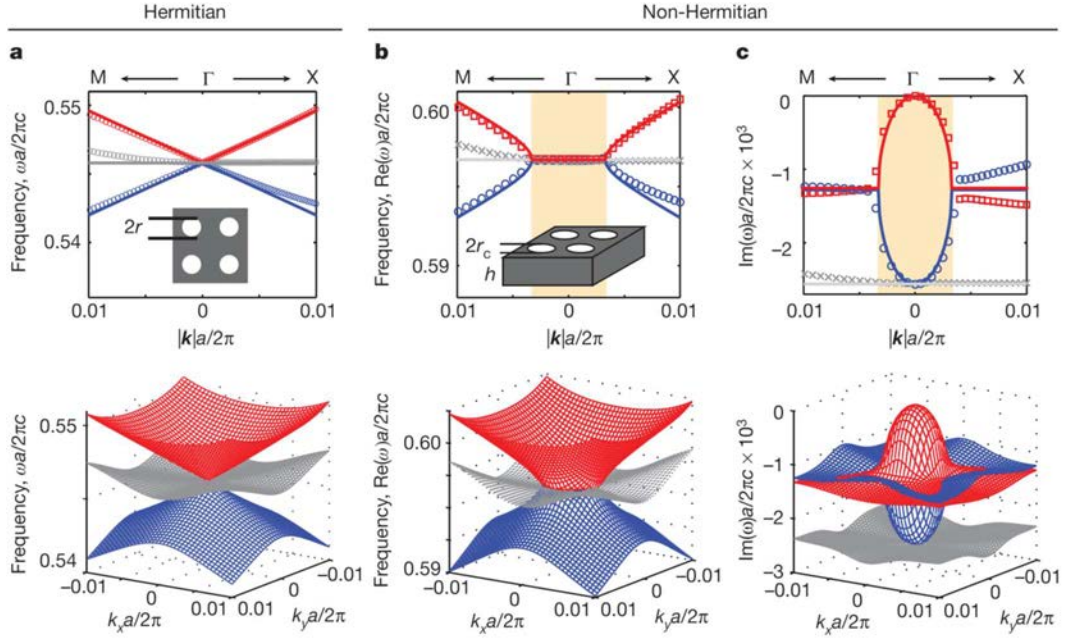


Fig. 2.23: A ring of EPs. (a) Band structure of a 2D photonic crystal composed of drilling air holes in a dielectric matrix. An accidental Dirac degeneracy arises from adjusting geometry parameter between a quadrupole band and two dipole bands. The bottom panel depicts a linear cone as expected as a Dirac degeneracy. (b) The real parts of the eigenvalues of an open-boundary photonic slab. A ring of exceptional points deformed from the Dirac degeneracy is shown in the yellow shaded region. 3D band structure further verifies the appearance of the exceptional ring. (c) The imaginary parts of the eigenvalues in association with real part plot, which has an ellipsoid closed surface in 3D dispersion plot. Throughout this figure, the parameters are given as follows: $a = 336$ nm, $r = 109$ nm, and refractive index $n = 2.02$ for Si_3N_4 . Above figures have been reproduced from ref. [42]

Aside from high-order exceptional points, generating exceptional rings out of a Dirac degeneracy at Γ was proposed [44]. The mode of Dirac cone at Γ point is made of one quadrupole and two dipole states. With an open boundary, classical electromagnetism has shown that only dipole moments will radiate the energy to the background instead of other multi-pole modes. As a result, by means of the radiation loss, an exceptional ring arises from the imaginary part difference [42]. Fig. 2.23a illustrates the band structure in a photonic crystal consisting of air holes and a dielectric background with a square lattice. Around Brillouin zone centre, an accidental Dirac degeneracy can be achieved via tuning geometry parameters. By numerical calculation, Fig. 2.23b-c respectively shows the real and imaginary parts of eigenvalues based on the structure of photonic crystal slab. The real part of band diagram clearly depicts a ring of exceptional points at frequency equals 0.597; the imaginary part forms

a closed ellipse shape associated with the area of the exceptional ring.

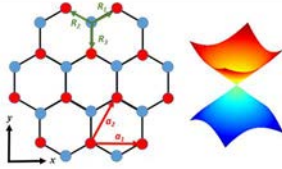

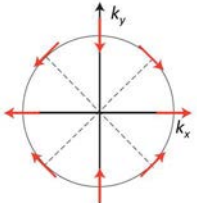
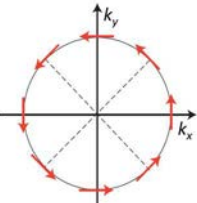
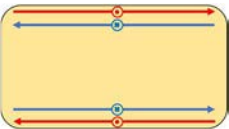
2-5: Chapter Summary

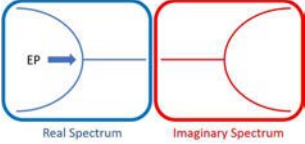
Throughout chapter two, firstly we have introduced the key concepts of topological physics and the up-to-date progress in graphene and topological insulators. In this review, some crucial mathematical tools are outlined to pave the way for subsequent discussions. Starting with a single-particle Schrödinger equation, the physical expressions of Berry mechanism were deduced. After briefly introducing the development of graphene in the absence of SOC, Rashba and Dresselhaus SOC terms are reviewed. Next, based on graphene's honeycomb structure, an essential physical system called Haldane model was discussed, which shows the properties of reflection-immune one-way edge states in the absence of net magnetic fields. Afterwards, a revolutionary concept proposed by Kane and Mele extends the idea from the symmetry-breaking to the symmetry-protected edge excitations. Since the Chern number description is not valid for symmetry-protected systems, a new topological index so-called Z_2 was investigated. Subsequently, topological insulators in 3D were discussed.

Secondly, the real eigenvalues and the emergence of spontaneous symmetry breaking were analysed in a PT symmetric system. For non-Hermitian but PT symmetric Hamiltonian, the realness of eigenvalues has been proved theoretically and verified experimentally in an equivalent optical system. In addition to the realisation in optics, PT symmetric phenomena have also been theoretically analysed and experimentally achieved in an acoustic setup made of channels filled with gain/loss inclusions. Furthermore, if we lose the restriction of balanced gain-loss magnitudes, passive PT symmetric systems, which only need the difference of imaginary terms, have attracted great interest owing to the feasibility in lower scale fabrication. In sec. 2-4.4, taking four coupled acoustic cavities as an example, the high-order exceptional

point resulted from the coalesces of a few low-order exceptional points were investigated. Also in photonic crystals, the emergence of the radiation loss in an open-boundary system spawns an exceptional ring out of a Dirac cone at Brillouin centre. With this exceptional ring, one can obtain the effects caused by single exceptional point along every direction.

As below, Table II summarises certain results related to contents in following chapters, including the conditions to achieve and the key features/outcomes in the aforementioned physical systems. In the beginning of every subsequent chapter, we will point out which system is about to be discussed to help readers catch up with the major concepts.

	Topic	Key feature	Condition
A	Graphene and Dirac point	 <p>Graphene's geometry and the zoomed-in figure of a Dirac point.</p>	<ol style="list-style-type: none"> 1. Preserve P symmetry 2. Preserve TR symmetry 3. Preserve C_3 symmetry
B	Chern insulators	 <p>Topological edge states (spinless)</p>	<ol style="list-style-type: none"> 1. Break TR symmetry 2. Non-zero Chern number
C	Dresselhaus SOC	 <p>Spin texture projection on xy plane</p>	Break central symmetry
	Rashba SOC	 <p>Spin texture projection on xy plane</p>	Break spatial symmetry
D	Kane-Mele Model (topological insulator)	 <p>Topological edge states (spinful)</p>	<ol style="list-style-type: none"> 1. Preserve TR symmetry 2. Non-zero Z_2 invariant

E	PT symmetric System	 <p data-bbox="598 360 965 421">Exceptional points as a transition b/w real and complex eigenvalues</p>	The coupling between equal gain and loss channels.
<p>Table II: Summary of the main results and their conditions in this chapter. Part A provides the conditions of creating Dirac degeneracies. Part B demonstrates topological edge states in Chern insulators, such as Haldane model. Part C indicates two kinds of SOC via breaking different symmetries. Part D gives a schematic diagram of topological insulators, i.e. KM model. The red(cyan) arrows denote spin-up(down) currents propagating along boundaries. Part E shows a PT symmetric system and the emergence of exceptional points.</p>			

Chapter 3 Novel Phenomena in Normal Spring-Mass Systems

Note: The contents of this chapter have been published in the following papers and some of the text form from these papers are used in this chapter:

I. *New Journal of Physics*, 17, 073031 (2015) [14]

II. *New Journal of Physics*, 18, 113014 (2016) [45]

In chapter two we have simply outlined the topological characteristics and spin-orbit interaction in graphene. In this chapter, two interesting results observed in quantum mechanical regime are presented in a classical spring-mass system. Firstly, although the topological phenomenon was firstly studied in the electronic systems, we demonstrate a mechanical version of quantum Hall effect via the verification of Chern numbers and topological edge states, which is unprecedented in classically vibrating systems [14]. Next, through pre-stretching springs, we present the effective SOC despite of the fact that SOC is a relativistic effect in quantum mechanics. In addition, in the presence of effective SOC, the mechanical counterpart of SHE arises in mechanical systems [45]. In what follows, the contents in Sec. 3-1, 3-2, and 3-3 are related to Part A, B, and C in Table II, respectively. We will discuss these novel results in detail.

3-1: Mechanical Graphene

In this section, a possible model for the realisation of mechanical edge states is given. The geometry of the model made by a series of honeycomb-arranged particles with mass M and springs with elastic constant K is shown in Fig. 3.1a. Every mass bead is considered as a rigid

body, and the mass of springs is omitted. By defining a to be the distance between a pair of particles (A and B), the lattice constant is thus $|\mathbf{a}_1| = |\mathbf{a}_2| = \sqrt{3}a$, where the bases are $\mathbf{a}_1 = \sqrt{3}a \hat{\mathbf{x}}$ and $\mathbf{a}_2 = (\sqrt{3}\hat{\mathbf{x}} + 3\hat{\mathbf{y}})a/2$. The centre of the mn unit cell is located at $\mathbf{r}_{mn} = m\mathbf{a}_1 + n\mathbf{a}_2$. The basics of the reciprocal lattices are $\mathbf{b}_1 = 2\pi(\sqrt{3}\hat{\mathbf{x}} - \hat{\mathbf{y}})/3a$, $\mathbf{b}_2 = 4\pi\hat{\mathbf{y}}/3a$. Three vectors connecting the particle A to its nearest neighbours are

$$\begin{aligned}\hat{\mathbf{R}}_1 &= \frac{1}{3a}(\mathbf{a}_1 + \mathbf{a}_2) = \frac{\sqrt{3}}{2}\hat{\mathbf{x}} + \frac{1}{2}\hat{\mathbf{y}} \\ \hat{\mathbf{R}}_2 &= \frac{1}{3a}(-2\mathbf{a}_1 + \mathbf{a}_2) = -\frac{\sqrt{3}}{2}\hat{\mathbf{x}} + \frac{1}{2}\hat{\mathbf{y}} \\ \hat{\mathbf{R}}_3 &= \frac{1}{3a}(\mathbf{a}_1 - 2\mathbf{a}_2) = -\hat{\mathbf{y}}\end{aligned}$$

We denote the small displacements, which implies quadratic or higher terms can be neglected, around the A and B as $\boldsymbol{\xi}$ and $\boldsymbol{\eta}$, the dynamical distance between them as $\mathbf{R}' = \mathbf{R} + \mathbf{u}$, and then $|\mathbf{R}'| = \sqrt{|\mathbf{R}|^2 + 2\mathbf{R} \cdot \mathbf{u} + |\mathbf{u}|^2} \approx |\mathbf{R}| + \hat{\mathbf{R}} \cdot \mathbf{u}$. The variation of the spring length is

$$\Delta_R = \hat{\mathbf{R}} \cdot \mathbf{u}, \quad (3-1)$$

and hence the Lagrangian of the system is denoted as

$$\begin{aligned}L &= \sum_{m,n} \frac{M}{2} (\dot{\boldsymbol{\xi}}_{mn}^2 + \dot{\boldsymbol{\eta}}_{mn}^2) \\ &\quad - \sum_{m,n} \frac{K}{2} \left\{ \left[\hat{\mathbf{R}}_1 \cdot (\boldsymbol{\xi}_{mn} - \boldsymbol{\eta}_{mn}) \right]^2 + \left[\hat{\mathbf{R}}_2 \cdot (\boldsymbol{\xi}_{mn} - \boldsymbol{\eta}_{m-1,n}) \right]^2 + \left[\hat{\mathbf{R}}_3 \cdot (\boldsymbol{\xi}_{mn} - \boldsymbol{\eta}_{m,n-1}) \right]^2 \right\}\end{aligned}$$

Substituting above Lagrangian into Euler-Lagrange equation, a set of equations of motion is given by

$$M\ddot{\boldsymbol{\xi}}_{mn} = -K \left[\hat{\mathbf{R}}_1 \hat{\mathbf{R}}_1 \cdot (\boldsymbol{\xi}_{mn} - \boldsymbol{\eta}_{mn}) + \hat{\mathbf{R}}_2 \hat{\mathbf{R}}_2 \cdot (\boldsymbol{\xi}_{mn} - \boldsymbol{\eta}_{m-1,n}) + \hat{\mathbf{R}}_3 \hat{\mathbf{R}}_3 \cdot (\boldsymbol{\xi}_{mn} - \boldsymbol{\eta}_{m,n-1}) \right], \quad (3-2)$$

$$M\ddot{\boldsymbol{\eta}}_{mn} = -K \left[\hat{\mathbf{R}}_1 \hat{\mathbf{R}}_1 \cdot (\boldsymbol{\eta}_{mn} - \boldsymbol{\xi}_{mn}) + \hat{\mathbf{R}}_2 \hat{\mathbf{R}}_2 \cdot (\boldsymbol{\eta}_{mn} - \boldsymbol{\xi}_{m+1,n}) + \hat{\mathbf{R}}_3 \hat{\mathbf{R}}_3 \cdot (\boldsymbol{\eta}_{mn} - \boldsymbol{\xi}_{m,n+1}) \right]. \quad (3-3)$$

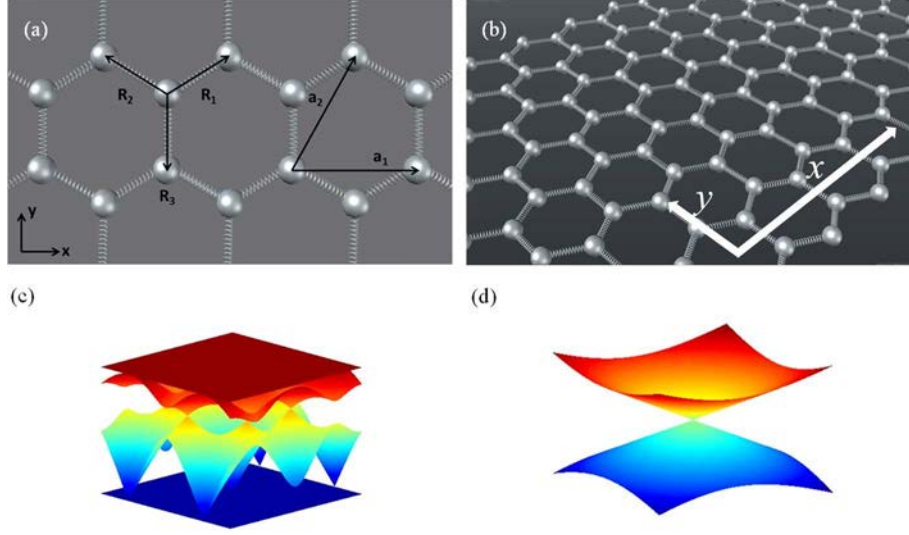


Fig. 3.1: Mechanical graphene.(a) Top view of zoomed-in plot and (b) mechanical graphene strip made of soft springs and rigid particles. a_i and R_i denotes lattice constants and nearest vectors, respectively. (c) The 3D band structure of mechanical graphene, where the mass and elastic constant equals to 10g and 4N/m, respectively. Two flat bands on top and bottom are clearly seen. (d) a zoomed-in figure of Dirac cone in the vicinity of a certain K point.

So far, we have obtained the equations of motion for particles arranged as honeycomb lattice.

To solve for the propagating normal-mode, one can assume

$\xi_{mn} = \xi p^m s^n e^{-i\omega t}$, $\eta_{mn} = \eta p^m s^n e^{-i\omega t}$, where $p = e^{ik \cdot a_1}$, $s = e^{ik \cdot a_2}$. Substituting above equations

into Eq. (3-2) and (3-3), we have an eigenvalue problem $\mathbf{H}\mathbf{x} = \omega^2 \mathbf{x}$, in which

$$\mathbf{H} = \omega_0^2 \begin{bmatrix} 3/2 & 0 & -\frac{3}{4}(1+p^*) & -\frac{\sqrt{3}}{4}(1-p^*) \\ 0 & 3/2 & -\frac{\sqrt{3}}{4}(1-p^*) & -\frac{1}{4}(1+p^*+4s^*) \\ -\frac{3}{4}(1+p) & -\frac{\sqrt{3}}{4}(1-p) & 3/2 & 0 \\ -\frac{\sqrt{3}}{4}(1-p) & -\frac{1}{4}(1+p+4s) & 0 & 3/2 \end{bmatrix}, \quad (3-4)$$

where $\omega_0^2 = K/M$ is the characteristic frequency of the system. By solving eigenvalue problem

given by Hamiltonian (3-4), one can obtain four solutions, two of them are 0 and $\sqrt{3}\omega_0$, others

give dispersion relation

$$\omega = \omega_0 \sqrt{\frac{3}{2} \mp \frac{1}{2} \sqrt{3 + 2 \left\{ \cos(\mathbf{k} \cdot \mathbf{a}_1) + \cos(\mathbf{k} \cdot \mathbf{a}_2) + \cos[\mathbf{k} \cdot (\mathbf{a}_1 - \mathbf{a}_2)] \right\}}} . \quad (3-5)$$

The band structure plotted by Eq. (3-4) is shown in Fig. 3.1c. There are four bands in Fig. 3.1c. In addition to the zero-frequency plane, the top one is also the flat bulk state. It implies that all particles vibrate locally at the frequency $\sqrt{3}\omega_0$. Besides, six linear degeneracies are seen in the vicinity of K points around the whole Brillouin zone. Expanding Eq. (3-5) to second order at one K point $(4\pi/3\sqrt{3}a, 0)$, it shows that $\omega = \omega_0(1 \pm |\delta\mathbf{k}|a/4)$ is a linear function with respect to \mathbf{k} vector. Fig. 3.1d indicates the zoomed-in plot near K point. These degeneracies, which referred as Dirac points, provide the chance to have topological edge states known in quantum Hall states and topological insulator. In the following contents, topological nature of edge states will be discussed.

Prior to going further for phononic edge states, an approach of analysing band structure needs to be further discussed. In Fig. 3.1b, our system, which likes a long ribbon, has an infinite length along x direction, but a finite width constructed out of N unit cells in y direction. Thus, as this semi-infinite geometry gives periodicity only in the x axis, we employ Fourier expansion of displacement ξ and η as well as time convention $\exp(-i\omega t)$, and then the dispersion equation is expressed as

$$\omega^2 \xi = \omega_0^2 \left[\hat{\mathbf{R}}_1 \hat{\mathbf{R}}_1 \cdot (\xi - \eta) + \hat{\mathbf{R}}_2 \hat{\mathbf{R}}_2 \cdot (\xi - e^{-ik \cdot \mathbf{a}_1} \eta) + \hat{\mathbf{R}}_3 \hat{\mathbf{R}}_3 \cdot (\xi - \eta_{n-1}) \right], \quad (3-6)$$

$$\omega^2 \eta = \omega_0^2 \left[\hat{\mathbf{R}}_1 \hat{\mathbf{R}}_1 \cdot (\eta - \xi) + \hat{\mathbf{R}}_2 \hat{\mathbf{R}}_2 \cdot (\eta - e^{ik \cdot \mathbf{a}_1} \xi) + \hat{\mathbf{R}}_3 \hat{\mathbf{R}}_3 \cdot (\eta - \xi_{n+1}) \right]. \quad (3-7)$$

where $\xi(k, n)$ and $\eta(k, n)$ have been expressed as ξ and η for briefness. Moreover, above equations can be rewritten as an eigenvalue problem $\mathbf{H}_B \mathbf{x} = \omega^2 \mathbf{x}$ as well, where $\mathbf{x} = [\xi_x^{(1)}, \xi_y^{(1)}, \eta_x^{(1)}, \eta_y^{(1)}, \dots]^T_{1 \times 4N}$, is the eigenvector of displacements at A and B, and Hamiltonian

$$\mathbf{H}_B = \omega_0^2 \begin{bmatrix} 3/2 & 0 & (-1-p^*)/4 & \sqrt{3}p^*/4 & & & \\ 0 & 3/2 & \sqrt{3}p^*/4 & -3p^*/4 & 0 & & \\ (-1-p)/4 & \sqrt{3}p/4 & 3/2 & 0 & -1/4 & -\sqrt{3}/4 & \\ \sqrt{3}p/4 & -3p/4 & 0 & 3/2 & -\sqrt{3}/4 & -3/4 & \\ & 0 & -1/4 & -\sqrt{3}/4 & 3/2 & 0 & \\ & & -\sqrt{3}/4 & -3/4 & 0 & \ddots & \end{bmatrix}_{4N \times 4N} \quad (3-8)$$

The 1D projected band structure of a spring-mass mechanical graphene ribbon is shown in Fig. 3.2. Firstly, as the same as graphene with zigzag truncation, the similar flat edge state between two Dirac points is observed in the energy spectrum. Due to the existence of the flat band, at the corresponding frequency the particles located on the edge vibrate locally and propagate no energy forward. Apart from zigzag edge case, band diagram calculated from bearded truncation shown in Fig. 3.2b also gives a flat band throughout the whole \mathbf{k} space. It is worth noting that these edge states differ from conventional bearded flat edge ones in real graphene, which only exhibits in the region between K points. In addition, for both cases there are two edge states that can be found between either 1st and 2nd band or 3rd and 4th band in Fig. 3.2a-b. These states derived from Hamiltonian with both types of boundary were recently proposed and observed by Y. Plotnik *et. al.* in the case referred ‘photonic graphene’, and the detail explanation of this effect has been elaborated in ref. [20]. Furthermore, even being a counterpart of novel photonic edge states, it is evident to see that the band spectrum of phononic results is much clearer than photonic one [46], representing it may be simpler to observe experimentally. Fig. 3.2c-d illustrate the amplitudes at points A and B along a certain transverse cross-section ($N = 20$) of mechanical graphene ribbons. As predicted by band spectrum, the peaks indicate that the vibration of particles is highly confined on the corresponding boundary.

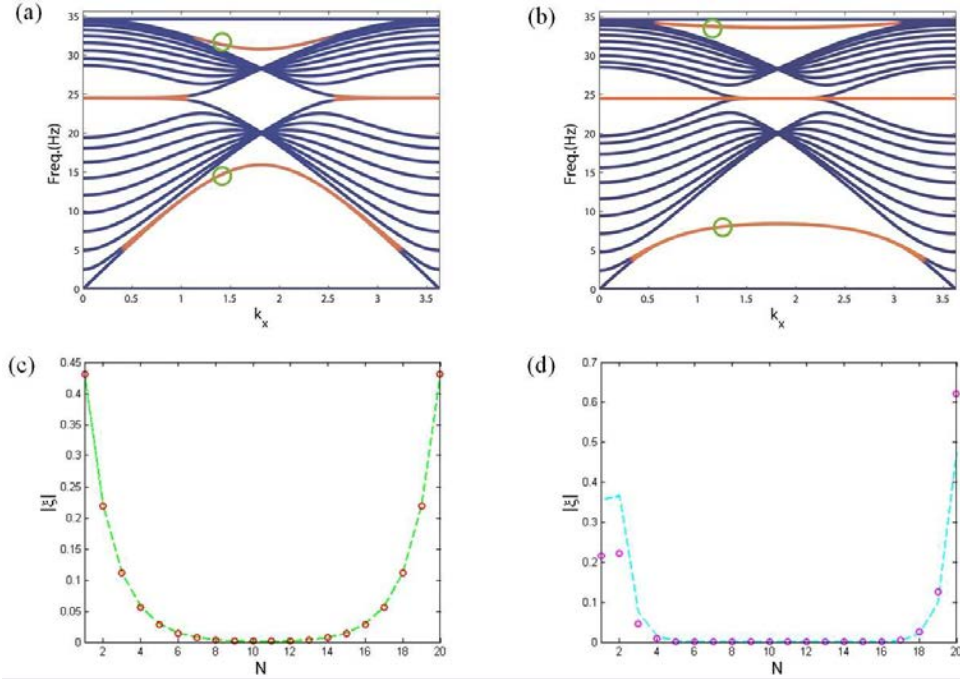


Fig. 3.2: Edge states of mechanical graphene. A mechanical graphene consists of springs with elastic constant $K = 4\text{N/m}$ and mass particles with $M = 10\text{g}$. (a) The 1D band diagram calculated from zigzag spring-mass ribbon. (b) 1D band diagram for bearded edges. (c) The absolute value of amplitudes for zigzag edge states, the green dashed line corresponds to the top edge state and the red circles are to the opposite one. (d) Its absolute value of amplitudes of Fig. 3.2b for both edge states. In this figure, all the parameters are the same as the Fig. 3.1.

3-2: Topological Mechanical Waves

In the previous section, we have discussed edge states in the gapless system by searching the existence of Dirac points. Since it is well-known that degeneracies are intimately relevant to symmetries in the system, it will open bandgaps through breaking them. As a result, we aim to discuss two approaches to lift a gap from Dirac points in this section. For the bulk band diagram, their outcomes are physically identical except a small deviation of eigen-frequency in momentum space. However, in the view of the projected band structure, it helps us distinguish the major discrepancies between the gaps lifted by breaking different symmetries. In what follows, the symmetries: spatial and TR symmetry, are taken as examples.

I. Breaking Spatial Symmetry via AB sublattices: Topologically Trivial Case

If we consider two particles with distinct mass magnitudes (AB sublattice) in a honeycomb unit cell, the governed equations are expressed as

$$M_1 \ddot{\xi}_{mn} = -K \left[\hat{\mathbf{R}}_1 \hat{\mathbf{R}}_1 \cdot (\xi_{mn} - \eta_{mn}) + \hat{\mathbf{R}}_2 \hat{\mathbf{R}}_2 \cdot (\xi_{mn} - \eta_{m-1,n}) + \hat{\mathbf{R}}_3 \hat{\mathbf{R}}_3 \cdot (\xi_{mn} - \eta_{m,n-1}) \right],$$

$$M_2 \ddot{\eta}_{mn} = -K \left[\hat{\mathbf{R}}_1 \hat{\mathbf{R}}_1 \cdot (\eta_{mn} - \xi_{mn}) + \hat{\mathbf{R}}_2 \hat{\mathbf{R}}_2 \cdot (\eta_{mn} - \xi_{m+1,n}) + \hat{\mathbf{R}}_3 \hat{\mathbf{R}}_3 \cdot (\eta_{mn} - \xi_{m,n+1}) \right],$$

where M_1 and M_2 denote the mass for particle A and B, respectively. Apparently, introducing two distinct mass particles breaks inversion symmetry ($\mathbf{r} \rightarrow -\mathbf{r}$) so that the degeneracies stabilised by it will be lifted. Correspondingly, the projected band structures are depicted in Fig. 3.3. The middle gap arises but there are no crossing edge states between edge states. Consequently, despite edge states inheriting from the Dirac points, the entire system turns out to become a conventional gapped one, which provides no topological interests.

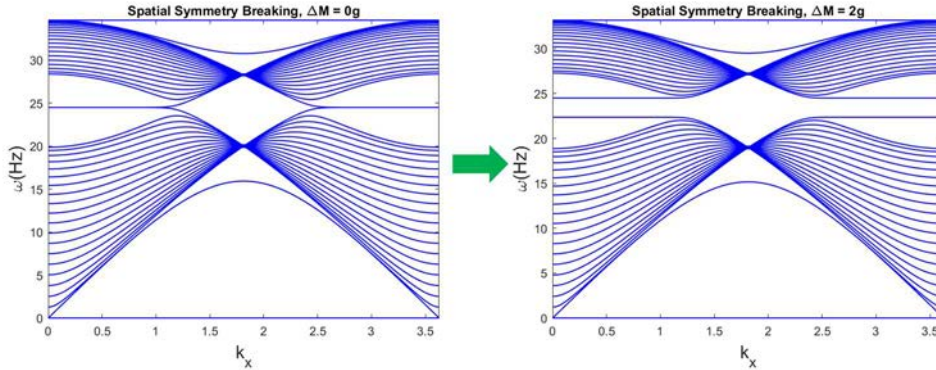


Fig. 3.3: Projected frequency bands for a mass-spring ribbon (P breaking). The parameters are given as follows: $M_1 = 12\text{g}$, $M_2 = 10\text{g}$, $K = 4\text{N/m}$, and $\Delta M = M_1 - M_2$. Despite the emergence of bandgap between 2nd and 3rd bands, there exist no gapless edge states indicating a topologically trivial case.

II. Breaking TR Symmetry via Magnetic Fields: Topologically Nontrivial Case

Aside from spatial symmetry breaking, applying the magnetic field gives rise to TR symmetry breaking which lifts a gap from degeneracies guaranteed by it. In the similar manner to lattice quantum-Hall-effect edge states, we assume every particle has a charge Q and apply a constant and uniform magnetic field \mathbf{B} along the z direction of spring-mass ribbon. For simplicity, here we assume Coulomb interaction makes no contribution to the motion. As a result, we have the

Lagrangian of the system in the presence of magnetic fields

$$L = \sum_{m,n} \left(\frac{M}{2} \dot{\xi}_{mn}^2 + \frac{M}{2} \dot{\eta}_{mn}^2 \right) + Q \sum_{m,n} \left[\mathbf{A}(\mathbf{r}_A + \xi_{mn}) \cdot \dot{\xi}_{mn} + \mathbf{A}(\mathbf{r}_B + \eta_{mn}) \cdot \dot{\eta}_{mn} \right] - \sum_{m,n} \frac{C}{2} \left\{ \left[\hat{\mathbf{R}}_1 \cdot (\xi_{mn} - \eta_{mn}) \right]^2 + \left[\hat{\mathbf{R}}_2 \cdot (\xi_{mn} - \eta_{m-1,n}) \right]^2 + \left[\hat{\mathbf{R}}_3 \cdot (\xi_{mn} - \eta_{m,n-1}) \right]^2 \right\}. \quad (3-9)$$

Here $\mathbf{r}_A = \mathbf{r}_{mn} - \mathbf{R}_2/2$, $\mathbf{r}_B = \mathbf{r}_{mn} + \mathbf{R}_2/2$, is the original positions between the two spherical objects in the mn cell, and \mathbf{A} is the vector potential, that is $\mathbf{B} = \nabla \times \mathbf{A}$. Through using the Euler-Lagrange equations, in the same manner we obtain two equations of motion as

$$M\ddot{\xi}_{mn} + QB \times \dot{\xi}_{mn} = -C \left[\hat{\mathbf{R}}_1 \hat{\mathbf{R}}_1 \cdot (\xi_{mn} - \eta_{mn}) + \hat{\mathbf{R}}_2 \hat{\mathbf{R}}_2 \cdot (\xi_{mn} - \eta_{m-1,n}) + \hat{\mathbf{R}}_3 \hat{\mathbf{R}}_3 \cdot (\xi_{mn} - \eta_{m,n-1}) \right], \quad (3-10)$$

$$M\ddot{\eta}_{mn} + QB \times \dot{\eta}_{mn} = -C \left[\hat{\mathbf{R}}_1 \hat{\mathbf{R}}_1 \cdot (\eta_{mn} - \xi_{mn}) + \hat{\mathbf{R}}_2 \hat{\mathbf{R}}_2 \cdot (\eta_{m,n} - \xi_{m+1,n}) + \hat{\mathbf{R}}_3 \hat{\mathbf{R}}_3 \cdot (\eta_{m,n} - \xi_{m,n+1}) \right]. \quad (3-11)$$

As far as above is concerned, by Fourier decomposition we find

$$\omega^2 \xi + i\omega \omega_c \mathbf{z} \times \xi = \omega_0^2 \left[\hat{\mathbf{R}}_1 \hat{\mathbf{R}}_1 \cdot (\xi - \eta) + \hat{\mathbf{R}}_2 \hat{\mathbf{R}}_2 \cdot (\xi - p^* \eta) + \hat{\mathbf{R}}_3 \hat{\mathbf{R}}_3 \cdot (\xi - \eta_{n-1}) \right], \quad (3-12)$$

$$\omega^2 \eta + i\omega \omega_c \mathbf{z} \times \eta = \omega_0^2 \left[\hat{\mathbf{R}}_1 \hat{\mathbf{R}}_1 \cdot (\eta - \xi) + \hat{\mathbf{R}}_2 \hat{\mathbf{R}}_2 \cdot (\eta - p\xi) + \hat{\mathbf{R}}_3 \hat{\mathbf{R}}_3 \cdot (\eta - \xi_{n+1}) \right], \quad (3-13)$$

in which $\omega_c = QB/M$ is the cyclotron frequency. Further simplification gives us an eigenvalue

problem $\mathbf{H}_M \mathbf{x} = \omega \mathbf{x}$, where $\mathbf{H}_M = -i\omega_c \mathbf{U}/2 + \sqrt{\mathbf{W}}$, $\mathbf{W} = \omega_0^2 \mathbf{H} + \omega_c^2 \mathbf{I}/4$, \mathbf{I} is an identity matrix,

and

$$\mathbf{U} = \begin{bmatrix} 0 & -1 & & \\ 1 & 0 & -1 & \\ & 1 & \ddots & \\ & & & \ddots \end{bmatrix}_{4N \times 4N}$$

The band structures illustrated in Fig. 3.4a-c are given by solving above eigenvalue equations with zigzag truncations. Beginning by zero magnetic fields, Fig. 3.4a shows the projected band structure as demonstrated in Fig. 3.2. With different strengths of the magnetic field (from 0, 20, to 80 T), non-trivial band gaps are lifted because of TR symmetry breaking. As $\mathbf{B} = 20$ T, three sets of edge states arise between bands. Note that the middle flat edge states are now changed into the ones with non-zero group velocity so that the oscillation of objects carrying energy propagates only in one way on the edge with topological protection.

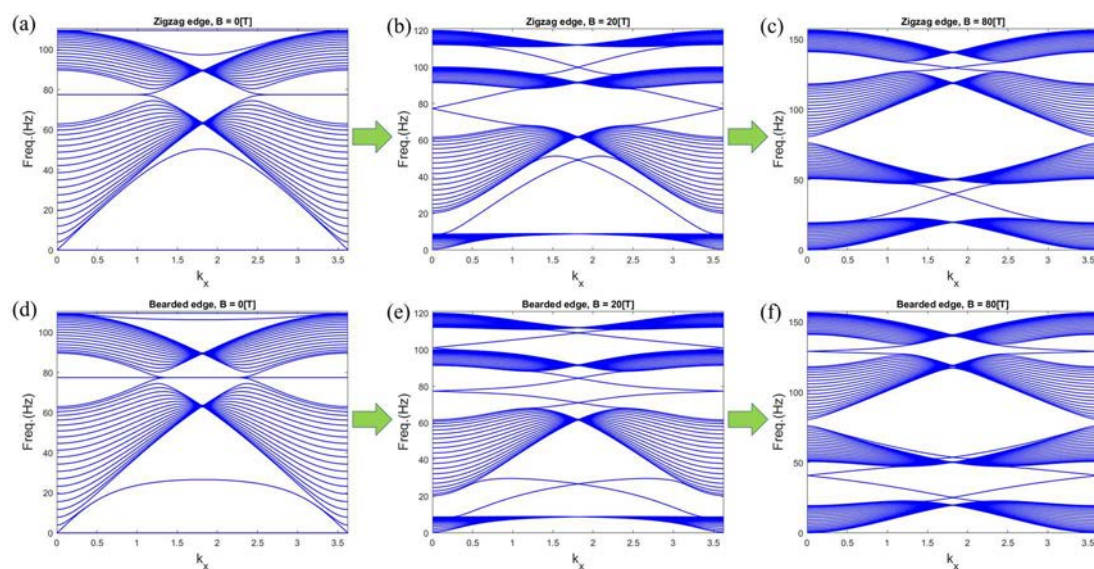


Fig. 3.4: Projected frequency bands for a mass-spring ribbon (TR breaking). The parameters are given as follows: $M = 1\text{g}$, $K = 4\text{N/m}$, and $Q = 1\text{mC}$. The plots for topological edge state with zigzag (a-c) and bearded (d-f) truncation. Spawning from (a) zigzag and (d) bearded truncated spring-mass strips, as the magnitudes of magnetic field increase from 20 to 80 T, topological band gaps are lifted, which turn the middle bandgap into a trivial one after the critical point $\mathbf{B} = 75$ T.

In the meantime, as predicted, other edge states also show a linearly cross band pattern, so that the nearly constant group velocities are found. Yet, when the external field strength reaches to around 75 T, the second and third band touch each other that eliminates their topological phases, and then edge states between them vanish because of the topological transition. If we keep raising the strength of magnetic fields up to 80 T, in Fig. 3.4c the middle gap reopens while it has been converted into a trivial one. In other words, as seen in Fig. 3.4c, there exist no topological edge states within the second and third band. Fig. 3.4d-f illustrates

the case of bearded boundary truncation. Despite the identical bulk band region to zigzag truncation, the feature of bearded edge states is apparently distinct due to the change of boundary geometry.

All in all, for generating topologically protected edge states, it is necessary to have edge states in a gapless system (mother system) by looking up the existence of Dirac degeneracies. Next step, one needs to break TR symmetry via applying external or synthetic fields to open topological non-trivial gaps (daughter system). At some points in parametric space, say magnetic fields, additional topological transitions might happen, which eliminates/creates the topological order and trivialises/non-trivialises certain bandgaps. Similar logic is applicable to any kinds of periodic systems with band diagrams.

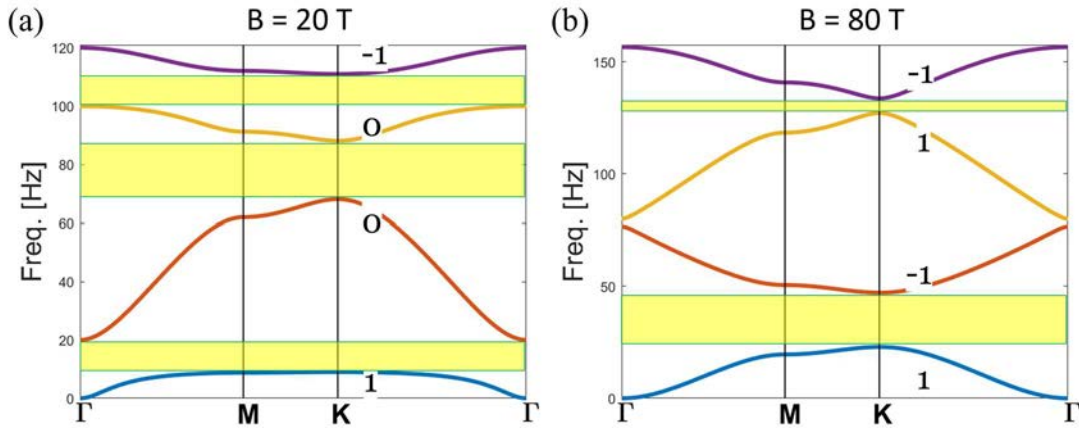


Fig. 3.5: Chern number calculation for bands. The bold black numbers indicate Chern number for each band while the magnetic field equals (a) 20 T and (b) 80 T. The yellow shaded areas highlight the topologically non-trivial bandgaps.

So far, we have thoroughly demonstrated the mechanical edge states in a spring-mass system. To further investigate the topological order of edge states, we have numerically evaluated Chern number for each band. Following the concepts in chapter two, the formula of Chern number is expressed as $C_n = (1/2\pi) \int_{BZ} d^2\mathbf{k} \cdot \mathbf{\Omega}_n$, where $\mathbf{\Omega}_n = i \langle \nabla_{\mathbf{k}} n | \times | \nabla_{\mathbf{k}} n \rangle$ is the Berry curvature for the n th band, and BZ means that the integration is taken throughout the first Brillouin zone. In Fig. 3.5a, the result shows that, at $\mathbf{B} = 20$ Tesla, Chern numbers from bottom

to top band are given as $[1, 0, 0, -1]$. It shows edge states in bands are topologically protected in association with net Chern number $|\Delta C| = 2$. When \mathbf{B} reaches 75 Tesla, as we mentioned before, a topological transition occurs, and therefore, in Fig. 3.5b the Chern number for bands become $[1, -1, 1, -1]$. The system now exhibits topologically non-trivial phase difference $|\Delta C| = 2$ within 1st – 2nd and 3rd – 4th band because of the topological transition, but in the central gap, the topological order now vanishes so no edge states exist. The numerical result matches the consequence shown in Fig. 3.4.

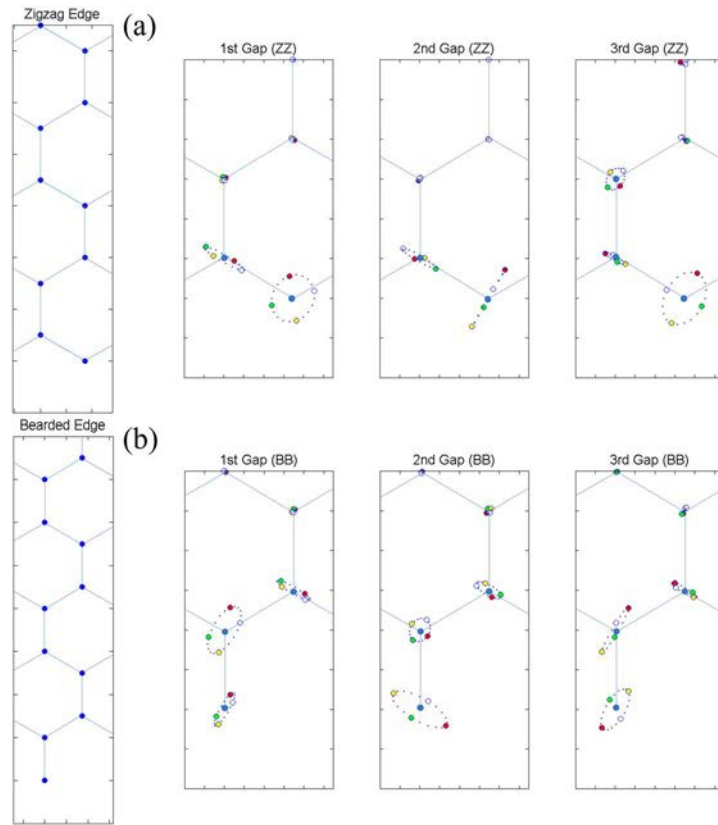


Fig. 3.6: Snapshots of edge states in a spring-mass strip for $\mathbf{B} = 20$ T. Snapshots of edge states at the boundary truncated by (a) zigzag and (b) bearded type. The motion of particles follows the red-green-yellow-white colour sequence and the cyan dots are the original position of particles. The same colour represents the position of particles at the same time.

On the other hand, Fig. 3.6 shows the snapshots of propagating eigenmodes for three edge states at the zigzag and bearded truncation via marking particles in different colours. It is evident to see that three edge states within different gaps are localised at one of the edges. With

the time order marked in a red-green-yellow-white colour sequence, in Fig. 3.6a, the first edge state expresses a counter-clockwise rotation for all the particles. The second one, however, presents fairly linear movement caused from the superposition of right and left-handed motions. Due to this mixed polarisation, its corresponding frequency is reasonably higher than previous one. For the third one, this anti-symmetric edge state gives rise to the highest operating frequency in the band diagram. In Fig. 3.6b, the cases with bearded boundary shows the similar feature comparing with zigzag-truncated systems except the modes in the middle bandgap, which has no linear vibration rather than two chiral modes distributed at different mass points.

Despite the validity of theoretical prediction, it is still impractical to realise our model because of the Coulomb force and extremely high external fields. In general, Coulomb force between two charge objects is much stronger than Lorentz force, so that it is unlikely to avoid the dominant of electric forces in the proposed model. Additionally, reaching magnetic fields to tens Tesla is a nearly impossible condition in the experiment. To overcome these drawbacks, next section we will provide another feasible system, which gives the strong enough effective magnetic field and gets rid of the complexity caused by Coulomb forces.

III. Breaking TR Symmetry via Coriolis Force: Topologically Nontrivial Case.

In classical mechanics, objects moving in a non-inertial reference frame experiences inertial forces resulting in corrections to the equation of motion. Especially, for the coordinate system moving in uniformly rotational manner, two kinds of additional loads applying on objects are known as *Centrifugal force* and *Coriolis force*. Let us first account for a particle doing simple harmonic oscillation on a rotating round plate with the constant angular velocity \mathbf{W} , its Lagrangian in terms of r and v can be expressed as [47]

$$L = \frac{M}{2} v^2 - \frac{K}{2} r^2 + \frac{M}{2} (\mathbf{W} \times \mathbf{r})^2 + M \mathbf{v} \cdot (\mathbf{W} \times \mathbf{r}).$$

The first two terms denote normal simple harmonic oscillation, the third resulting in a correction term of elastic potential energy is the centrifugal force, and the fourth indicates the Coriolis force. Defining that a factor $\mathbf{A} = (\mathbf{W} \times \mathbf{r})/2$ as a counterpart of Landau gauge in quantum physics, Lagrangian can be rewritten as

$$L = \frac{M}{2} v^2 - \frac{(K - MW^2)}{2} r^2 + 2M\mathbf{A} \cdot \mathbf{v}.$$

Comparing with the Lagrangian of the simple harmonic oscillation for a charged particle in constant magnetic fields, i.e. $L = Mv^2/2 + kx^2/2 + Q\mathbf{A} \cdot \mathbf{v}$, it is clear to see that the Lagrangian of rotating reference frame can be analogous to the 2D system applied by a constant magnetic field along the normal direction with the corrected elastic constant and relevant “charge” $Q = 2M$. Back to our case, according to above discussion, we can write down the Lagrangian of the system in rotational circumstance

$$\begin{aligned} L = & \frac{M}{2} \sum_{m,n} (\dot{\xi}_{mn}^2 + \dot{\eta}_{mn}^2) + M \sum_{m,n} [\mathbf{W} \times (\mathbf{r}_0 + \mathbf{r}_A + \xi_{mn}) \cdot \dot{\xi}_{mn} + \mathbf{W} \times (\mathbf{r}_0 + \mathbf{r}_B + \eta_{mn}) \cdot \dot{\eta}_{mn}] \\ & - \frac{K}{2} \sum_{m,n} \left\{ [\hat{\mathbf{R}}_1 \cdot (\xi_{mn} - \eta_{mn})]^2 + [\hat{\mathbf{R}}_2 \cdot (\xi_{mn} - \eta_{m-1,n})]^2 + [\hat{\mathbf{R}}_3 \cdot (\xi_{mn} - \eta_{m,n-1})]^2 \right\} \quad , \quad (3-14) \\ & + \frac{M}{2} \sum_{m,n} \left\{ [\mathbf{W} \times (\mathbf{r}_0 + \mathbf{r}_A + \xi_{mn})]^2 + [\mathbf{W} \times (\mathbf{r}_0 + \mathbf{r}_B + \eta_{mn})]^2 \right\} \end{aligned}$$

Here \mathbf{r}_0 is the radius of round plate. Since the centrifugal term of Lagrangian only gives rise to a correction of equilibrium position, it will be neglected in the following paragraph and elaborate its influence later. In the same manner, two equations of motion are written as

$$\omega^2 \xi + 2i\omega \mathbf{W} \times \xi = \omega_0^2 \left[\hat{\mathbf{R}}_1 \hat{\mathbf{R}}_1 \cdot (\xi - \eta) + \hat{\mathbf{R}}_2 \hat{\mathbf{R}}_2 \cdot (\xi - p^* \eta) + \hat{\mathbf{R}}_3 \hat{\mathbf{R}}_3 \cdot (\xi - \eta_{n-1}) \right], \quad (3-15)$$

$$\omega^2 \eta + 2i\omega \mathbf{W} \times \eta = \omega_0^2 \left[\hat{\mathbf{R}}_1 \hat{\mathbf{R}}_1 \cdot (\eta - \xi) + \hat{\mathbf{R}}_2 \hat{\mathbf{R}}_2 \cdot (\eta - p\xi) + \hat{\mathbf{R}}_3 \hat{\mathbf{R}}_3 \cdot (\eta - \xi_{n+1}) \right]. \quad (3-16)$$

Comparing with Eq. (3-11) and (3-12), we find that angular velocity in here is linked to cyclotron frequency with the relation $2W = \omega_c$. As stated, to open a significantly large bandgap, it is necessary to increase the magnitude of magnetic fields over tens of Tesla. However, only tens rad/s angular frequency, which can be readily achieved in the practical situation, is required to have the same behaviour in a spring-mass ribbon. Besides, avoiding from strong applied field and any presented electric charge, it is no need to consider the complexity caused from Coulomb interactions. Consequently, using the concept of moving on rotational coordinate makes the system more feasible in comparison with the same phenomenon by applying a constant magnetic field. Next, the equilibrium position correction is included in discussion, under the approximation $C \gg MW^2$, corrected equations of motion are given by

$$\begin{aligned} \omega^2 \xi + 2i\omega \mathbf{W} \times \xi = \\ \omega_0^2 \left[\hat{\mathbf{R}}_1 \hat{\mathbf{R}}_1 \cdot (\xi - \boldsymbol{\eta} - \mathbf{d}_{mn}^A) + \hat{\mathbf{R}}_2 \hat{\mathbf{R}}_2 \cdot (\xi - p^* \boldsymbol{\eta} - \mathbf{d}_{mn}^A) + \hat{\mathbf{R}}_3 \hat{\mathbf{R}}_3 \cdot (\xi - \boldsymbol{\eta}_{n-1} - \mathbf{d}_{mn}^A) \right], \\ \\ \omega^2 \boldsymbol{\eta} + 2i\omega \mathbf{W} \times \boldsymbol{\eta} = \\ \omega_0^2 \left[\hat{\mathbf{R}}_1 \hat{\mathbf{R}}_1 \cdot (\boldsymbol{\eta} - \xi - \mathbf{d}_{mn}^B) + \hat{\mathbf{R}}_2 \hat{\mathbf{R}}_2 \cdot (\boldsymbol{\eta} - p\xi - \mathbf{d}_{mn}^B) + \hat{\mathbf{R}}_3 \hat{\mathbf{R}}_3 \cdot (\boldsymbol{\eta} - \xi_{n+1} - \mathbf{d}_{mn}^B) \right]. \end{aligned}$$

where

$$\mathbf{d}_{mn}^{A,B} = \frac{2\Omega^2}{3\omega_0^2} (\mathbf{r}_{mn}^{A,B} + \mathbf{r}_0). \quad (3-17)$$

Let us consider a practical case possessed large enough non-trivial gaps. Assume that a mass-spring ribbon with characteristic frequency $\omega_0 = 20\text{Hz}$ located on a $\mathbf{r}_0 = 1\text{m}$ round plate and $\mathbf{r}_0 \gg \mathbf{r}_{mn}^{A,B}$. For angular velocity $W = 2 \text{ rad/s}$, the correction derived by Eq. (3-17) is about 0.0067, which is much smaller than displacements of edge states. Hence, as long as the angular

velocity is much less than characteristic frequency, the influence of equilibrium position can be omitted. Even high angular speed applied, one can still set all particles at corrected positions in advance since geometric parameters must be known before fabrication. When round plate starts rotating, all objects thus move back to the right places and system becomes our original design.

In Fig. 3.7a, a scheme plot of mechanical graphene ribbon on a rotating frame is illustrated. The band structure, therefore, can be obtained by solving the eigenvalue Eq. (3-15) and (3-16). For the numerical calculation afterwards, we choose $K = 4 \text{ N/m}$ and $M = 10\text{g}$. Fig. 3.7b to e show the band structures for four angular velocities of the rotating frame as $W = 1, 4, W_c = \sqrt{3K/8M}$, and 15 Hz , respectively. At the lowest rotating speed $W = 1 \text{ Hz}$, interestingly, the top and bottom bands evolve from the originally flat bands in the inertial frame into the ones with finite bandwidth. All three bandgaps are topologically nontrivial because of non-zero Chern number difference arising from TR symmetry breaking, so that there exist topologically protected edge states within each bandgap, as shown in Fig. 3.7b-e.

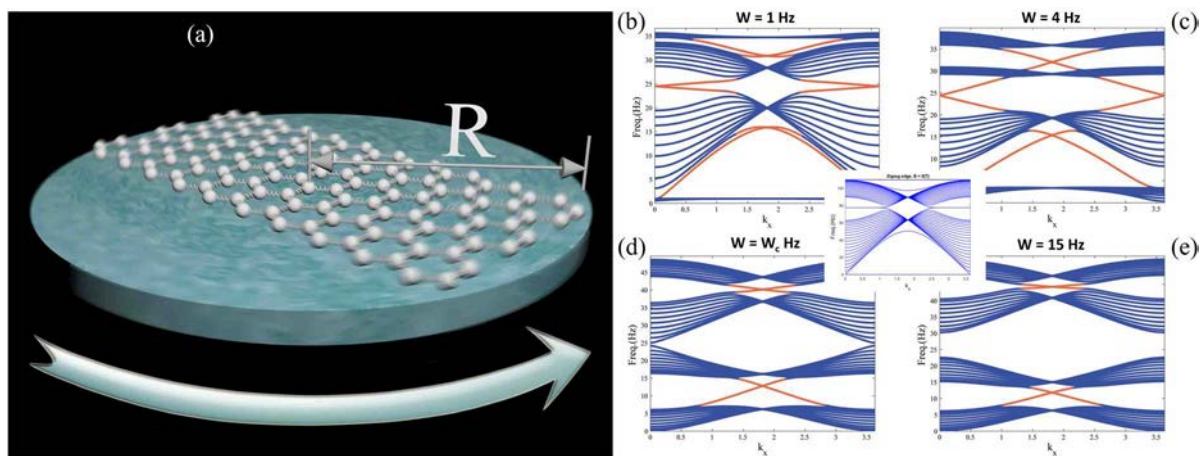


Fig. 3.7: Gapless edge states in mechanical graphene (zigzag). The mass and elastic constant are given as follows: $M = 10\text{g}$ and $K = 4 \text{ N/m}$. (a) A schematic diagram of the non-inertial system. The inset presents the projected band structure in the absence of rotation. With all edge states marked in red, 1D projected band structure for a mechanical ribbon end with zigzag boundary applied constantly angular velocity (b) $W = 1$, (c) $W = 4$, (d) $W = W_c$, and (e) $W = 15 \text{ Hertz}$. Note that wavevector k_x here sticks on rotating frame rather than fixed frame.

As the angular velocity increases to 4 Hz, the band gaps broaden and the dispersion of the edge states become more linear. When the angular velocity reaches to $W_c \sim 12.247$ Hz, the topological transition occurs since the 2nd and 3rd band touch each other. When the angular velocity further increases, the gap reopens but is now converted into a trivial one, which does not contain any edge states due to the band crossing, as shown in Fig. 3.7d. Fig. 3.8a-d show the bearded edge states under different speeds of rotation. Similarly, the bearded edge states exist in every band gap as the angular velocity is less than W_c . Due to band inversion, topological phase transition occurs at 2nd and 3rd band after reaching to the critical angular frequency.

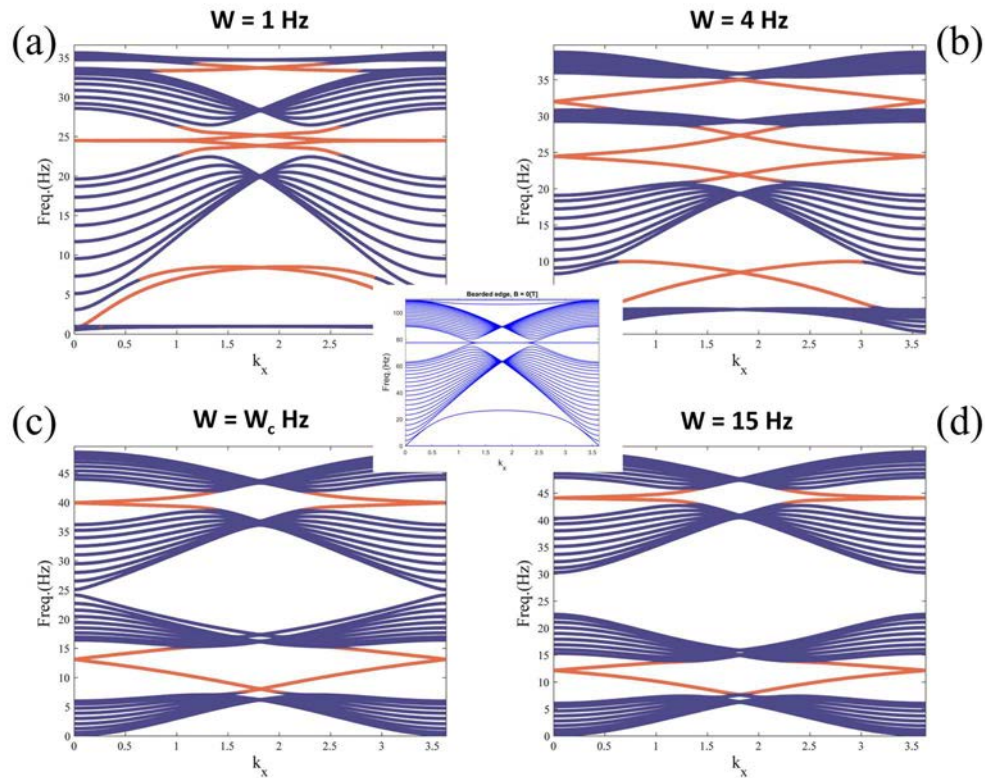


Fig. 3.8: Gapless edge states in mechanical graphene (bearded). Band diagram in one dimension for a mass-spring ribbon end with bearded boundary applied constantly angular velocity at (a) $W = 1$, (b) $W = 4$, (c) $W = W_c$, and (d) $W = 15$ Hertz. The inset in the middle of figure presents the projected band structure in the absence of rotation. All the edge states are marked in red and the parameters are identical to Fig. 3.7.

In conclusion of this section, we have proposed a mechanical graphene - a honeycomb lattice plane consisting of rigid bodies and soft springs. When placed in a rotating frame,

mechanical graphene generates non-trivial frequency gaps that leads to topological one-way edge states. Due to the simplicity of the system, these topological vibrational modes induced by Coriolis forces can be experimentally observed at low-frequency cases.

3-3: Effective Spin-Orbit Coupling in Mechanical Graphene

In this section, the effective spin-orbit coupling (SOC) in mechanical graphene will be discussed. In atomic physics, SOC is an interaction between a particle's motion and spin, which accounts for the physical origin of the fine structure in early quantum mechanics development. In condensed matter physics, SOC plays very important role in understanding various interesting phenomena and generating diverse applications. One of the examples is that a strong spin-orbit interaction in ferromagnetic materials is able to generate a significant intrinsic magnetic field that gives rise to the anomalous Hall states. In the regime of semiconductors, SOC can be categorised into a generic symmetry-independent type, which exists in every material system, and a symmetry-dependent type such as Rashba and Dresselhaus SOC. More recently, the latter type has drawn enormous attention as they lead to interesting phenomena in spintronics such as spin-Hall effect for weak interaction [16], anomalous Hall effect [48] and anomalous spin-Hall effect [49] for strongly coupled systems.

Inspired by the progress of SOC related physics in electronic regime, effective SOC has been found in a variety of other physical systems including optics and acoustics. For example, in photonics, by defining the left (right) circular polarisation of light as spin up (down) state, the spin-Hall effect of light [50-52] has been proposed to describe a relative lateral shift between the two spin polarisation states as light undergoes refraction or reflection at an interface between two different dielectric media. In addition, an effective intrinsic SOC realised

by metamaterial structures has been put forward to mimic the KM model in graphene [11] and to realise 2D photonic topological insulators [5]. In phononics, similar spin-dependent splitting effects are also theoretically predicted for elastic waves travelling through an interface [53]. Besides, the SOC concept has been theoretically predicted [54] and experimentally [55] verified for polaritons that exist in a quantum well embedded in a microcavity. Furthermore, due to the fact TE and TM polarisations of photons are coupled inside microcavities [56], the dispersion diagram of a cavity-photonic crystal exhibits a Dresselhaus SOC at the K point [57].

The physics occurring in photonic systems can be intuitively linked to classical vibrating systems. A similar analysis of modes can be applied on the elastic waves or classical vibration since they naturally consist of longitudinal and transverse components. In subsequent content, we will introduce a mechanical graphene possessing longitudinal-transverse (LT) splitting which gives rise to an effective intrinsic Dresselhaus type SOC. The proposed system opens new perspectives towards manipulation of mechanical waves in artificial mechanical metamaterials. Moreover, amongst all intriguing phenomena induced by spin-orbit interaction, the spin-Hall effect is arguably the most important one owing to its potential to future spintronic devices. Spin-Hall effects is a transverse spin current driven by the electronic current, which could be caused by either intrinsic [58-59] or extrinsic SOC [60]. We will also propose an analogue of spin-Hall effect based on an effective SOC of classical vibration. In what follows, we demonstrate a spin-wavevector correlated propagation for classical vibrations in a mechanical graphene, i.e. elastic spin-Hall effect (ESHE). Here we emphasise that this effect has a different physical mechanism in comparison to spin Hall effect of phonons [53], which describes the lateral displacements as a wave packet passes through an interface between two different elastic materials. In addition, we propose an equivalent system for elastic waves,

which is made up of two isotropic elastic solids. The observed phonon dispersion and spin texture verify that they have the same signature of Dresselhaus SOC.

In order to introduce the ESHE, we first define “spin” as an in-plane rotation for the centre of mass of a rigid body, i.e. spin up/down for $x \pm iy$, which is also referred to “chiral phonons” in the recent literature [61]. In this section, we begin by discussing the spin-orbit interaction in a mechanical graphene. The system consists of a series of honeycomb-arranged rigid body spheres with mass M , and massless springs with longitudinal elastic constant K_L and transverse one K_T , as shown in Fig. 3.9a. Throughout this section, we assume that all the springs have good linearity and restrict ourselves to taking only in-plane vibrations into consideration. The distance between two NN mass points (A and B) is a and the lattice translation vectors are expressed as $\mathbf{r}_{mn} = m\mathbf{a}_1 + n\mathbf{a}_2$, where $\mathbf{a}_1 = \sqrt{3}a\hat{x}$, $\mathbf{a}_2 = (\sqrt{3}\hat{x} + \hat{y})a/2$.

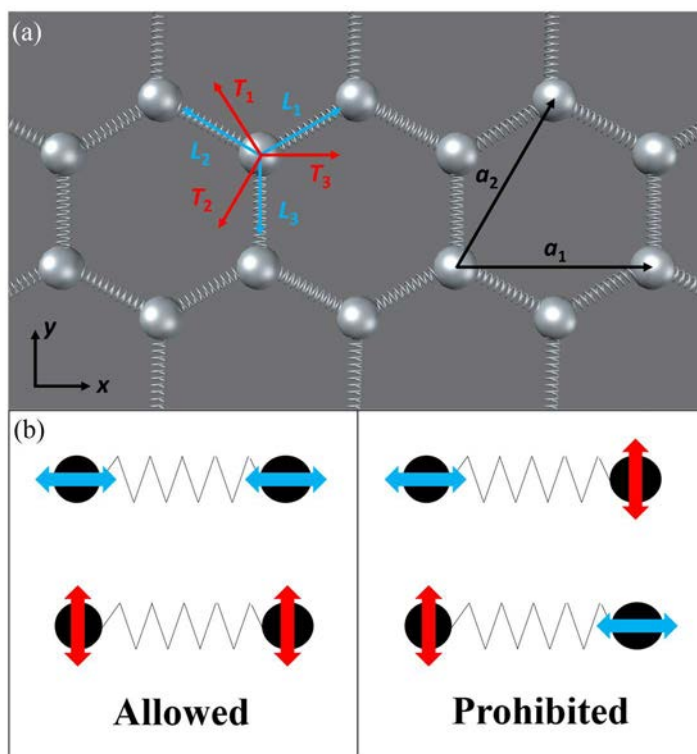


Fig. 3.9: Mechanical Graphene with transverse elastic constants. (a) A part of the mechanical graphene made by soft springs and rigid particles. (b) A schematic sketch of the allowed and prohibited vibrating mode transfer.

The transverse elasticity arises from stretching of the springs, that is to say, the NN distance a at equilibrium is longer than the natural length of the spring [62]. The three longitudinal and transverse unit vectors that connect between the nearest neighbours are

$$\hat{\mathbf{L}}_1 = (\sqrt{3}\hat{\mathbf{x}} + \hat{\mathbf{y}})/2, \hat{\mathbf{L}}_2 = (-\sqrt{3}\hat{\mathbf{x}} + \hat{\mathbf{y}})/2, \hat{\mathbf{L}}_3 = -\hat{\mathbf{y}},$$

$$\hat{\mathbf{T}}_1 = (-\hat{\mathbf{x}} + \sqrt{3}\hat{\mathbf{y}})/2, \hat{\mathbf{T}}_2 = -(\hat{\mathbf{x}} + \sqrt{3}\hat{\mathbf{y}})/2, \hat{\mathbf{T}}_3 = \hat{\mathbf{x}}.$$

By setting the displacements of the A and B as ξ and η , respectively, the variation in length parallel and perpendicular to the spring orientation can be denoted as $\hat{\mathbf{L}}_i \cdot (\xi_{mn} - \eta_{mn})$ and $\hat{\mathbf{T}}_i \cdot (\xi_{mn} - \eta_{mn})$. Fig. 3.9b shows that vibrating mode transfer between the nearest neighbour only occurs between modes of the same vibration direction, whereas that between perpendicular vibration directions is prohibited. Following the preceding description, the equation of motions for mechanical graphene is governed by

$$M\ddot{\xi}_{mn} = -K_L \left[\hat{\mathbf{L}}_1 \hat{\mathbf{L}}_1 \cdot (\xi_{mn} - \eta_{mn}) + \hat{\mathbf{L}}_2 \hat{\mathbf{L}}_2 \cdot (\xi_{mn} - \eta_{m-1,n}) + \hat{\mathbf{L}}_3 \hat{\mathbf{L}}_3 \cdot (\xi_{mn} - \eta_{m,n-1}) \right] - K_T \left[\hat{\mathbf{T}}_1 \hat{\mathbf{T}}_1 \cdot (\xi_{mn} - \eta_{mn}) + \hat{\mathbf{T}}_2 \hat{\mathbf{T}}_2 \cdot (\xi_{mn} - \eta_{m-1,n}) + \hat{\mathbf{T}}_3 \hat{\mathbf{T}}_3 \cdot (\xi_{mn} - \eta_{m,n-1}) \right], \quad (3-13a)$$

$$M\ddot{\eta}_{mn} = -K_L \left[\hat{\mathbf{L}}_1 \hat{\mathbf{L}}_1 \cdot (\eta_{mn} - \xi_{mn}) + \hat{\mathbf{L}}_2 \hat{\mathbf{L}}_2 \cdot (\eta_{mn} - \xi_{m+1,n}) + \hat{\mathbf{L}}_3 \hat{\mathbf{L}}_3 \cdot (\eta_{mn} - \xi_{m,n+1}) \right] - K_T \left[\hat{\mathbf{T}}_1 \hat{\mathbf{T}}_1 \cdot (\eta_{mn} - \xi_{mn}) + \hat{\mathbf{T}}_2 \hat{\mathbf{T}}_2 \cdot (\eta_{mn} - \xi_{m+1,n}) + \hat{\mathbf{T}}_3 \hat{\mathbf{T}}_3 \cdot (\eta_{mn} - \xi_{m,n+1}) \right]. \quad (3-13b)$$

As studied previously [14], there exist four bands in the case $K_L \gg K_T$; two nearly flat bands of transverse modes at zero frequency and $\sqrt{3}\omega_0$, and two bands for longitudinal modes. On the other hand, for a system with K_L slightly different from K_T , the energy of longitudinal (L) and transverse (T) are only slightly different, which implies an energy splitting because of the LT discrepancy. To prove this argument, by setting $K_L = 4\text{N/m}$, and $M = 10\text{g}$, we plot the

frequency dispersions around the irreducible Brillouin zone in Fig. 3.8a-c for $K_T = K_L/8$, $K_L/3$ and $7K_L/8$. Note that even though the magnitude $7K_L/8$ might be unrealistically large, it helps on a clear explanation of SOC. The band structure for $K_T = K_L/8$ gives a Dirac degeneracy at K point with non-flat first and fourth bands, which is consistent with the result shown in ref. [62]. The gap at M between the 2nd and 3rd band closes at $K_T = K_L/3$ and it is observed that the dispersion is linear along direction Γ to M but parabolic along M to K. This type of dispersion can give rise to the trigonal warp effect [63], i.e. there exist three extra Dirac cones in the vicinity of K and K' points. These additional Dirac points are located at the high symmetry line Γ -M because of the three-fold symmetry. At $K_T = 7K_L/8$, band diagram illustrates a very similar splitting pattern to the bilayer graphene [64] or the graphene sheet including Rashba spin-orbit interaction [65].

To identify the nature of this SOC, by altering the original basis to circular bi-polarisation basis $[\psi_A^\uparrow, \psi_A^\downarrow, \psi_B^\uparrow, \psi_B^\downarrow]^T$ with $\psi_{A(B)}^{\uparrow\downarrow}$ representing spinors $[\xi_x(\eta_x) \pm i\xi_y(\eta_y)]/\sqrt{2}$ at A and B lattice, Eq. (3-13) are rewritten to the Bloch Hamiltonian form as

$$\mathbf{H} = \begin{bmatrix} \frac{3K}{M} & 0 & \frac{K}{M}(1+s+p) & \frac{\Delta K}{M} \left[1 - \frac{s+p}{2} - \frac{i\sqrt{3}}{2}(s-p) \right] \\ 0 & \frac{3K}{M} & \frac{\Delta K}{M} \left[1 - \frac{s+p}{2} + \frac{i\sqrt{3}}{2}(s-p) \right] & \frac{K}{M}(1+s+p) \\ h.c. & h.c. & \frac{3K}{M} & 0 \\ h.c. & h.c. & 0 & \frac{3K}{M} \end{bmatrix}, \quad (3-14)$$

where $p = e^{ik \cdot a_1}$, $s = e^{ik \cdot a_2}$, $K = (K_L + K_T)/2$, and $\Delta K = (K_L - K_T)/2$. In Eq. (3-14), if we turn off ΔK , which implies no LT coupling, the Hamiltonian expresses the feature as exactly the same as the graphene with a non-zero bias energy. As ΔK is not equal to zero, the splitting

of phonon dispersion emerges as shown in Fig. 3.10a-c. To confirm this splitting is caused from an effective SOC, we further plot the spin texture of the second band in the vicinity of K point in Fig. 3.10d-f. Note the spin texture depicted in Fig. 3.10 is a 3D spin-vector projection onto k_x - k_y plane, i.e. taking k_x and k_y components from the expectational value of spin operators $\langle \mathbf{s} \rangle_{k_x, k_y} = \langle \psi | \boldsymbol{\sigma} | \psi \rangle_{k_x, k_y}$. It is shown that, regardless of the magnitude of K_T , all the spin textures show similar characteristics to that of Dresselhaus SOC, which originally results from the inversion symmetry breaking in semiconductors as stated in Sec. 2-2.3. In the vicinity of K point $\Delta k_{x,y} a \ll 1$, for a large transverse elastic constant one can derive a low-energy approximation of spin-orbit term in equation (3-14) that matches Dresselhaus SOC near K point as

$$H_D = \frac{3\Delta K}{4M} (\tau_z \sigma_x s_x - \sigma_y s_y), \quad (3-15)$$

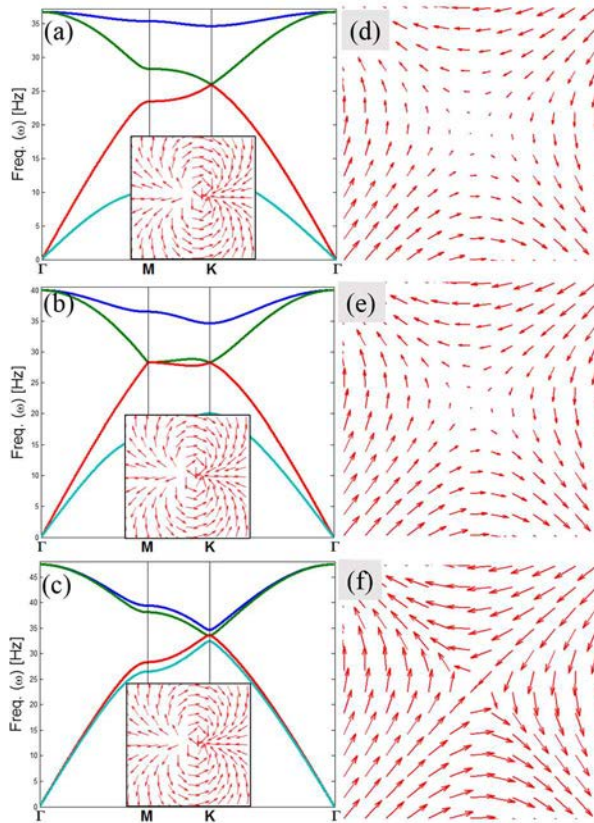


Fig. 3.10: Phonon dispersion and spin texture. (a)-(c) The phonon dispersion for $K_T = K_L/8$, $K_L/3$, and $7K_L/8$ ($M = 10\text{g}$ and $K_L = 4\text{ N/m}$). The insets are projected spin texture around Γ point. (d)-(f) are projected spin textures of the third band for corresponding transverse elastic constants in the vicinity of K point. The length of arrows in spin textures indicates the strength of effective magnetic fields.

where τ_z is the valley degree of freedom and $s_{x,y}$ represent the Pauli matrix for spins. As the rotation motion of the mass describes spin polarisation in mechanical graphene, there exists an effective Dresselhaus field in the system. In this analogue system, the length of arrows can be regarded as the strength of in-plane effective magnetic fields, which is a similar way as the real spins being aligned by real magnetic fields. The insets in Fig. 3.10a-c indicate the corresponding spin textures at Γ point. All three spin textures demonstrate nearly identical patterns indicating the robustness of the effective magnetic field against the change of K_T at Γ point. In contrast, in the vicinity of K(K') points, the effective magnetic fields become weaker as K_T decreases in Fig. 3.10d-f. This feature significantly affects the propagation of spin waves at the K(K') points, which will be discussed in more details in the next section.

3-4: Mechanic Spin-Hall Effect

To figure out how the “spin current” evolves in a mechanical graphene, we assume that the initial condition is a Gaussian pulse source in real space as depicted in Fig. 3.11. After applying the Gaussian source given in Fig. 3.11, with time step $\Delta t = 10$ ms, Fig. 3.12a-c illustrate the evolution of spin fields in real space around several high symmetry points (Γ , K, and K') after 100 time-step iterations. While the wavevector \mathbf{k} is chosen around Γ point, the corresponding Stokes' parameter $\rho_c = I_+ - I_-$, where I is the intensity for two spins, is shown in figure. It is evident to see that the splitting for the four spin polarisations (spin-up in red and spin-down in blue colours) propagates radially in different directions because of the conservation of spin angular momentum. The field distribution shows a four-domain pattern as that of optical spin-Hall effect [54-55]. Fig. 3.12b and c show the ESHE at K and K' point, respectively. There are two spin polarisations in real space propagating in opposite direction, and it gives rise to a reverse splitting of circular polarisation due to the field inversion at K and K' point.

As discussed, the transverse mode could be supported so long as the springs are stretched. Based on the result in ref. [62], one can define a factor α as the ratio between the spring's natural length and NN distance. The transverse elastic constant can be expressed as

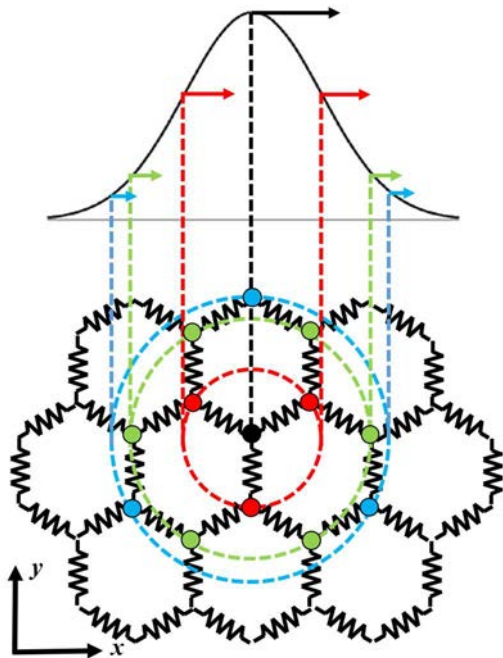


Fig. 3.11: A schematic sketch of the initial displacement distribution. A Gaussian pulse $A_0 \exp\left[-(\mathbf{r} - \mathbf{R}_0)^2 / \alpha^2 - t^2 / \beta^2\right] \exp[i(\mathbf{k} \cdot \mathbf{r} - \omega t)]$ is applied to the middle of the system, where it has a spatial deviation $\alpha = 6a$ and time deviation $\beta = 25$ ms. All the displacements are along x direction and the length of arrows denotes the corresponding displacements in the Gaussian pulse.

$$K_T = K_L(1-\nu) \quad (3-16).$$

Despite the minimum value of ν can reach to zero in principle, its magnitude is roughly limited within the region from 0.2 to 1 so as to keep the linearity of a spring. As such, the large transverse constant in the preceding discussion, $K_T = 7K_L/8$, requires an impractical system with the NN distance almost ten times to the original length of the spring. For a more practical system with a reasonable ratio $\nu = 1/3$, the corresponding K_T is given by $2K_L/3$. Fig. 3.12d-f demonstrate the ESHE field pattern for $\nu = 1/3$ at Γ , K , and K' point after 100 time-step iterations. Fig. 3.12d exhibits similar spin propagation as that in the Fig. 3.12a for $K_T = 7K_L/8$. In fact, we discover that the ESHE at Γ point is not sensitive to the variation of α parameter. It is consistent with the preceding argument for the robustness against the alteration of K_T at Γ point. Even for ν further increased to $1/2$, our simulation shows that the ESHE remains its

four-domain spin-wave-splitting property and radial propagation. However, Fig. 3.12e-f indicate that the ESHE at K and K' point are distinct from Fig. 3.12b-c, but they still fulfil the feature of field inversion. Yet, as shown in Fig. 3.10d-e, the effective fields are weaker for small transverse elastic constant. For such weak field strength, it cannot give rise to an obvious splitting for two spin waves, such that the spin waves are mixed in Fig. 3.12e-f.

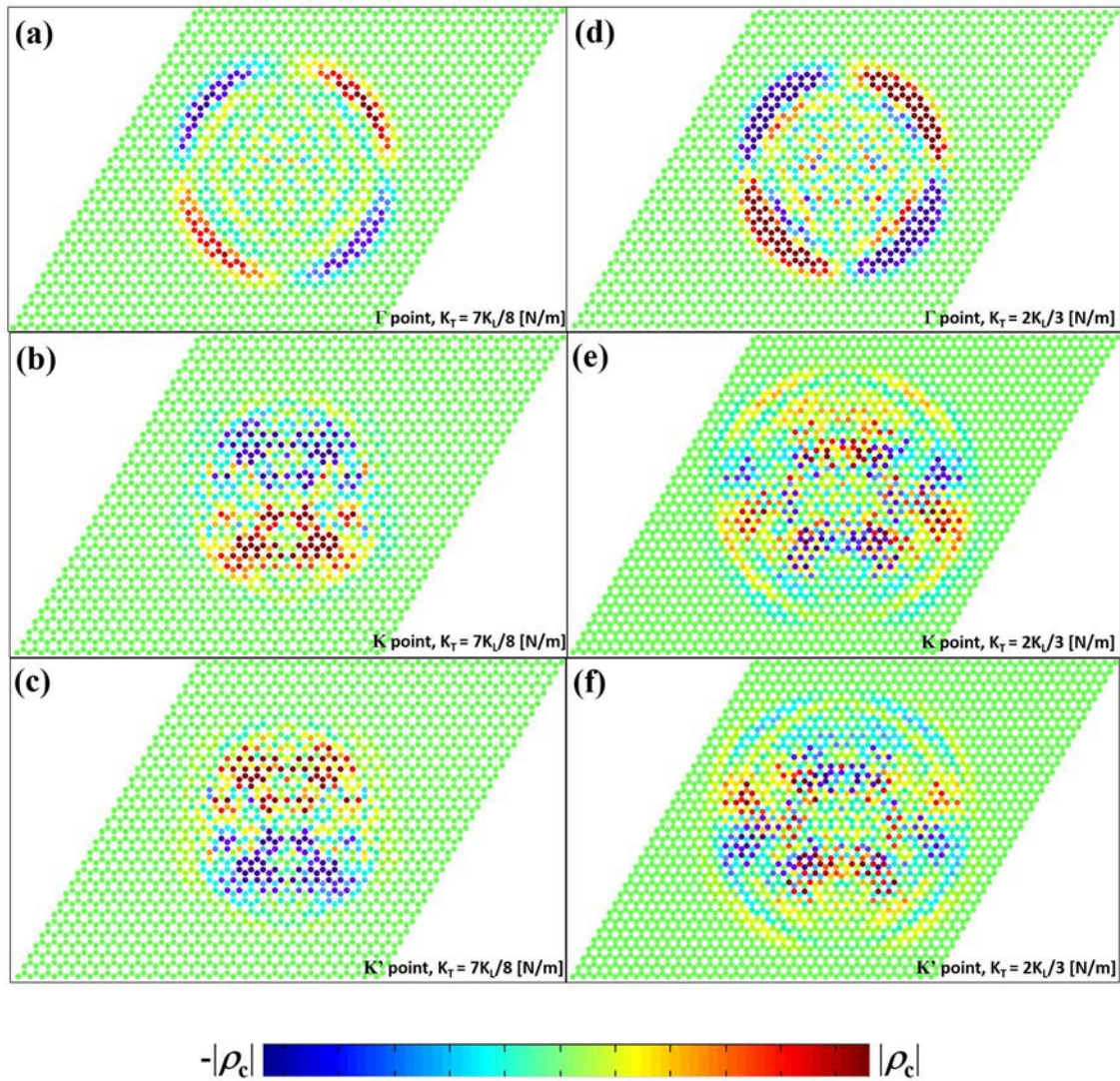


Fig. 3.12: Elastic spin Hall effect.(a)-(c) ESHE for $K_T = 7K_L/8$ N/m in real space while the wavevector \mathbf{k} is chosen around Γ , K and K' point. There are four spin polarisations in (a), two in (b) and (c) propagates separately in distinct orientations. Also (b) and (c) shows a clear inverted field pattern. (d)-(f): ESHE for $K_T = 2K_L/3$ N/m at Γ , K and K' point. It is clear to observe the existence of splitting of spin-envelope propagation. Despite the compliance of field inversion, (e) and (f) show a mixed spin field pattern since the violation of Dresselhaus SOC. Note that for observing a clear evolution for K and K' points, we increase the number of lattices in the system to 35×35 and add the time step up to 150 in Fig. 4(e) and (f).

Besides spring-mass systems, here we propose another equivalent elastic crystal system for realising ESHE. The crystal is made by two isotropic elastic solids. In order to establish the equivalence between the mass-spring system and the elastic crystal, we first deduce the classical Hamiltonian for Eq. (3-13) in terms of the wave vector \mathbf{k} as

$$H = \frac{(\tilde{\Pi}_A^L)^2 + (\tilde{\Pi}_B^L)^2}{2M} + \frac{3K_L}{2} [(\tilde{L}_A)^2 + (\tilde{L}_B)^2] + \frac{(\tilde{\Pi}_A^T)^2 + (\tilde{\Pi}_B^T)^2}{2M} + \frac{3K_T}{2} [(\tilde{T}_A)^2 + (\tilde{T}_B)^2] - \frac{K_L}{2} [(1+p^* + s^*)(\tilde{L}_A\tilde{L}_B + \tilde{L}_B\tilde{L}_A)] - \frac{K_T}{2} [(1+p^* + s^*)(\tilde{T}_A\tilde{T}_B + \tilde{T}_B\tilde{T}_A)], \quad (3-16)$$

where $\tilde{\Pi}_{A(B)}^{L(T)}$ and $\tilde{L}(T)_{A(B)}$ are the canonical momentum and displacement for L and T at A or B lattice, respectively. Eq. (3-16) shows that the local vibration for each mass point can be regarded as a simple harmonic oscillator in the presence of an elastic potential $(3/2)Ku^2$. Besides, the negative coupling term represents the energy transfer from one oscillator to another. The coupling coefficient plays the role of the hopping parameter of nearest neighbours in the tight-binding description. For the sake of simplicity, one can neglect the energy of local simple harmonic oscillators since it only provides a bias and does not affect the main feature of phonon dispersion. In the basis of creation and annihilation operators, the Hamiltonian of a mechanical graphene reads

$$H = -\hbar t_L [a_{L,mn}^\dagger b_{L,mn} + a_{L,mn}^\dagger b_{L,m-1,n} + a_{L,mn}^\dagger b_{L,m,n-1} + \text{h.c.}] - \hbar t_T [a_{T,mn}^\dagger b_{T,mn} + a_{T,mn}^\dagger b_{T,m-1,n} + a_{T,mn}^\dagger b_{T,m,n-1} + \text{h.c.}], \quad (3-17)$$

where the hopping parameter $t_{L(T)} = \omega_{L(T)}/3$ for L and T was introduced. Based on Eq. (3-17), we can extend the ESHE to elastic waves propagating inside a phononic crystal made by embedding tungsten carbide ($\rho = 13800 \text{ kg/m}^3$, $c_l = 6655 \text{ m/s}$, $c_t = 3980 \text{ m/s}$) rods in an aluminium ($\rho = 2690 \text{ kg/m}^3$, $c_l = 6420 \text{ m/s}$, $c_t = 3040 \text{ m/s}$) background. The dispersive

relations in Fig. 3.13 are numerically calculated by COMSOL Multiphysics 5.1, a commercial package using the finite-element method. In Fig. 3.13a, with filling factor equals to 0.4, there is a large band gap for xy mode between the third and fourth band. Through removing rods in honeycomb lattice, a phononic graphene with periodic arrangement of cavities results in extra bands in the bandgap. For those bands generated from cavity modes, the tight-binding description is applicable since every mode is sufficiently localised in a cavity [66]. To find the counterpart of classical vibration, we only take p-orbital into account because its vibrating direction corresponds to the motion of mechanical oscillators. Also, the hopping of the tightly confined state to its neighbour does not introduce the change of polarisation from L to T and vice versa. In accordance with above description, the corresponding equation is naturally identical to Eq. (3-17). The cavity mode in the band gap is plotted in Fig. 3.13b. Its appearance matches the case $K_L \sim K_T$ in mechanical graphene. To further verify its feature of SOC, Fig. 3.13c illustrates the pseudospin texture derived from equation (3-17) at K point in accordance with the fitting central frequency $\omega_0 = 3322.7$ and two hopping parameters $t_L = 3.96$, $t_T = 3.24$ in the unit of Hertz, which gives similar spin distribution to that of spring-mass system. An advantage of cavity-phononic crystals to the spring-mass systems is that they can provide very close L and T elastic constants. Consequently, an effective SOC theory in Sec. 3-3 can be utilised and we predict that ESHE at K(K') point is available for such cavity-phononic crystals.

As a conclusion to Sec. 3-3 and 3-4, the effective spin-orbit coupling in mechanical graphene has been studied. We show that the band structure exhibits a Dresselhaus type of SOC caused by LT splitting. Under the condition of $K_L \sim K_T$, the elastic SHE caused from SOC leads to interesting spin texture that shows up in the field distribution evolution in time. The numerical result verifies the existence of elastic SHE at Γ and K(K') point, which also fits the result given in spintronics and photonics. Surprisingly, in practical condition $K_L \gg K_T$, elastic

SHE still appears in spite of imperfect field inversion at K(K') point. In the final part, we introduce a cavity-phononic crystal that is equivalent to the proposed spring mass system.

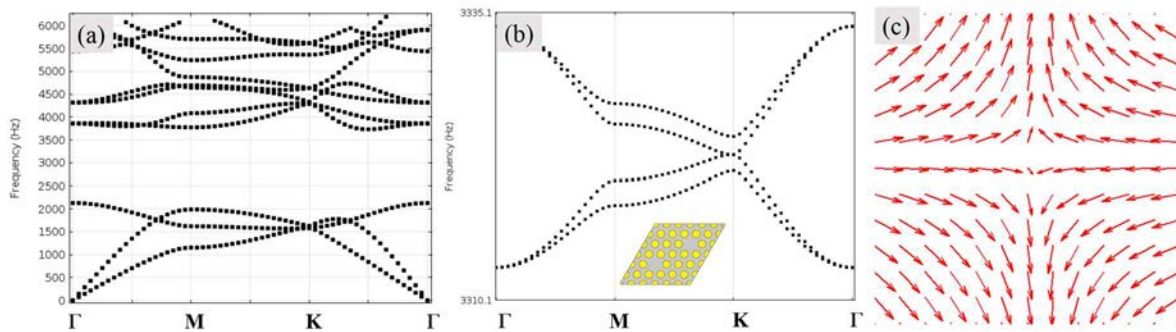


Fig. 3.13: The cavity-phononic crystal.(a) The phononic band structure for tungsten carbide rods embedded in an aluminium background with the lattice constant = 1 m. (b) Cavity-phononic crystal shows the dispersion being similar to Fig. 3.10c. The inset demonstrates the geometry of a unit cell. (c) Spin texture of Dresselhaus SOC around K point. The orientation discrepancy from Fig. 3.10c is caused by the choice of primitive translation vectors.

3-5: Chapter Summary

Throughout this chapter we have demonstrated mechanical graphene providing novel properties in classical vibrations. As illustrated by projected band structures, localised edge states were found between every bulk frequency bands. When TR symmetry is broken by external fields, such as magnetic fields or Coriolis forces induced from rotating frame, the topological phase transition and the one-way edge state can be observed. The Chern number calculation was made to prove the existence of topologically non-trivial bandgap as the difference of Chern number for certain bandgap is not zero. In addition, in the next part of this chapter the effective Dresselhaus type SOC resulted from stretch springs revealed in the description of chiral polarisation of vibration was shown by deducing analytical expressions and emulating spin textures. Exploiting nature from effective SOC terms, we have numerically demonstrated the ESHE under the scenarios of wavevectors $k = 0$ as well as $4\pi/3a$. Despite the extreme condition of realising ESHE at K point, the same phenomenon exhibits in cavity-elastic crystals owing to the nature of LT coupling in elastic solids.

Chapter 4 Topological Elasticity

Phononic crystals (PC) are artificial media consisting of periodic elastic composites that are capable of manipulating the propagation of acoustic or elastic waves, whereas the coupling between the longitudinal and transverse (shear) waves in elastic solids significantly complicates the investigation of PC. However, in a 2D system, shear wave field vibrating in the z direction is decoupled from the in-plane mixed waves so that one can separately study them. In this chapter, firstly we introduce topological phenomena for shear waves via embedding magneto-elastic material into solid background. The result can be regarded as the shear-wave analogue of quantum Hall effect, which have not been proposed in any literature yet. Additionally, the in-plane mode provides a possibility of achieving phononic topological insulating phase. Provided that two Lamé coefficients have the relationship as $\lambda = -\mu$, the longitudinal (L) and transverse (T) are degenerate, leading to topologically non-trivial phases in this in-plane solid mechanical modes. To the best of our knowledge, this is the first proposal of phononic topological insulators. In what follows, the contents in Sec. 4-2 and 4-3 are related to Part B and D in Table II, respectively.

4-1: Introduce to Elastic Waves

Prior to discussing the main text of this chapter, a brief review of classic elastodynamics is introduced in this section [67]. Consider a force acts on the solids, the shape and volume are changed, which is so-called *deformation*. For a point in this solid, its position is denoted by a position vector $\mathbf{r} = (x_1, x_2, x_3)$ where $(x_1, x_2, x_3) = (x, y, z)$. If we define that \mathbf{r} is the position before deformation and \mathbf{r}' is the one after deformation. Thus, the displacement vector in solids is expressed as $\mathbf{r}' = \mathbf{r} + \mathbf{u}$ or

$$u_i = x'_i - x_i. \quad (4-1)$$

It is evident that when deformation happens, the distant between points are altered as well. Thus, one can consider an infinitesimal distant between two positions ds and ds' , the former gives a length before acting force, and the latter presents the one after deformation, namely, $ds = \sqrt{dx_1^2 + dx_2^2 + dx_3^2}$ and $ds' = \sqrt{dx_1'^2 + dx_2'^2 + dx_3'^2}$. According to equation (4-1), we have $dx'_i = dx_i + du_i$. In following sections, the Einstein convention is applied so that $ds = dx_i^2$ and $ds' = (du_i + dx_i)^2$. Besides, as we already knew $du_i = \frac{\partial u_i}{\partial x_k} dx_k$, the relation of deformation yields

$$ds'^2 = ds^2 + 2u_{ik} dx_i dx_k, \quad (4-2)$$

where $u_{ik} = \frac{1}{2} \left(\frac{\partial u_i}{\partial x_k} + \frac{\partial u_k}{\partial x_i} + \frac{\partial u_l}{\partial x_i} \frac{\partial u_l}{\partial x_k} \right)$. As we are interested in the linearised cases, the second-order small quantities are omitted here. u_{ik} , which is called “*strain tensor*”, reads

$$u_{ik} = \frac{1}{2} \left(\frac{\partial u_i}{\partial x_k} + \frac{\partial u_k}{\partial x_i} \right). \quad (4-3)$$

It is worth to mention two properties regarding strain tensors. Firstly, one can readily find that the strain tensor is a symmetric tensor, namely $u_{ik} = u_{ki}$. Secondly, by the definition (4-3), the strain tensor is a dimensionless parameter. After the brief discussion of strain tensors, to further study elastic waves in solids, an essential physical quantity called “*stress tensor*” σ_{ik} should be introduced. Consider a thermal equilibrium system, which means that there is no deformation caused by temperature or external field in the system, one can only take an

infinitesimal volume into account. The total force is $\int \mathbf{F}dV$, where \mathbf{F} is the force acting on unit volume. However, based on Newton's third law of motion, these forces cancel each other in the volume except the one on the surfaces. For the total forces of every unit, they are equal to the forces acting on surfaces of volume only. Above discussion shows that a quantity can be introduced in accordance with Gauss' theorem in vector analysis so that

$$\int F_i dV = \oint \sigma_{ik} ds_k = \int \frac{\partial \sigma_{ik}}{\partial x_k} dV, \text{ or}$$

$$F_i = \frac{\partial \sigma_{ik}}{\partial x_k}. \quad (4-4)$$

When equilibrium condition is applied, the total forces must be zero, and we have equilibrium equation

$$\frac{\partial \sigma_{ik}}{\partial x_k} = 0. \quad (4-5)$$

Regarding the indices of the stress tensor, the first index represents the direction of stress tensor, another is which surface the force acts on. For example, σ_{xx} means the stress tensor along x direction on the x surfaces (*normal stress tensor*), the tangential tensors along y and z direction are σ_{yx} and σ_{zx} (*tangential stress tensor* or *shear tensor*), respectively. Note that normal stress tensors cause the change of volume, this means the acoustic waves in fluid belong a special case of elastic waves. In addition, shear tensors give rise to the change of shapes but maintain the constant volume of solids.

Now we can further discuss the deformation with a slight deviation in equilibrium.

Intuitively, consider the work caused by forces, one obtains where $\int \delta W dV = \int \frac{\partial \sigma_{ik}}{\partial x_k} \delta u_i dV$ is

work in a small volume. By employing integration by parts, and then

$$\int \delta W dV = \cancel{\sigma_{ik} \delta u_{ik}} \Big|_{-\infty}^{\infty} - \int \sigma_{ik} \frac{\partial \delta u_i}{\partial x_k} dV .$$

The first term can be neglected since we assume no existence of stress tensor on the infinitely far surface. Due to the symmetric nature of strain tensors, above equation is denoted as

$$\int \delta W dV = -\frac{1}{2} \int \sigma_{ik} \delta \left(\frac{\partial u_i}{\partial x_k} + \frac{\partial u_k}{\partial x_i} \right) dV = -\int \sigma_{ik} \delta u_{ik} dV \text{ or}$$

$$\delta W = -\sigma_{ik} \delta u_{ik} . \quad (4-6)$$

Moreover, according to the first law of thermodynamic and the definition of free energy $F = U - TS$, we have $dF = -SdT + \sigma_{ik} \delta u_{ik}$. Therefore, another common and useful formula for stress tensors is presented as

$$\sigma_{ik} = \left(\frac{\partial F}{\partial u_{ik}} \right)_T . \quad (4-7)$$

Since we have already known that the free energy is a function of strain tensor, one can expand it to quadratic term as

$$F = F_0 + \frac{\lambda}{2} u_{ii}^2 + \mu u_{ik}^2 , \quad (4-8)$$

where λ and μ are so-called Lamé constants or Lamé coefficients and the constant F_0 is the free energy before deformation. Note that the linear term must be vanished because the free energy is a scalar. Meanwhile, for the sake of simplicity, we also set F_0 is zero in the following paragraph. Plugging equation (4-8) into (4-7), we get

$$\sigma_{ik} = \lambda \delta_{ik} u_{ll} + 2\mu u_{ik} . \quad (4-9)$$

In general, under the condition of isotropic compression ($\sigma_{ik} = -p\delta_{ik}$, where p is pressure), equation (4-9) can be rewritten as

$$F = \frac{B}{2} u_{ll}^2 + \mu \left(u_{ik} - \frac{1}{3} \delta_{ik} u_{ll} \right)^2, \quad (4-10)$$

where B is referred to bulk modulus and its relation of Lamé constant is

$$B = \lambda + \frac{2}{D} \mu, \quad (4-11)$$

where D is the dimension of the system. Now, by substituting equation (4-9) into (4-7), for 3D stress tensors we have

$$\sigma_{ik} = B \delta_{ik} u_{ll} + 2\mu \left(u_{ik} - \frac{1}{3} \delta_{ik} u_{ll} \right). \quad (4-12)$$

It is essential for equation (4-12) that can be regarded as the constitutive relation between displacement field and electric field, namely $\mathbf{D} = \varepsilon \mathbf{E}$. Furthermore, normally in fluid the shear waves are relatively small, thus equation (4-12) reduces to $\sigma_{ik} = B \delta_{ik} u_{ll} = -p \delta_{ik}$, thus $u_{ll} = -p/B$. This formula is the well-known Hooke's law.

In the study of elastodynamics in an isotropic elastic solid, one can simply substitute $F_i \rightarrow -\rho \omega^2 u_i$ in Eq. (4-4). Since only 2D cases ($\partial_z \rightarrow 0$) are discussed in the subsequent contents, Eq. (4-4) can be further simplified into two decoupled equations yielding

$$-\rho \omega^2 u_i = \nabla_{\perp} \cdot \mu \nabla_{\perp} u_i + \nabla_{\perp} \cdot (\mu \partial_i \mathbf{u}_{\perp}) + \partial_i (\lambda \nabla_{\perp} \cdot \mathbf{u}_{\perp}). \quad (4-13a)$$

$$-\rho\omega^2 u_z = \nabla_{\perp} \cdot \mu \nabla_{\perp} u_z. \quad (4-13b)$$

where $\nabla_{\perp} = \hat{e}_x \partial_x + \hat{e}_y \partial_y$, $\mathbf{u}_{\perp} = \hat{e}_x u_x + \hat{e}_y u_y$, and $i = x, y$. It is worth noting that, in Eq. (4-13b), the z -orientation shear modes are governed by a standard wave equation in 2D elastic solids. The mixed xy waves, however, result from the Eq. (4-13a) whose modes are coupled with longitudinal and transverse components. This discrepancy between two elastic waves enables the specific manipulation through engineering the structures and materials.

4-2: Topological Shear Modes

In Chapter three, a discrete system like spring-mass composites has been discussed. Apart from the topological mechanics, classical vibration in a continuum can also possess topological nature under certain circumstance. The recent progress on topological photonic [9-10] has inspired researchers to explore similar phenomena for other classical waves in a continuum. Following the realisation of topologically nontrivial systems in photonics, research groups around the world have extended this concept to pressure acoustics [13]. In general, the generation of topological edge states is achieved through TR symmetry breaking for opening a topologically non-trivial band gap. According to the bulk-edge correspondence principle, topologically protected edge states are present at the boundary. To break TR symmetry in photonics, a feasible way is to utilise the magneto-optical effect in materials such as yttrium-aluminium-garnet (YAG) since photons are uncharged particles that do not directly interact with the magnetic field. On the other hand, if the spin waves and elastic waves operate at close frequencies, the coupling between them results in a new excitation mode. Under a suitable physical condition, the linear coupling between magnetisation and strain give rise to non-reciprocity for elastic waves in the crystalline ferrites. Based on the theory proposed by Kittel [68] and Schlömann [69], the Faraday effect for transverse elastic waves [70] was achieved in

early 1960s. Since then, YAG has been considered as one of the best candidates for realising the transverse acoustic Faraday rotation because of its low-loss property [71].

In addition, phononic crystals (PC) are artificial media composing of periodic elastic composites that can manipulate the propagation of acoustic or elastic waves, whereas the coupling between the longitudinal and transverse (shear) waves in elastic solids significantly complicates the investigation of PC. However, in a 2D system, shear wave field vibrating in the z direction is decoupled from the in-plane mixed waves. Interestingly, the propagating behaviour of pure shear waves is governed by the same wave equations as that of the TM mode (electric fields along z direction) of electromagnetic wave and the pressure wave in acoustics. Therefore, if a 2D PC is constructed using the aforementioned non-reciprocal materials such as YAG under a uniform magnetic field, topological shear edge states are expected to be present in this system.

In this section, we demonstrate the topological edge states of shear waves through magnon-phonon interaction in a finite thickness 2D lattice phononic crystal as shown in Fig. 4.1. This finite thickness 2D PC is made of lossless YAG rods embedded in the epoxy background, in which each rod exhibit magneto-elastic (ME) effect so as to break the TR symmetry. In the absence of magnetic fields, the PC possesses Dirac cones at the K and K' points in the k space. By applying a uniform magnetic field in the z direction, these degeneracies are lifted to form a topologically non-trivial gap. Due to the non-trivial gap, a backscattering-immune one-way shear wave propagating around disorders is numerically discovered. Furthermore, since the finite thickness PC is made of two realistic materials, the corresponding experimental realisation could be readily implemented.

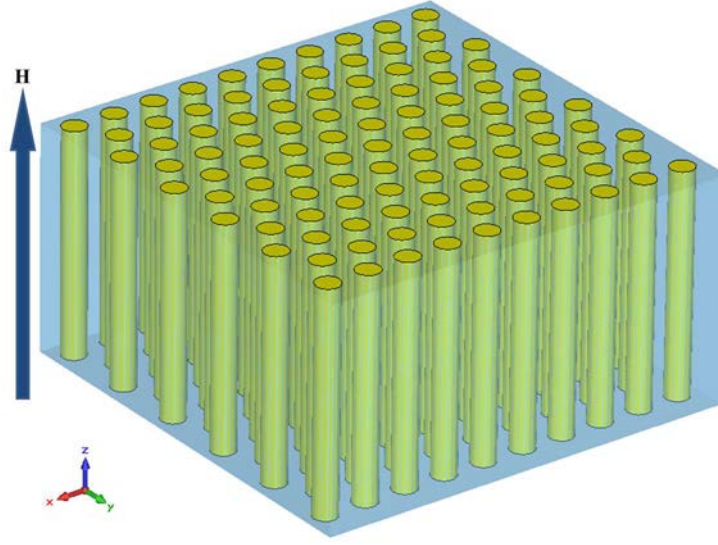


Fig. 4.1: A 2D gyromagnetic phononic crystal. The schematic diagram of a PC made by a finite thickness 2D triangular-lattice arranged YAG rods (yellow) embedded in epoxy background (light blue). The external field \mathbf{H} is applied in the z direction.

We start with a description of the ME effect in bulk YAG. Under a uniform field $\mathbf{H} = H_0 \hat{\mathbf{z}}$ applied along the crystal axis and a major axis of ellipsoid in ref. [71], the five coupled linear equations governing the dynamics of the coupled system (in SI unit) in terms of the small displacement \mathbf{u} , magnetisation m_x and m_y are given as follows:

$$\dot{m}_x = -g_r \left[(H_0 - DN^2) m_y + b (\partial_z u_y + \partial_y u_z) - M (h_y - N_y m_y) \right], \quad (4-14a)$$

$$\dot{m}_y = +g_r \left[(H_0 - DN^2) m_x + b (\partial_z u_x + \partial_x u_z) - M (h_x - N_x m_x) \right], \quad (4-14b)$$

$$\rho \ddot{u}_x = c_{44} \nabla^2 u_x + (c_{12} + c_{44}) \partial_x (\nabla \cdot \mathbf{u}) + (b/M_s) \partial_z m_x, \quad (4-14c)$$

$$\rho \ddot{u}_y = c_{44} \nabla^2 u_y + (c_{12} + c_{44}) \partial_y (\nabla \cdot \mathbf{u}) + (b/M_s) \partial_z m_y, \quad (4-14d)$$

$$\rho \ddot{u}_z = c_{44} \nabla^2 u_z + (c_{12} + c_{44}) \partial_z (\nabla \cdot \mathbf{u}) + (b/M_s) (\partial_x m_x + \partial_y m_y). \quad (4-14e)$$

where ρ , c_{ij} , b , \mathbf{m} , g_r and \mathbf{M}_s are mass density, elastic moduli, ME constant, magnetisation, electron gyromagnetic ratio, and saturation magnetisation, respectively. \mathbf{h} represents the internal in-plane field [71]. D is the “exchange field” term, which is negligible for most materials if $k < 10^7 \text{ m}^{-1}$ [72]. In equations (4-14), the shape of YAG has been set as a thin rod, which means that its demagnetisation factors satisfy $N_z=0$ and $N_x=N_y=1/2$ [73]. From literature [71] it is reasonable to assume that the z component magnetisation $m_z \sim M_s$ and $m_{x,y} \ll M_s$. The elastic stiffness matrix of a bulk YAG can be further simplified as

$$\begin{bmatrix} c_{11} & c_{12} & c_{13} & & & \\ c_{12} & c_{22} & c_{13} & & & \\ c_{13} & c_{13} & c_{33} & & & \\ & & & c_{44} & -ic_{45} & \\ & & & ic_{45} & c_{55} & \\ & & & & & c_{66} \end{bmatrix}, \quad (4-15)$$

where $c_{11} = c_{22} = c_{33} = \lambda + 2\mu$, $c_{12} = c_{13} = \lambda$, $c_{66} = \mu$, $c_{45} = \frac{\gamma(b^2/M_s)\omega}{(\gamma M_s/2 + \gamma H_0)^2 - \omega^2}$,

$c_{44} = c_{55} = \mu - \frac{\gamma^2(b^2/M_s)(M_s/2 + H_0)}{(\gamma M_s/2 + \gamma H_0)^2 - \omega^2}$. Note that, as the H_0 flips sign, saturated magnetisation

M_s also flips its sign because it is induced by the external magnetic field. This leads to a sign change for c_{45} as the direction of applied fields changes.

For the ideal 2D PC system, as all quantities are independent of the z variable, i.e., $\partial_z(\dots) = 0$, and the elastic wave can be decoupled to the in-plane and out-of-plane term [74]:

$$\rho \ddot{u}_i = \nabla_{\perp} \cdot c_{66} \nabla_{\perp} u_i + \nabla_{\perp} \cdot (c_{66} \partial_i \mathbf{u}) + \partial_i [(c_{12} - 2c_{66}) \nabla_{\perp} \cdot \mathbf{u}], \quad (4-16a)$$

$$\rho \ddot{u}_z = \nabla_{\perp} \cdot c_{44} \nabla_{\perp} u_z + i \hat{\mathbf{z}} \cdot [\nabla_{\perp} \times (c_{45} \nabla_{\perp} u_z)]. \quad (4-16b)$$

The index $i = x, y$, $\mathbf{u} = [u_x, u_y]$, and ∇_{\perp} is the gradient operator with respect to x and y . As Eq. (4-16a) describes the longitudinal and transverse elastic waves, they are referred to as “mixed waves” in PCs. Apart from mixed waves, Eq. (4-16b) involving only the out-of-plane component u_z is the master equation for the “pure shear wave”. Defining a new set of parameters $\rho \equiv \varepsilon$, $1/c_{44} \equiv \tilde{\mu}$, $c_{45} \equiv \tilde{\eta}$, and $\psi \equiv \sqrt{1/c_{44}} u_z$, Eq. (4-16b) is perfectly mapped onto a non-relativistic 2D Schrödinger equation [9,13],

$$\left[-|\nabla_{\perp} + i\mathbf{A}_{eff}(r)|^2 + V(r) \right] \psi = 0, \quad (4-17a)$$

where

$$\mathbf{A}_{eff} = (1/2c_{44}) \hat{\mathbf{z}} \times \nabla_{\perp} c_{45}, \quad (4-17b)$$

$$V = \left[|\nabla_{\perp} \ln(1/c_{44})|^2 + |(1/c_{44}) \nabla_{\perp} \ln(c_{45})|^2 \right] / 4 - \left[\nabla_{\perp}^2 \ln(1/c_{44}) + 2\rho\omega^2/c_{44} \right] / 2. \quad (4-17c)$$

Induced by the external magnetic field, \mathbf{A}_{eff} can be regarded as an effective vector potential for elastic waves. In other words, although applying magnetic field cannot directly affect shear waves in conventional solids, the off-diagonal terms of stiffness matrix in ferrimagnetic materials give rise to an effectively magnetic response via ME interaction. In the 2D spinless electronic system, the vector potential resulted from a strong magnetic field gives rise to quantised energy levels so that electrons are able to occupy a number of discretised levels only. This results in the quantised electronic transport is an essential concept of integer quantum Hall effect. Hence, owing to the same configuration of the wave equation, similar phenomena are expected in our elastic PC model.

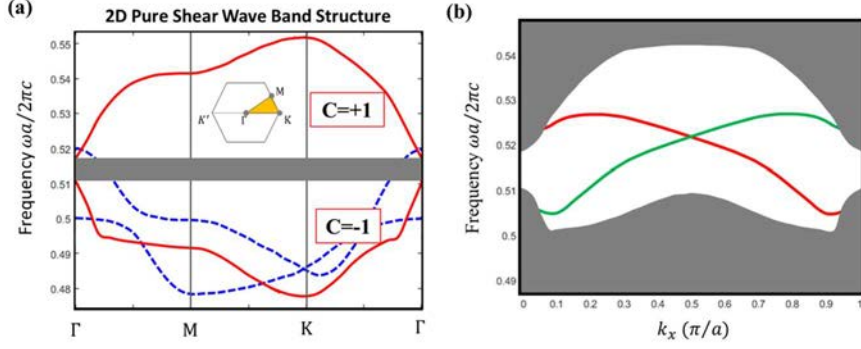


Fig. 4.2: Bulk band diagrams and gapless edge states (2D).(a) Band structure of pure shear mode in a triangular lattice with filling fraction f equals 0.64 ($r = 0.42a$). The shaded rectangle area highlights the topological band gap. Red solid and blue dashed lines correspond to the system with and without magnetic field $H_z = 100$ G, respectively. The Chern numbers are labelled for each band. (b) The solid line coloured in red and green expresses edge states in the upper and lower boundary, respectively. Other grey areas are made of a number of bulk bands. The material parameters: YAG ($\rho = 4550$ kg/m³, $c_l = 8600$ m/s, $c_t = 4960$ m/s), Epoxy ($\rho = 1190$ kg/m³, $c_l = 2830$ m/s, $c_t = 1160$ m/s).

Fig. 4.2 illustrates the band structure of pure shear waves. The PC consists of YAG rods ($\rho = 4550$ kg/m³, $c_l = 8600$ m/s, $c_t = 4960$ m/s) of radius $r = 0.42a$ embedded in epoxy background ($\rho = 1190$ kg/m³, $c_l = 2830$ m/s, $c_t = 1160$ m/s), in which a is the lattice constant. Others material parameters are $g_r = 1.759 \times 10^{11}$ s-T⁻¹, $b = 4.2 \times 10^5$ Pa, and $4\pi\mathbf{M}_s = 680$ G. Throughout the paper the frequency is normalised to a dimensionless one by multiplying a factor $2\pi a/c$, where c is the average shear velocity $\sqrt{\bar{c}_{44}/\bar{\rho}}$. Here the bar represents the average defined by $\bar{x} = fx_a + (1-f)x_b$, where f denotes the filling fraction. In accordance with these parameters, we numerically calculate the band structure of pure shear waves from Eq. (4-15) by COMSOL Multiphysics 5.1. As depicted in the Fig. 4.2a, the red solid and blue dashed lines represent the band diagrams with and without external magnetic fields. Note that even though there is no isolated Dirac point, a non-trivial bandgap is lifted via applying a uniform magnetic field $H_z = 100$ G. From Eq. (4-15) we calculate the values of c_{44} and c_{45} to be 78.8 GPa and 31.5 GPa, respectively. Due to the TR symmetry breaking, the degeneracies are lifted and a topologically non-trivial gap with a width $\Delta\omega = 0.06$ is created.

To verify the presence of nontrivial topological orders, we evaluate the Chern number for the n th band as $C_n = (1/2\pi) \int_{BZ} d^2\mathbf{k} \cdot \mathbf{\Omega}_n$, where $\mathbf{\Omega}_n = i \langle \nabla_{\mathbf{k}} u_z^n(\mathbf{k}) | \times | \nabla_{\mathbf{k}} u_z^n(\mathbf{k}) \rangle$ is the Berry curvature and the integration is carried throughout the first Brillouin zone. The Chern numbers for the two bands split by TR symmetry breaking are ± 1 (black number labelled in Fig. 4.2a). According to the principle of bulk-edge correspondence, a truncated PC exhibits topologically protected shear edge states in association with a net change of Chern number $\Delta C = 2$. We further investigate the existence of shear edge states appearing in a band gap. In Fig. 4.2b, the projected band structure for a 20×1 supercell is calculated, and two edge states can be seen within the bandgap. The boundary conditions of supercells are respectively set as periodic and fixed in the x and y directions.

In practical, the thickness of a slab must be finite and mixing between longitudinal and transverse waves is inevitable. To further verify the validity of the proposed model, in what follows the simulation for a practical system is implemented. With a finite thickness $h = 0.6a$, we assume a PC possessing geometry and material parameters as the same as the preceding 2D case. Although most of bands are mixed between the longitudinal and transverse states, two bands of pure shear waves emerge in the mixed states bandgap ranged from 0.22 to 0.55. In Fig. 4.3a, we observe that the Dirac point is located around the frequency 0.485 at K point. In Fig. 4.3b and c, it is clear to see that two degenerate eigenmodes are pure shear waves since the direction of vibrations is along z direction, which further proves the existence of Dirac points of pure shears in the bandgap of mixed waves. In Fig. 4.3c, the edge states can also be found within the bandgap between frequencies 0.476 and 0.484, where colours represent the same meaning as mentioned in pure shear models.

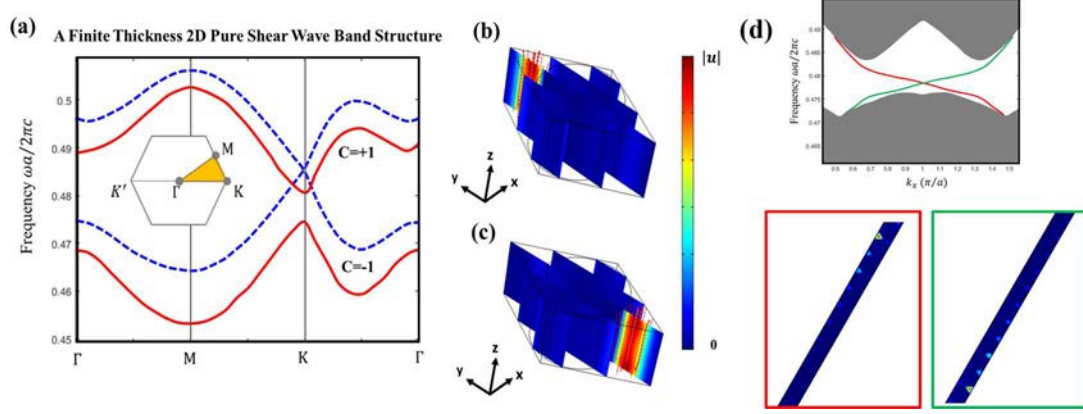


Fig. 4.3: Bulk band diagrams and gapless edge states (Finite Thickness). (a) Band structures with the same geometry as Fig. 4.2 except a finite thickness $h = 0.6a$. Red solid and blue dashed lines illustrate the system with and without applied magnetic field $H_z = 100$ G, respectively. (b-c), the arrows and the field slices at the Dirac degeneracy show the modes fairly vibrate along the z direction. (d) Projected band structure calculated by a 20×1 supercell arranged in triangular lattices. A set of unidirectional shear edge state (red and green curves) located between two bulk bands (blue regions). The edge eigenstates in the red and green boxes stand for the edge states at the top and bottom boundary, respectively.

In addition, one of the most essential features of topologically edge states is the robustness against disorders. In Fig. 4.4, we model a finite thickness 2D triangular lattice slab with an absorption layer at the bottom to demonstrate the field distributions of shear edge states. As shown in Fig. 4.4a-b, for a dc magnetic field applied in z and opposite directions, it is evident that the unidirectional shear wave modes excited by a z -oscillating source at the frequency of 0.489. Note that the chosen frequency is slightly higher than the gap range given by Fig. 4.4 due to the change of boundary condition in x axis. Our simulation shows that the centre of gap blue shifts but the gap width remains the same as before. Moreover, as shown in Fig. 4.4c, one can see the wave conformably bends around a sharp corner without being reflected or scattered, as protected by the nontrivial topology. Also, practically the influence of material loss should be considered. Here the damping factor Γ of YAG can be calculated from the linewidth ΔH given in [73]. By adding the dissipation term $\Gamma = 7.4 \times 10^{-2}$ Hz, there is no difference between lossless and lossy system even including the loss of YAG. To see how dissipation affects the edge states, we numerically increase the damping factor up to 7.4×10^4 Hz. In Fig. 4.4d, with this value of damping factor, the chiral edge states still exist, and their amplitude has no notable

change as the dissipation term Γ is sufficiently small in comparison with the operating frequency. Regarding the confinement of edge states, topological edge modes exponentially decay along the direction of truncated boundary and its decay rate depends on how large the gap is. In this case, with a comparatively small topological bandgap, the decay rate of shear waves is slower than the topological mechanical waves showing in the chapter 3, in spite of the fairly confined appearance of edge states shown in Fig. 4.4.

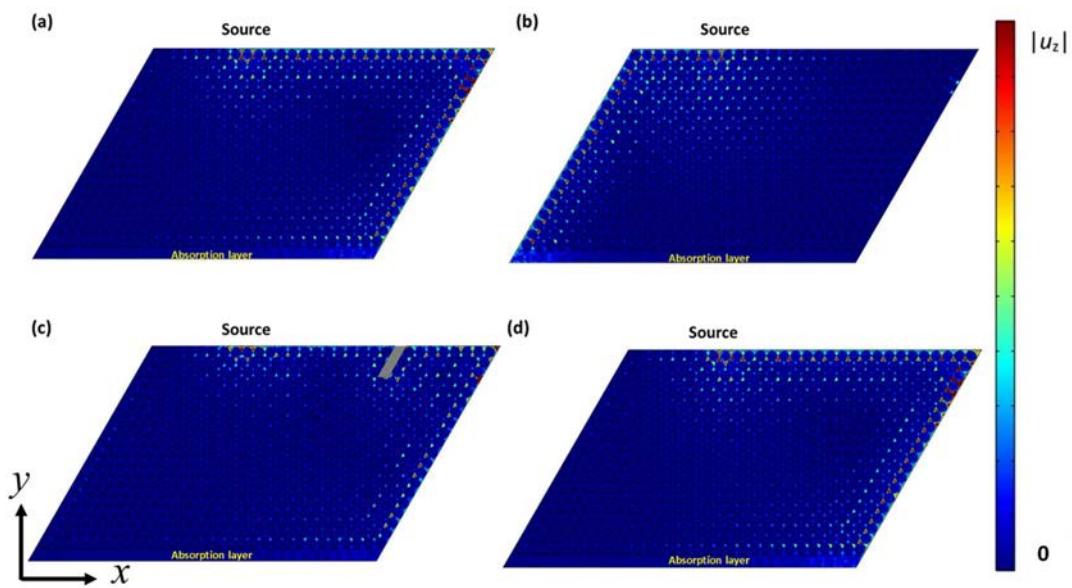


Fig. 4.4: One-way transport of shear modes. Unidirectional shear edge states in a finite PC with an applied dc magnetic field in (a) $+z$ and (b) $-z$ direction. A finite PC system surrounded by three fixed-constraint boundaries and an absorption layer at the bottom. (c) The robustness of shear edge states against a sharp corner. Topological protection ensures that no backscattering occurs in such system. All the edge states are excited by a point source at frequency 0.489. (d) The energy loss of YAG is considered in this field pattern. All the figures are calculated by using COMSOL.

4-3: Elastic Topological Insulators

In this section, we will investigate the topological nature in the in-plane mode of 2D elastic periodic composites. Based on (4-13a), by defining two effective spinors of elastic waves

$$u_{\pm} = (u_x \pm iu_y) / \sqrt{2}, \text{ Eq. (4-13a) is rewritten on this basis as}$$

$$\begin{aligned} \rho \ddot{u}_+ = & \nabla \cdot \left(\frac{\lambda + 3\mu}{2} \right) \nabla u_+ - i \left[\nabla \times \left(\frac{\lambda - \mu}{2} \right) \nabla u_+ \right]_z, \\ & + \nabla \cdot \left(\frac{\lambda + \mu}{2} \right) \hat{\sigma}_z \nabla u_- - i \left[\nabla \times \left(\frac{\lambda + \mu}{2} \right) \hat{\sigma}_z \nabla u_- \right]_z, \end{aligned} \quad (4-18a)$$

$$\begin{aligned} \rho \ddot{u}_- = & \nabla \cdot \left(\frac{\lambda + 3\mu}{2} \right) \nabla u_- + i \left[\nabla \times \left(\frac{\lambda - \mu}{2} \right) \nabla u_- \right]_z, \\ & + \nabla \cdot \left(\frac{\lambda + \mu}{2} \right) \hat{\sigma}_z \nabla u_+ + i \left[\nabla \times \left(\frac{\lambda + \mu}{2} \right) \hat{\sigma}_z \nabla u_+ \right]_z. \end{aligned} \quad (4-18b)$$

Now consider a particular case: $\lambda = -\mu$, Eq. (4-18) can be further simplified to

$$\rho \ddot{u}_+ = \nabla \cdot \mu \nabla u_+ + i \left[\nabla \times \mu \nabla u_+ \right]_z, \quad (4-19a)$$

$$\rho \ddot{u}_- = \nabla \cdot \mu \nabla u_- - i \left[\nabla \times \mu \nabla u_- \right]_z. \quad (4-19b)$$

The physical meaning of this assumption is that the equivalence of longitudinal and transverse sound velocity results in the duality between LT components, which can be one-to-one mapping the electromagnetic duality in photonic topological insulators [11]. Note that the criterion $\lambda = -\mu$ gives rise to infinite Poisson's ratio while the material is homogenous. Yet, with the aid of metamaterials, one can achieve such extreme condition within certain frequency region. Further studies for these matters will be introduced in the later content.

Here we consider a phononic meta-crystal with honeycomb lattice made of cylinders ($\rho_a = 19300 \text{ kg/m}^3$ and $\mu_a = 1.612 \times 10^{11} \text{ Pa}$) embedded in a background ($\rho_b = 2690 \text{ kg/m}^3$ and $\mu_b = 2.486 \times 10^{10} \text{ Pa}$). Through employing Bloch theorem, the displacement field expresses as $u_{\pm} = \sum_{\mathbf{G}} u_{\mathbf{G}}^{\pm} \exp[i(\mathbf{k} + \mathbf{G}) \cdot \mathbf{r}]$. Also, periodically arranged material parameters are decomposed by reciprocal lattice \mathbf{G} , which read $\mu = \sum_{\mathbf{G}} \mu_{\mathbf{G}} \exp(i\mathbf{G} \cdot \mathbf{r})$,

$$\rho = \sum_{\mathbf{G}} \rho_{\mathbf{G}} \exp(i\mathbf{G} \cdot \mathbf{r}) \text{ with } \mu_{\mathbf{G}} = \frac{1}{A} \int_{u.c.} \mu \exp(-i\mathbf{G} \cdot \mathbf{r}) d^2r, \rho_{\mathbf{G}} = \frac{1}{A} \int_{u.c.} \rho \exp(-i\mathbf{G} \cdot \mathbf{r}) d^2r. A$$

is the area of a unit cell and sub-index represents taking integration over the entire unit cell.

Substituting all the expressions above into Eq. (4-19), we obtain

$$\begin{aligned} \omega_{\mathbf{k}}^2 \rho_{\mathbf{G}-\mathbf{G}'} u_{\mathbf{G}'}^+ - \sum_{\mathbf{G}'} \mu_{\mathbf{G}-\mathbf{G}'} \left[(k_x + G_x)(k_x + G'_x) + (k_y + G_y)(k_y + G'_y) \right] u_{\mathbf{G}'}^+ \\ = i \sum_{\mathbf{G}'} \mu_{\mathbf{G}-\mathbf{G}'} \left[(k_x + G_x)(k_y + G'_y) - (k_y + G_y)(k_x + G'_x) \right] u_{\mathbf{G}'}^+ \end{aligned} \quad (4-20a)$$

$$\begin{aligned} \omega_{\mathbf{k}}^2 \rho_{\mathbf{G}-\mathbf{G}'} u_{\mathbf{G}'}^- - \sum_{\mathbf{G}'} \mu_{\mathbf{G}-\mathbf{G}'} \left[(k_x + G_x)(k_x + G'_x) + (k_y + G_y)(k_y + G'_y) \right] u_{\mathbf{G}'}^- \\ = -i \sum_{\mathbf{G}'} \mu_{\mathbf{G}-\mathbf{G}'} \left[(k_x + G_x)(k_y + G'_y) - (k_y + G_y)(k_x + G'_x) \right] u_{\mathbf{G}'}^- \end{aligned} \quad (4-20b)$$

To analyse the modes in the vicinity of the K and K' points, we truncate the plane waves basis for the first three reciprocal lattice components G_0 , G_1 , and G_2 , which are respectively equal to

$$G_0 = (0, 0), G_1 = \left(-\frac{3K}{2}, -\frac{\sqrt{3}K}{2} \right), G_2 = \left(-\frac{3K}{2}, \frac{\sqrt{3}K}{2} \right),$$

with $K = 4\pi/3a$. These three plane wave components give three equal-length reciprocal vectors originating from K point, and each of them rotates 120 degrees about the K point ($\mathbf{K} = [K, 0]$). For K' point ($\mathbf{K} = [-K, 0]$), three truncated reciprocal lattice vectors are

$$G_0 = (0, 0), G_1 = \left(\frac{3K}{2}, -\frac{\sqrt{3}K}{2} \right), G_2 = \left(\frac{3K}{2}, \frac{\sqrt{3}K}{2} \right),$$

Combining Eq. (4-20) for two spinors one obtains a general eigenvalue problem

$$\omega_{\mathbf{k}}^2 \begin{bmatrix} \gamma & \\ & \gamma \end{bmatrix} \begin{bmatrix} \mathbf{u}^+ \\ \mathbf{u}^- \end{bmatrix} = \begin{bmatrix} \boldsymbol{\alpha} + i\boldsymbol{\beta} & \\ & \boldsymbol{\alpha} - i\boldsymbol{\beta} \end{bmatrix} \begin{bmatrix} \mathbf{u}^+ \\ \mathbf{u}^- \end{bmatrix} \quad (4-21)$$

where $\mathbf{u}^{\pm} = [u_0^{\pm}, u_1^{\pm}, u_2^{\pm}]^T$. Around K point we expand Eq. (4-21) to first-order perturbation

$k_x = K + \delta k_x$ and $k_y = \delta k_y$. After neglecting second-order and higher small quantities, we have

$$\boldsymbol{\gamma} = \begin{bmatrix} \rho_0 & \rho_1 & \rho_1 \\ \rho_1 & \rho_0 & \rho_1 \\ \rho_1 & \rho_1 & \rho_0 \end{bmatrix}, \quad (4-22a)$$

$$\begin{aligned} \boldsymbol{\alpha} = & K^2 \begin{bmatrix} \mu_0 & -\frac{1}{2}\mu_1 & -\frac{1}{2}\mu_1 \\ -\frac{1}{2}\mu_1 & \mu_0 & -\frac{1}{2}\mu_1 \\ -\frac{1}{2}\mu_1 & -\frac{1}{2}\mu_1 & \mu_0 \end{bmatrix} + K\delta k_x \begin{bmatrix} 2\mu_0 & \frac{1}{2}\mu_1 & \frac{1}{2}\mu_1 \\ \frac{1}{2}\mu_1 & -\mu_0 & -\mu_1 \\ \frac{1}{2}\mu_1 & -\mu_1 & -\mu_0 \end{bmatrix} \\ & + K\delta k_y \begin{bmatrix} 0 & -\frac{\sqrt{3}}{2}\mu_1 & \frac{\sqrt{3}}{2}\mu_1 \\ -\frac{\sqrt{3}}{2}\mu_1 & -\sqrt{3}\mu_0 & 0 \\ \frac{\sqrt{3}}{2}\mu_1 & 0 & \sqrt{3}\mu_0 \end{bmatrix}, \quad (4-22b) \end{aligned}$$

$$\begin{aligned} \boldsymbol{\beta} = & \frac{\sqrt{3}}{2}K^2\mu_1 \begin{bmatrix} & -1 & 1 \\ 1 & & -1 \\ -1 & 1 & \end{bmatrix} + \sqrt{3}K\delta k_x\mu_1 \begin{bmatrix} & -1/2 & 1/2 \\ 1/2 & & 1 \\ -1/2 & -1 & \end{bmatrix}, \quad (4-22c) \\ & + \frac{3}{2}K\delta k_y\mu_1 \begin{bmatrix} & 1 & 1 \\ -1 & & \\ -1 & & \end{bmatrix} \end{aligned}$$

Applying the unitary transformation $[\hat{U}, \hat{\mathbf{0}}; \hat{\mathbf{0}}, \hat{U}]$ with $[1, 1, 1; 1, \eta^2, \eta; 1, \eta, \eta^2]/\sqrt{3}$ and $\eta = \exp(i2\pi/3)$, further simplified expressions read

$$\tilde{\boldsymbol{\gamma}} = (\rho_0 + \rho_1)\mathbf{I}_{3 \times 3}, \quad (4-23a)$$

$$\begin{aligned} \tilde{\boldsymbol{\beta}} = & \frac{-i3}{2}K^2\mu_1 \begin{bmatrix} & & \\ & 1 & \\ & & -1 \end{bmatrix} + \frac{i3\sqrt{3}}{2}K\delta k_x\mu_1 \begin{bmatrix} & -1 & 1 \\ -1 & & \\ 1 & & \end{bmatrix}, \quad (4-23b) \\ & + \frac{9}{4}K\delta k_y\mu_1 \begin{bmatrix} & & \\ -1 & & -1 \\ 1 & & \end{bmatrix} \end{aligned}$$

$$\begin{aligned}
\tilde{\mathbf{a}} = K^2 & \begin{bmatrix} \mu_0 - \mu_1 & & & \\ & \mu_0 + \frac{1}{2}\mu_1 & & \\ & & \mu_0 + \frac{1}{2}\mu_1 & \\ & & & \mu_0 - \mu_1 \end{bmatrix} + K\delta k_x \begin{bmatrix} & \mu_0 + \frac{1}{2}\mu_1 & \mu_0 + \frac{1}{2}\mu_1 & \\ & \mu_0 + \frac{1}{2}\mu_1 & & \mu_0 - \mu_1 \\ \mu_0 + \frac{1}{2}\mu_1 & & & \\ \mu_0 + \frac{1}{2}\mu_1 & \mu_0 - \mu_1 & & \end{bmatrix} \\
& + iK\delta k_y \begin{bmatrix} & & -\left(\mu_0 + \frac{1}{2}\mu_1\right) & \left(\mu_0 + \frac{1}{2}\mu_1\right) \\ \left(\mu_0 + \frac{1}{2}\mu_1\right) & & & -(\mu_0 - \mu_1) \\ -\left(\mu_0 + \frac{1}{2}\mu_1\right) & & & \\ & -\left(\mu_0 + \frac{1}{2}\mu_1\right) & (\mu_0 - \mu_1) & \end{bmatrix} \quad .(4-23c)
\end{aligned}$$

where $\tilde{\mathbf{O}} = \hat{U}\mathbf{O}\hat{U}^\dagger$. Finally, by eliminating the two singlets and keeping the two doublets, two Dirac Hamiltonian associated with an effective intrinsic SOC term near the K point are given by

$$\omega_{\text{PnTI}} \begin{bmatrix} \mathbf{u}_d^+ \\ \mathbf{u}_d^- \end{bmatrix} = \begin{bmatrix} v_D (\delta k_x \sigma_x + \delta k_y \sigma_y) + \zeta \sigma_z & \\ & v_D (\delta k_x \sigma_x + \delta k_y \sigma_y) - \zeta \sigma_z \end{bmatrix} \begin{bmatrix} \mathbf{u}_d^+ \\ \mathbf{u}_d^- \end{bmatrix} \quad (4-24a)$$

In the same manner, for K' point Dirac Hamiltonian reads

$$\omega_{\text{PnTI}} \begin{bmatrix} \mathbf{u}_d^+ \\ \mathbf{u}_d^- \end{bmatrix} = \begin{bmatrix} v_D (-\delta k_x \sigma_x + \delta k_y \sigma_y) - \zeta \sigma_z & \\ & v_D (-\delta k_x \sigma_x + \delta k_y \sigma_y) + \zeta \sigma_z \end{bmatrix} \begin{bmatrix} \mathbf{u}_d^+ \\ \mathbf{u}_d^- \end{bmatrix} \quad (4-24b)$$

where

$$\omega_{\text{PnTI}} = (\rho_0 + \rho_1) \Omega(K) \frac{\omega^2 - \Omega^2(K)}{K^2}$$

$$\Omega(K) = K \sqrt{[(\mu_0 + \mu_1/2)/(\rho_0 + \rho_1)]}$$

$$v_D = (\mu_0 - \mu_1) \Omega(K) / K$$

$$\zeta = 3\Omega(K)\mu_1/2$$

Eq. (4-24) together presents a 4×4 low-energy effective Hamiltonian

$$\hat{H} = v_D (\tau_z \delta k_x \sigma_x + \delta k_y \sigma_y) + \zeta \tau_z s_z \sigma_z, \quad (4-25)$$

where τ_z and s_z denotes the valley and spin index, respectively. Eq. (4-25) is equivalent to the KM model for 2D topological insulators so that the proposed system can be regarded as the elastic counterpart of it.

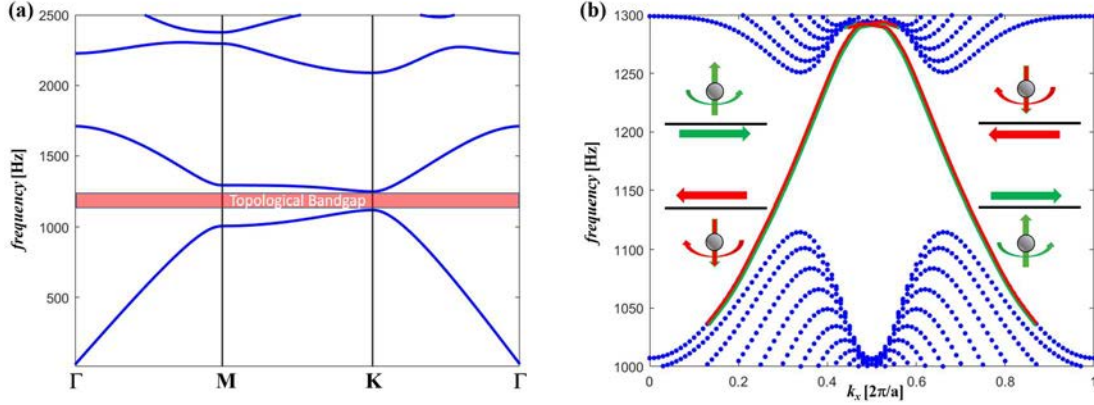


Fig. 4.5: Topologically non-trivial bandgap and gapless edge states. (a) Band diagram of elastic topological insulators consisting of special inclusions ($\rho_a = 19300 \text{ kg/m}^3$ and $\mu_a = 1.612 \times 10^{11} \text{ Pa}$) embedded in a background ($\rho_b = 2690 \text{ kg/m}^3$ and $\mu_b = 2.486 \times 10^{10} \text{ Pa}$). Every band is doubly degenerate due to longitudinal-transverse (LT) duality. A red shaded region is highlighted for the topological non-trivial bandgap. (b) Four edge states within the topological band gap. Each pair represents topologically one-way transports for a spin pair. Both figures are numerically calculated by using COMSOL multiphysics.

According to the given material parameters, in Fig. 4.5a the band structure of the phononic meta-crystal for two distinct conditions are investigated. If we force the second term of the Eq. (4-19) vanishes, the band diagram plotted by solid lines exhibit a Dirac degeneracy around K(K') points. As stated in chapter three, a Dirac point carries a topological charge as it is a singular point of Berry curvatures. With the intrinsic SOC term, which is the second term of Eq. (4-19), a topological non-trivial bandgap is lifted between the 2nd and 3rd band. Exploiting FEM numerical calculation performed by COMSOL 5.1a, Fig. 4.5b demonstrates the gapless edge states of two chiral phonons (spinors) for a 30×1 supercell. The boundary

condition follows Dirichlet condition on truncated edge and Floquet-Bloch condition along x direction, respectively. Although phononic systems are bosonic, which in general does not obey Kramers theorem, in here Kramers theorem can be applied such that linear combination of two phonon polarisations creates an effectively spinful system. Therefore, two chiral edge states in Fig. 4.5b must be degenerate at TRIMs as formerly discussed in chapter two.

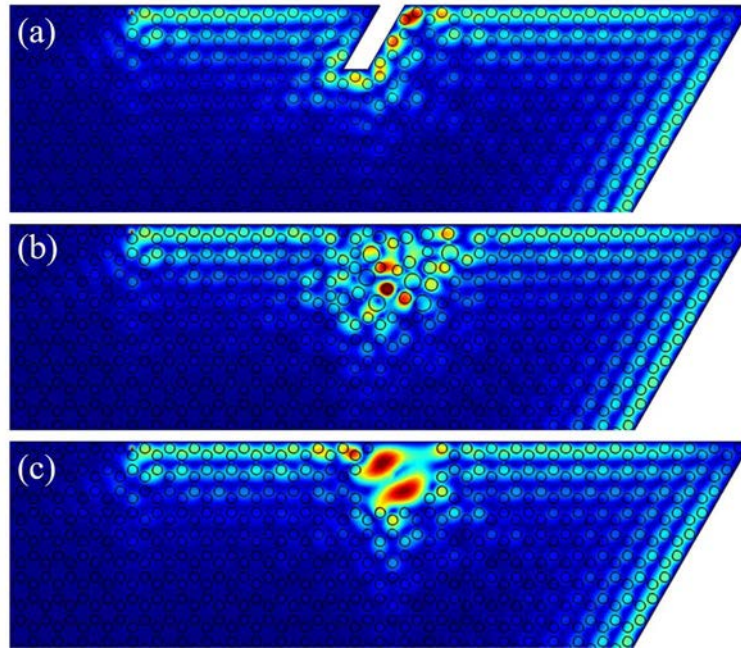


Fig. 4.6: TR Symmetry-protected edge states. Three kinds of defects calculated by COMSOL multiphysics: (a) a block for a sharp corner, (b) random distribution of geometry, and (c) a cavity by removing an area of cylinders. For all type of disorders, topological protection guarantees the backscattering-immune propagation along the boundary. Note that here only spin-up polarised source is used.

To confirm the robustness against disorders, in Fig. 4.6 we plot several cases that exhibit the reflection-free unidirectional spin wave propagation guaranteed by TR symmetry in the system. Here we consider spin-up cases only because, for spin-down, the phenomena are the same except the propagating direction. From Fig. 4.6a-c, three types of defects are numerically demonstrated. In Fig. 4.6a, from a point source to right spin waves propagate around a sharp corner created by a fixed block without any backscattering. In Fig. 4.6b, by introducing randomness to the distribution of cylinders, we construct an area of disorders but still, spin waves bypass this random area without any occurrence of reflection. At last, we

remove a few cylinders to form a cavity. Generally, as operating frequency is chosen within the bandgap, localised modes arise like the cavity-phononic crystal we perform in Chapter three. However, due to the topological protection, spin waves circling around the cavity generate no cavity mode. All three type defects show that symmetry-protected edge states take place as long as TR symmetry retains.

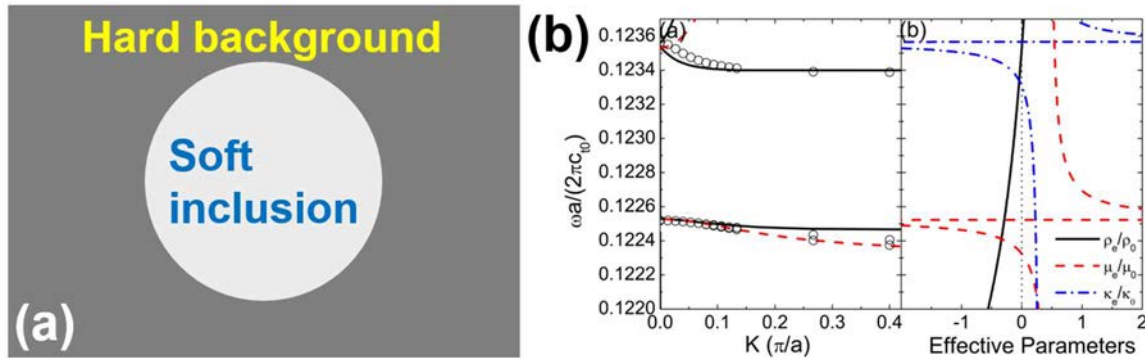


Fig. 4.7: Elastic metamaterials.(a) A schematic draw for elastic metamaterials. Within a unit cell, a soft inclusion embedded in the hard background creates an effective dispersive medium. (b) The plot of low-frequency band diagram and effective material parameters show a resonance feature of elastic metamaterials. [75]

Despite the exotic properties described above, to fabricate elastic solids with criterion $\lambda = -\mu$ or zero bulk modulus in 2D, it takes extra attention since, physically, such material cannot be found in nature. Yet, artificial composites called metamaterials provide the chance of accomplishing negative elastic moduli. The design of elastic metamaterials has been revealed in this reference [75]. Here a brief discussion is given. As shown in Fig. 4.7a, consider a soft inclusion, such as water, rubber, or acrylics, embedded in a hard background, normally, metals. Under long-wavelength limit, this composite is equivalent to a spring-mass network with characteristic frequencies, which can be considered as a multi-pole dispersive material that leads to zero bulk modulus. In Fig. 4.7b, effectively we can have zero bulk modulus at a certain frequency that, in principle, makes the elastic topological insulators possible. Nevertheless, there is a flaw in the previous band diagram calculation. For dispersive media,

direct FEM emulation by COMSOL needs to be corrected because formally the wave equation cannot be discretised as an eigenvalue problem of frequency. To clarify this part, an alternative numerical calculation of band structure proposed in ref. [76] will be implemented. Additionally, since the LT duality is no longer valid for any frequency point, Z_2 topological index must be further calculated to verify the occurrence of topological nature in the future.

4-4: Chapter Summary

Throughout this chapter, firstly we demonstrated the emergence of topological shear wave in a 2D PC with finite thickness. For such elastic composites, the mixed modes, in general, are coupled with the vibration in z direction. However, by choosing proper geometry and material parameters, we obtained the Dirac degeneracies of pure shear waves found in a gap of mixed modes, leading to a topologically non-trivial gap as the uniform magnetic field is applied. Since our proposed system is made by two realistic materials, it is feasible to experimentally observe these topological shear edge states. In our design, the operating frequency of 0.489 corresponds to a PC lattice constant of about $6.67 \mu\text{m}$, which is feasible to fabricate by using current nanofabrication technology.

In the second part, we discussed the topological nature of in-plane elastic waves. Assuming a zero-index bulk modulus, the elastic version of topological insulators arises from the LT duality. Our deduction analytically proved that the effective KM model can be achieved near the Brillouin zone vertices K and K' . Numerically, the band diagram of a unit cell and a 30×1 supercell were presented for the verification of topological bandgap and gapless edge states in between. To examine its topological protection properties, three kinds of defects were applied but none of them can lead to any reflection so long as the TR symmetry is preserved. Due to the use of zero-index bulk modulus, we introduced metamaterials to achieve it at certain

frequency region. Yet as a dispersive case, the numerical calculation of band structure should be corrected, for which we aim to investigate in the future.

Chapter 5 Rotation Induced PT Symmetric Acoustics

As mentioned in Sec. 2-4, non-Hermitian physics with PT symmetry possesses many intriguing phenomena. In this chapter, distinguished from the conventional gain-loss combination, we propose a novel approach to realise PT symmetric physics via the rotations. In what follows, we prove that a metamaterial consisting of spinning cylinders leads to interesting type of dispersion, i.e. folded band, in extremely low-frequency region. Within these folded bands, there exist complex solutions representing the occurrence of PT broken phase. In addition, at every PT phase transition point, a set of exceptional points forms rings in 3D band diagram that generate an extraordinary effect called pairs of exceptional rings. In what follows, the content in Sec. 5-3 is related to Part E in Table II.

5-1: Introduction

As previously stated, the acoustic waves can be regarded as a special case of elasticity. Yet, in comparison with elastic waves, sonic waves are closer to our daily life so that the related studies and applications are ubiquitous in practical. In this section, a brief introduction of sound is presented via the perspectives of fluid mechanics [77]. In fluid mechanics, considering an incompressible fluid, the continuity equation $\partial_t \rho + \rho \nabla \cdot \mathbf{v} = 0$ must hold in accordance with conservation of mass. Also, based on Newton's second law, we have the momentum (Euler) equation $\partial_t \mathbf{v} + (\mathbf{v} \cdot \nabla) \mathbf{v} = -\rho^{-1} \nabla p$.

With regard to the sound waves, it is a kind of the alternative and small volume change in fluid. Therefore, the additions of small-quantity perturbations on incompressible fluids lead

to the governed equation of acoustic waves. Three variables are expressed as $\mathbf{v} = \mathbf{v}_0 + \mathbf{v}'$, $p = p_0 + p'$ and $\rho = \rho_0 + \rho'$. Substituting them into the continuity and the momentum equation, by neglecting second-order small magnitudes, we obtain

$$\partial_t \rho' + \rho_0 \nabla \cdot \mathbf{v}' = 0,$$

$$\partial_t \mathbf{v}' + \rho_0^{-1} \nabla p' = 0.$$

As the motions in ideal fluid is an adiabatic process, the relation $p' = c_0^2 \rho'$ connecting pressure, density and fluid velocity holds. Combining two equations above with the identity $\nabla \cdot \mathbf{v}' = c_0^{-2} \partial_t p'$, the pressure wave equation yields

$$\frac{1}{\rho_0 c_0^2} \partial_t^2 p' = \nabla \cdot \frac{1}{\rho_0} \nabla p',$$

where the factor $\rho_0 c_0^2$ is usually called “bulk modulus” with the notation B_0 . The above pressure wave equation shows the identical mathematical expression as 2D shear waves stated in the previous chapter, as well as the TE(TM) modes in electromagnetism while replacing ϵ (μ) with ρ_0 and μ (ϵ) with B_0^{-1} . Consequently, the concepts of metamaterials for electromagnetic waves can be intuitively extended to sound waves by the proper structure engineering.

On the other hand, over the past decades, metamaterials, which could manipulate waves by the design of certain structures, have achieved many novel phenomena such as double negative material indices [78], subwavelength imaging [79], invisibility cloaking [80], and classical analogue of electromagnetically induced transparency [81]. Specifically, for sonic waves modulation, there are several ways to implement acoustic metamaterials. To realise the

negative bulk modulus, the structures is made of periodically arranged Helmholtz resonators [82]. In addition, negative mass density is observed in a composite is composed of heavy metal beads coated by soft rubbers [83-84]. Lastly, A set of silicone rubber spheres suspended in water has been theoretically proposed that can bring about double negative material indices [85]. In addition to preceding methods, Censor et. al. [86] pointed out the sound waves is scattered even though the material of spinning inclusion and background are identical. This result implies that rotation will transform the material properties into the one distinguished from its origin. Inspired by that, in the subsequent contents, we will prove non-dispersive media could be changed into dispersive ones while the scatterer rotates. This rotation-induced dispersion enables us to accomplish acoustic metamaterials without fabricating any complex structure.

In this chapter, we demonstrate pairs of ERs in a PT symmetric acoustic metamaterial distinguished from the conventional gain-loss combination. To achieve it, we introduce a periodic array of spinning cylinders in a water matrix. Induced by the rotation, effective dispersive media arise under long-wavelength approximation. Around the magnitude of angular velocity, we show that the Hamiltonian of proposed model exhibits two ERs in the vicinity of Γ point. Most interestingly, the imaginary term of each pair of ERs forms a novel torus in momentum space. To examine the order of EPs, phase rigidity is applied and the results present a ring of 1/2 order singularities around every \mathbf{k} direction. We further demonstrate an additional pair of ERs, which shares the same mechanism as others, at higher frequency region.

5-2: Rotation Induced Dispersion

We begin by considering a 2D periodic composite made by an array of parallel, inviscid fluid cylinders immersed in water background ($\rho_0 = 1000 \text{ kg/m}^3$, $c_0 = 1490 \text{ m/s}$). The lattice constant

$a = 0.1$ m and the radius of cylinders $r_s = 0.15a$. As indicated in Fig. 5.1a, each cylinder rotates about its symmetric z axis in a constant angular velocity $W = 3000$ rad/s. Although it is difficult to implement, particularly we assume that filling fluid is also water to demonstrate the influence between dispersion and rotation. In the later part, a realistic case will be discussed. Fig. 5.1 depicts the schematic plot of a rotation-induced acoustic metamaterial. Nevertheless, whereas Fig. 5.1a illustrates a square lattice of cylinders, the lattice type is insignificant because only the homogenised bulk material is implemented. In polar coordinates, the pressure acoustic wave equation inside the inclusions with a constantly rotating speed W is given by [86]

$$\partial_r^2 p + r^{-1} \partial_r p - r^{-2} m^2 p + \lambda_m^2 p = 0, \quad (5-1)$$

where p is the pressure wave, m is the angular index, and the rotating wavevector $\lambda_m^2 = -(4W^2 + M^2)c^{-2}$. The frequency correction $M = -i(\omega - mW)$ is due to the rotational Doppler effect [87] that causes frequency shifts of waves propagating from static to rotating media. The solutions of (5-1) generate a complete set composed of Bessel and Hankel functions that enable the analysis by employing multiple scattering theory* (MST). To match the boundary conditions, we further calculate the radial and azimuthal displacement u_r and u_θ denoted as

$$u_r = \left[(2W^2 - M^2) \partial_r p - 3imMWp/r \right] / \left[(M^2 + 4W^2)(M^2 + W^2) \right], \quad (5-2a)$$

$$u_\theta = \left[3MW \partial_r p + im(2\Omega^2 - M^2)p/r \right] / \left[(M^2 + 4W^2)(M^2 + W^2) \right]. \quad (5-2b)$$

* Multiple scattering theory is the mathematical algorithm for calculating wave propagation via a collection of waves scattered by many objects. It is applicable to several physical systems, such as porous media in acoustics, sunlight scattered by many water droplets (cloud) in the sky, or high-frequency electromagnetic waves scattering from a solid crystal.

After applying boundary conditions $p_{bac} = p_{inc}$ as well as $-\nabla p_{bac}/\rho_0\omega^2 = u_r$, the Mie scattering coefficients is

$$D_m = -\frac{\lambda_m \rho_0 R_m(\lambda_m r_s) J_m(k_0 r_s) - k_0 \rho_s J_m(\lambda_m r_s) J'_m(k_0 r_s)}{\lambda_m \rho_0 R_m(\lambda_m r_s) H_m(k_0 r_s) - k_0 \rho_s J_m(\lambda_m r_s) H'_m(k_0 r_s)}, \quad (5-3)$$

where,

$$R_m(\lambda_m r_s) = \frac{\omega^2 \left\{ (2W^2 - M^2) J'_m(\lambda_m r_s) - 3imMW \left[J_m(\lambda_m r_s) / (\lambda_m r_s) \right] \right\}}{(4W^2 + M^2)(W^2 + M^2)}. \quad (5-4)$$

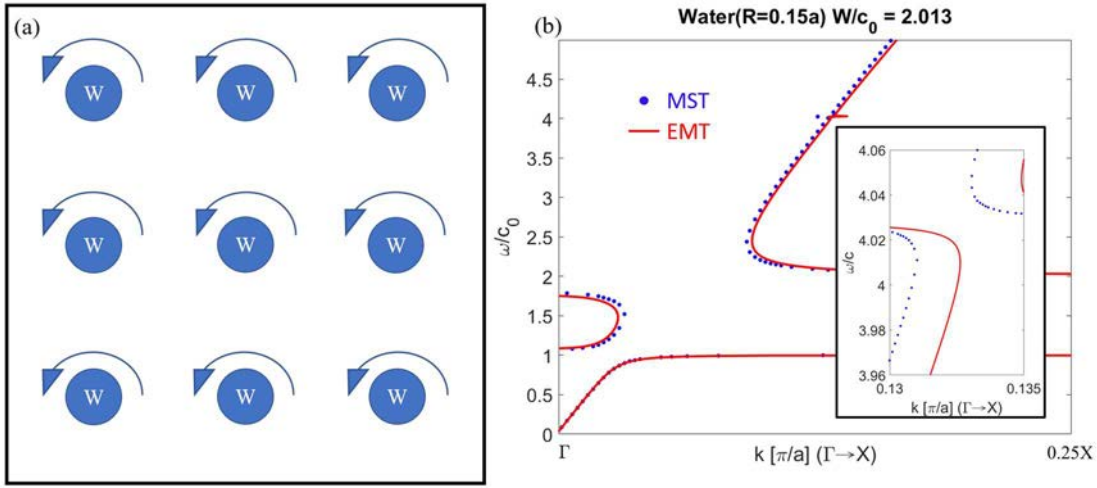


Fig. 5.1: A schematic plot and low-frequency dispersion. (a) A 2D periodic structure consisting of a water-cylinder array in water background ($\rho = 1000 \text{ kg/m}^3$ and $c = 1490 \text{ m/s}$). Each cylinder is parallel to z axis with a constant angular velocity W . (b) The band diagrams for acoustic metamaterials by using MST and EMT. Both results fairly match each other. Second and third band are folded within the frequency region $W/c_0 = [1, 3]$, and $[3.99, 4.06]$ as illustrated in the inset.

As depicted in Fig. 5.1b, by using both MST as well as the effective material theory (EMT) [88], we plot the band diagrams for acoustic metamaterials via scanning the real frequencies and wavevectors. When the eigenfrequency is much higher than angular frequency, it shows a scatterer-free band structure which is the same as the case without rotation. However, as the eigenfrequencies are approaching the angular frequency W , around the long-wavelength region the dispersion relation dramatically changes into several folding and resonance bands owing to

the gain resulted from the centrifugal force. Especially the turning points between these folding bands, we will show that there exist some complex solutions by constructing an effective Hamiltonian around the low-frequency area.

We further deduce effective material indices inside the scatterers and the method of homogenisation. To calculate the effective density and bulk modulus, a necessary term $D_m/(1+D_m)$ is

$$\frac{D_m}{1+D_m} = \frac{\frac{\lambda_m \rho_0}{k_0 \rho_s} \left[\frac{R_m(\lambda_m r_s)}{J_m(\lambda_m r_s)} \right] \left[\frac{J_m(k_0 r_s)}{J'_m(k_0 r_s)} \right] - 1}{\frac{\lambda_m \rho_0}{k_0 \rho_s} \left[\frac{R_m(\lambda_m r_s)}{J_m(\lambda_m r_s)} \right] \left[\frac{J_m(k_0 r_s)}{J'_m(k_0 r_s)} \right] \frac{Y_m(k_0 r_s)}{iJ_m(k_0 r_s)} - \frac{Y'_m(k_0 r_s)}{iJ'_m(k_0 r_s)}}}. \quad (5-5)$$

With Eq. (5-5), we can derive the effective bulk modulus and the mass density in the subsequent contents. Firstly, for effective bulk modulus, we only need to take the angular index $m = 0$ into account. Based on the EMT [88], the effective bulk modulus is given by

$$\frac{B_e^{-1} + 2B_0^{-1} \frac{J'_0(k_0 r_0)}{k_0 r_0 J_0(k_0 r_0)}}{B_e^{-1} + 2B_0^{-1} \frac{Y'_0(k_0 r_0)}{k_0 r_0 Y_0(k_0 r_0)}} = \frac{Y_0(k_0 r_0)}{iJ_0(k_0 r_0)} \left(\frac{D_0}{1+D_0} \right). \quad (5-6)$$

Although Eq. (5-6) has given the analytic form of effective bulk modulus, we do further approximation under the condition $k_0 r_s < k_0 r_0 \ll 1$ so as to clarify the influence of the rotation in material properties. Focusing on the R.H.S. of Eq. (5-6), it can be rewritten as

$$R.H.S. = \frac{\frac{\lambda_0 \rho_0}{k_0 \rho_s} \left[\frac{R_0(\lambda_0 r_s)}{J_0(\lambda_0 r_s)} \right] \left[\frac{J_0(k_0 r_s)}{J'_0(k_0 r_s)} \right] - 1}{\frac{\lambda_0 \rho_0}{k_0 \rho_s} \left[\frac{R_0(\lambda_0 r_s)}{J_0(\lambda_0 r_s)} \right] \left[\frac{J_0(k_0 r_s)}{J'_0(k_0 r_s)} \right] \frac{Y_0(k_0 r_s)/Y_0(k_0 r_0)}{J_0(k_0 r_s)/J_0(k_0 r_0)} - \frac{Y'_0(k_0 r_s)/Y_0(k_0 r_0)}{J'_0(k_0 r_s)/J_0(k_0 r_0)}}}. \quad (5-7)$$

As long as the approximate condition $k_0 r_s < k_0 r_0 \ll 1$ holds, we have

$$\begin{aligned}
J_0(k_0 r_s)/J'_0(k_0 r_s) &\approx -\frac{2}{k_0 r_s} \\
Y_0(k_0 r_s)/Y_0(k_0 r_0) &\approx J_0(k_0 r_s)/J_0(k_0 r_0) \approx 1. \\
\frac{Y'_0(k_0 r_s)/Y_0(k_0 r_0)}{J'_0(k_0 r_s)/J_0(k_0 r_0)} &\approx -\frac{2}{k_0^2 r_s^2 \ln(k_0 r_0)}
\end{aligned}$$

Also, while $k_0 r_0, k_0 r_s \rightarrow 0, k_0^2 r_s^2 \ln(k_0 r_0) \rightarrow 0$. It causes that the denominator is dominated by the

term $\frac{2}{k_0^2 r_s^2 \ln(k_0 r_0)}$ so that the R.H.S. can be approximately expressed as

$$R.H.S. = \frac{\frac{\lambda_0 \rho_0}{k_0 \rho_s} \left[\frac{R_0(\lambda_0 r_s)}{J_0(\lambda_0 r_s)} \right] \left[-\frac{2}{k_0 r_s} \right] - 1}{\frac{2}{k_0^2 r_s^2 \ln(k_0 r_0)}}. \quad (5-8)$$

In the same manner, we will have the expression of L.H.S.

$$L.H.S. = \frac{B_e^{-1} - B_0^{-1}}{B_0^{-1} \frac{2}{k_0^2 r_0^2 \ln(k_0 r_0)}}. \quad (5-9)$$

Combining with Eq. (5-8) and (5-9), a clearer form of effective bulk modulus is

$$\frac{B_e^{-1} - B_0^{-1}}{B_0^{-1}} = f \frac{B_s^{-1} - B_0^{-1}}{B_0^{-1}}, \quad (5-10)$$

where $f = (r_s / r_0)^2$ is the filling ratio and the bulk modulus inside every scatterer denotes

$$\frac{1}{B_s} = \frac{\lambda_0^2}{\omega^2 \rho_s} \left[\frac{R_0(\lambda_0 r_s)}{J_0(\lambda_0 r_s)} \right] \left[-\frac{2}{\lambda_0 r_s} \right]. \quad (5-11)$$

With the aid of Eq. (5-10) and (5-11), the influence of rotation is now separated from the background. Note that Eq. (5-11) is deduced under the condition $k_0 r_s \ll 1$. It means $k_0 \ll 1 / r_s$

or $k_0 \ll 10$ as $r_s = 0.15a$ and $a = 0.1$. Therefore, a reasonable choice of a frequency region could be $|k_0| < 3$ and this region will be considered in the subsequent contents.

Before we start to calculate its expression, it is helpful to look the value of function

$\frac{J'_0(\lambda_0 r_s)}{\lambda_0 r_s J_0(\lambda_0 r_s)}$. In the Fig. 5.2a, it is evident to see that, in the region $|k_0| < 3$, the value nearly equals -0.5.

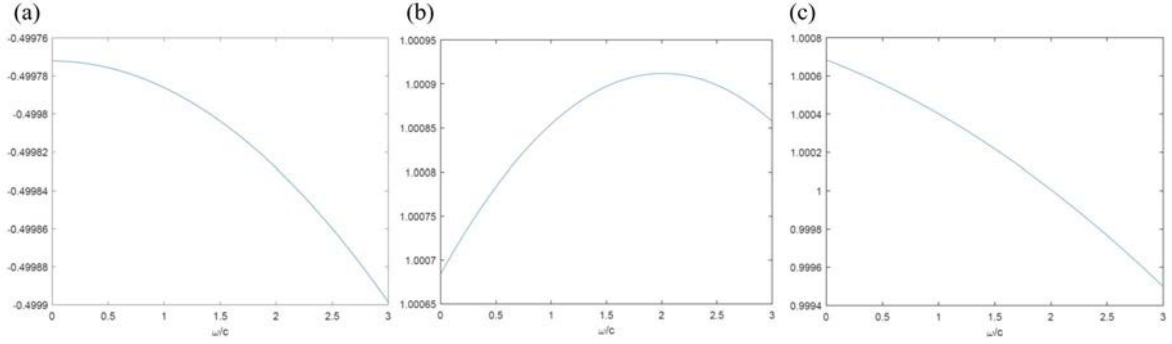


Fig. 5.2: The approximate values:The numerical calculation between $\omega/c = [0, 3]$ for the magnitude of (a) $J'_0(\lambda_0 r_s)/[\lambda_0 r_s J_0(\lambda_0 r_s)]$, (b) $[\lambda_1 r_s J'_1(\lambda_1 r_s)]/J_1(\lambda_1 r_s)$, and (c) $[\lambda_{-1} r_s J'_{-1}(\lambda_{-1} r_s)]/J_{-1}(\lambda_{-1} r_s)$.

Thus, Eq. (5-11) is simplified to

$$\begin{aligned} \frac{1}{B_s} &= \frac{\lambda_0^2}{\omega^2 \rho_s} \left[\frac{R_0(\lambda_0 r_s)}{J_0(\lambda_0 r_s)} \right] \left[-\frac{2}{\lambda_0 r_s} \right] \\ &= \frac{\omega^2}{\omega^2 \cdot (4W^2 - \omega^2) \cdot (W^2 - \omega^2)} \left[(2W^2 + \omega^2) \frac{J'_0(\lambda_0 r_s)}{\lambda_0 r_s J_0(\lambda_0 r_s)} \right] \cdot \left[\frac{2(4W^2 - \omega^2)}{\rho_s c_s^2} \right] \\ &\approx \frac{(2W^2 + \omega^2)}{(\omega^2 - W^2) \rho_s c_s^2} = \frac{1}{\rho_s c_s^2} \left(1 + \frac{3W^2}{\omega^2 - W^2} \right) \end{aligned}$$

Consequently, we can conclude that the effective bulk modulus for each scatterer has a resonant form given by

$$\frac{1}{B_s} = \frac{1}{\rho_s c_s^2} \left(1 + \frac{3W^2}{\omega^2 - W^2} \right) \quad (5-12)$$

Additionally, by taking only the angular index $m = 1$ into account. The effective mass density can be denoted as

$$\frac{\rho_e^+ - \rho_0 \frac{J_1(k_0 r_0)}{k_0 r_0 J_1'(k_0 r_0)}}{\rho_e^+ - \rho_0 \frac{Y_1(k_0 r_0)}{k_0 r_0 Y_1'(k_0 r_0)}} = \frac{Y_1'(k_0 r_0)}{i J_1'(k_0 r_0)} \left(\frac{D_1}{1 + D_1} \right). \quad (5-13)$$

In the same manner, one can do further approximation $k_0 r_0, k_0 r_s \ll 1$ and the R.H.S. of Eq. (5-13) is expressed as

$$\text{R.H.S.} = \frac{\frac{\lambda_1 \rho_0}{k_0 \rho_s} \left[\frac{R_1(\lambda_1 r_s)}{J_1(\lambda_1 r_s)} \right] \left[\frac{J_1(k_0 r_s)}{J_1'(k_0 r_s)} \right] - 1}{\frac{\lambda_1 \rho_0}{k_0 \rho_s} \left[\frac{R_1(\lambda_1 r_s)}{J_1(\lambda_1 r_s)} \right] \left[\frac{J_1(k_0 r_s)}{J_1'(k_0 r_s)} \right] \frac{Y_1(k_0 r_s)/Y_1'(k_0 r_0)}{J_1(k_0 r_s)/J_1'(k_0 r_0)} - \frac{Y_1'(k_0 r_s)/Y_1'(k_0 r_0)}{J_1'(k_0 r_s)/J_1'(k_0 r_0)}}. \quad (5-14)$$

Similarly, the approximate condition $k_0 r_0, k_0 r_s \ll 1$ holds, we have

$$\begin{aligned} J_1(k_0 r_s)/J_1'(k_0 r_s) &\approx k_0 r_s \\ Y_1(k_0 r_s)/Y_1'(k_0 r_0) &\approx -k_0^2 r_0^2 / k_0 r_s \\ J_1(k_0 r_s)/J_1'(k_0 r_0) &\approx k_0 r_s \\ Y_1'(k_0 r_s)/Y_1'(k_0 r_0) &\approx -k_0^2 r_0^2 / k_0^2 r_s^2 \\ J_1'(k_0 r_s)/J_1'(k_0 r_0) &\approx 1 \end{aligned}$$

Next the R.H.S. can be approximately expressed as

$$\text{R.H.S.} = \frac{\frac{\lambda_1 \rho_0}{k_0 \rho_s} \left[\frac{R_1(\lambda_1 r_s)}{J_1(\lambda_1 r_s)} \right] [k_0 r_s] - 1}{\frac{\lambda_1 \rho_0}{k_0 \rho_s} \left[\frac{R_1(\lambda_1 r_s)}{J_1(\lambda_1 r_s)} \right] [k_0 r_s] \left[-\frac{r_0^2}{r_s^2} \right] - \left[-\frac{r_0^2}{r_s^2} \right]}, \quad (5-15)$$

and the L.H.S. is

$$\text{L.H.S.} = \frac{\rho_e^+ - \rho_0}{\rho_e^+ + \rho_0}. \quad (5-16)$$

Combining with Eq. (5-15) and (5-16), a clearer form of effective mass density is

$$\frac{\rho_e^+ - \rho_0}{\rho_e^+ + \rho_0} = f \frac{\rho_s^+ - \rho_0}{\rho_s^+ + \rho_0}, \quad (5-17)$$

the mass density of the scatterers denotes

$$\rho_s^+ = \rho_s \left[\frac{J_1(\lambda_1 r_s)}{\lambda_1 r_s R_1(\lambda_1 r_s)} \right]. \quad (5-18)$$

Expanding Eq. (5-18) we get

$$\rho_s^+ = \rho_s \frac{(3W - \omega)(W + \omega) \cdot (2W - \omega)}{\omega \left\{ [2W^2 + (\omega - W)^2] \cdot \frac{\lambda_1 r_s J_1'(\lambda_1 r_s)}{J_1(\lambda_1 r_s)} - 3(\omega - W)W \right\}}. \quad (5-19)$$

In Fig. 5.2b, the function $\frac{\lambda_1 r_s J_1'(\lambda_1 r_s)}{J_1(\lambda_1 r_s)}$ in the region $|k_0| < 3$ is nearly equal to one. Therefore,

Eq. (5-19) surprisingly becomes a neat expression as

$$\begin{aligned} \rho_s^+ &\approx \rho_s \frac{(3W - \omega) \cdot (W + \omega) \cdot (2W - \omega)}{\omega \left\{ [2W^2 + (\omega - W)^2] - 3(\omega - W)W \right\}} \\ &= \rho_s \frac{(3W - \omega) \cdot (W + \omega) \cdot (2W - \omega)}{\omega \cdot (\omega^2 - 5\omega W + 6W^2)} \\ &= \rho_s \frac{(3W - \omega) \cdot (W + \omega) \cdot (2W - \omega)}{\omega \cdot (\omega - 3W) \cdot (\omega - 2W)} = \rho_s \left(1 + \frac{W}{\omega} \right). \end{aligned}$$

We thus have the form of mass density, which is given by

$$\rho_s^+ = \rho_s \left(1 + \frac{W}{\omega} \right) \quad (5-20)$$

In the same manner for $m = -1$, we get another mass density

$$\rho_s^- = \rho_s \frac{(3W + \omega) \cdot (W - \omega) \cdot (2W + \omega)}{-\omega \left\{ \left[2W^2 + (\omega + W)^2 \right] \cdot \frac{\lambda_{-1} r_s J'_{-1}(\lambda_{-1} r_s)}{J_{-1}(\lambda_{-1} r_s)} + 3(\omega + W)W \right\}}. \quad (5-21)$$

Similarly, in Fig. 5.2c the function $\frac{\lambda_{-1} r_s J'_{-1}(\lambda_{-1} r_s)}{J_{-1}(\lambda_{-1} r_s)}$ in the region $|k_0| < 3$ is nearly equal to 1 as

well. Eq. (5-21) becomes

$$\begin{aligned} \rho_s^- &\approx \rho_s \frac{(3W + \omega) \cdot (W - \omega) \cdot (2W + \omega)}{-\omega \left\{ \left[2W^2 + (\omega + W)^2 \right] + 3(\omega + W)W \right\}} \\ &= \rho_s \frac{(3W + \omega) \cdot (W - \omega) \cdot (2W + \omega)}{-\omega \cdot (\omega^2 + 5\omega W + 6W^2)} \\ &= \rho_s \frac{(3W + \omega) \cdot (W - \omega) \cdot (2W + \omega)}{-\omega \cdot (\omega + 3W) \cdot (\omega + 2W)} = \rho_s \left(1 - \frac{\Omega}{\omega} \right). \end{aligned}$$

We thus have the form of mass density, which is given by

$$\rho_s^- = \rho_s \left(1 - \frac{W}{\omega} \right) \quad (5-22)$$

The discrepancy of two densities is due to the fact non-reciprocity results from spinning cylinders. Eq. (5-12), (5-21), and (5-22) demonstrate a frequency-independent material can be turned into a dispersive medium while the rods are spinning. After homogenising by (5-10) and (5-17), the effective material parameters are denoted as

$$\frac{1}{B_e} = \frac{1}{B_0} \left(a_1 + \frac{a_2 W^2}{\omega^2 - W^2} \right), \quad \rho_e^\pm = \rho_0 \left(b_1 + \frac{b_2 W}{b_3 W \pm \omega} \right), \quad (5-23)$$

with

$$B_0 = \rho_0 c_0^2, \quad a_1 = \frac{B_0}{B_s} f + (1-f), \quad a_2 = \frac{B_0}{B_s} 3f,$$

$$b_1 = \frac{\rho_s + \rho_0 + f(\rho_s - \rho_0)}{\rho_s + \rho_0 - f(\rho_s - \rho_0)}, \quad b_2 = \frac{\rho_s [(1+f) - (1-f)b_1]}{\rho_s + \rho_0 - f(\rho_s - \rho_0)}, \quad b_3 = \frac{(1-f)\rho_s}{\rho_s + \rho_0 - f(\rho_s - \rho_0)}.$$

It is worth noting that, for static inclusions, $a_1 B_0^{-1} = \bar{B}^{-1}$ and $\rho_0 b_1 = \bar{\rho}$ are average bulk modulus and mass density whose expressions are consistent with ref. [88]. In addition, if one transforms the density terms of (5-23) into Cartesian coordinates, it results in an anisotropic density tensor written by

$$\vec{\rho}_s = \rho_0 \begin{pmatrix} b_1 + \frac{b_2 b_3 W^2}{b_3^2 \Omega^2 - \omega^2} & -i \frac{b_2 W \omega}{b_3^2 \Omega^2 - \omega^2} \\ i \frac{b_2 W \omega}{b_3^2 W^2 - \omega^2} & b_1 + \frac{b_2 b_3 W^2}{b_3^2 W^2 - \omega^2} \end{pmatrix}, \quad (5-24)$$

which formally coincide with the electromagnetic waves affected by ferrimagnetic materials, such as yttrium iron garnet (YIG) [73].

5-3: Pairs of Exceptional Rings

Once the expressions of dispersive media are decided, we can thus formulate the effective Hamiltonian by means of defining auxiliary variables [76]

$$\Pi = \left(\frac{a_2 W^2}{\omega^2 - W^2} \right) p, \quad -i a \Pi = \Theta, \quad \Lambda = \frac{b_2 W}{b_3^2 W^2 - \omega^2} \begin{bmatrix} b_3 W & -i \omega \\ i \omega & b_3 W \end{bmatrix} \mathbf{v}.$$

To make a symmetric Hamiltonian, auxiliary fields can be further reformulated by further defining: $\bar{c} = \sqrt{\bar{B}/\bar{\rho}}$, $\tilde{W} = W/\bar{c}$, $\tilde{\mathbf{v}} = \bar{\rho} \mathbf{v}$, $\tilde{p} = p/\bar{c}$, $\tilde{\Lambda} = \sqrt{\rho_0 \bar{\rho} b_3/b_2} \Lambda$, $\tilde{\Pi} = \Pi / (\bar{c} \sqrt{a_1 a_2})$, and

$\tilde{\Theta} = \Theta / (\bar{c}^2 \tilde{W} \sqrt{a_1 a_2})$. We can obtain an eigenvalue problem $(\omega/c_0)\mathbf{x} = \hat{\mathbf{H}}\mathbf{x}$ whose the eigenvector equals $\mathbf{x}^T = [\tilde{\mathbf{v}}, \tilde{\rho}, \tilde{\Lambda}, \tilde{\Pi}, \tilde{\Theta}]$ and its Hamiltonian reads

$$\hat{\mathbf{H}} = \frac{\bar{c}}{c_0} \begin{bmatrix} 0 & -i \frac{\rho_0 b_2}{\bar{\rho}} & k_x & 0 & i \sqrt{\frac{\omega_0 b_2 \rho_0}{\bar{\rho}}} & 0 & 0 \\ i \frac{\rho_0 b_2}{\bar{\rho}} & 0 & k_y & -i \sqrt{\frac{\omega_0 b_2 \rho_0}{\bar{\rho}}} & 0 & 0 & 0 \\ k_x & k_y & 0 & 0 & 0 & 0 & -i \sqrt{\frac{a_2}{a_1}} \\ 0 & i \sqrt{\frac{\omega_0 b_2 \rho_0}{\bar{\rho}}} & 0 & 0 & -ib_3 \tilde{W} & 0 & 0 \\ -i \sqrt{\frac{\omega_0 b_2 \rho_0}{\bar{\rho}}} & 0 & 0 & ib_3 \tilde{W} & 0 & 0 & 0 \\ 0 & 0 & 0 & 0 & 0 & 0 & i \tilde{W} \\ 0 & 0 & -i \sqrt{\frac{a_2}{a_1}} & 0 & 0 & -i \tilde{W} & 0 \end{bmatrix} \quad (5-25)$$

The off-diagonal terms in the above Hamiltonian consisting of b_i coefficients retain its Hermiticity because, as stated in (5-23), they can be considered as an analogue to the electromagnetic response in ferrites after applying static magnetic field. Yet, a_i coefficients conduct the non-Hermitian parts and they are relevant to the effective bulk modulus which possesses the effect of anti-resonance*. To reveal the underlying physics of the anti-resonance and non-Hermitian system, we review displacements expressed in (5-2). In the absence of

* Anti-resonance is a unique resonant effect which has an inverse phase jump in comparison with (normal) resonance. Generally, the anti-resonance effect originates from two coupled oscillators as destructive interference occurs under certain circumstances. A sole oscillator possessing anti-resonance is considered to be impossible due to the rule of causality. However, the anti-resonance feature has been observed in the presence of active materials because the rule of causality is valid only for passive media.

rotation, the azimuthal displacement u_θ vanishes when the index $m=0$ is considered. This corresponds to the fact that, around low-frequency, the eigenmode of the pressure wave is nearly acting as the isotropic oscillation along the radial direction. However, with a constant angular frequency W , the isotropic pressure distribution causes not only the displacement in radial direction but the one in azimuthal orientation. In other words, while rotation is introduced, both displacements u_r and u_θ are naturally coupled because of the Coriolis force. Additionally, the existence of centrifugal force generates an effective gain and loss as the cylinder rotates. During the compressional process, pressure waves propagate against the outward force caused by the centrifugal effect, which can be regarded as an effective loss. On the contrary, in the time of the dilation, the centrifugal force benefits this process so that it can be considered as the gain medium. As a result, with effective gain/loss terms from centrifugal effect and coupling from Coriolis effect, a PT symmetric system is physically expected.

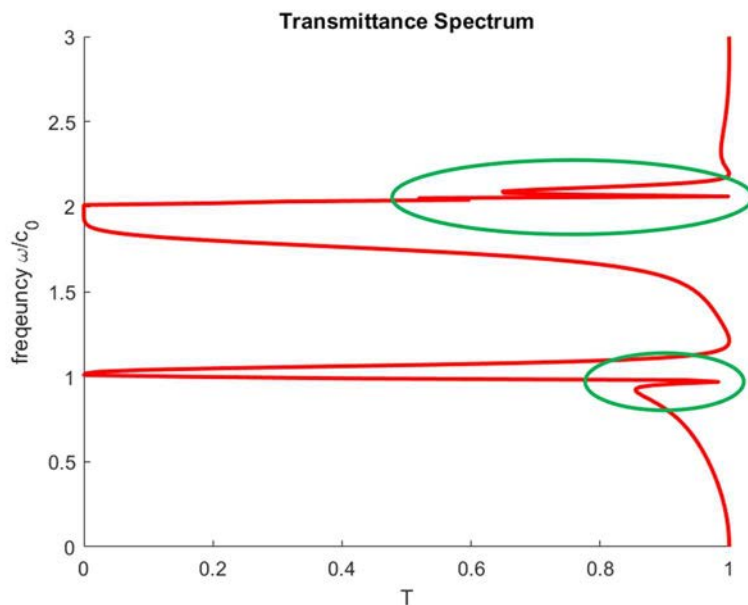


Fig. 5.3: Transmittance spectrum. The transmittance spectrum within the region $[0,3]$. The green circles highlight the Fano resonance peaks around the frequencies $\omega = W$ and $2W$.

Next, if one regards u_r and u_θ as two “oscillators”, the coupling between them would give rise to the anti-resonance characteristic, which has been proposed in other systems such as *RLC* circuits [73], coupled mechanics [89], and cavity QEDs [90]. In addition, this coupling

between two resonators leads to the phenomenon called ‘‘Fano resonance’’ that shows distinct resonant shapes comparing with conventional type of resonances [91]. In Fig. 5.3, we plot the transmittance spectrum illustrating Fano resonant peaks around frequency $\omega = W$ and $2W$. As stated in the literature [92], under certain circumstance it is possible for two coupled resonators to have anti-resonance. Thus, the rise of Fano mechanism can be considered as another angle of the generation of this unconventional asymmetric line shape. For the reason of non-Hermiticity, in accordance with the definition of bulk modulus $B = -V \partial P / \partial V$, the radial displacement u_r inside scatterers caused by the pressure from background directly contributes to the change of volume, yet u_θ plays no role to it. This makes acoustic metamaterials become an open system. Thus, an anti-Hermitian, or even asymmetric Hamiltonian originating from an open system is theoretically anticipated [93].

On the other hand, by testing commutation relation of PT operator, we further discuss in this section whether this acoustic metamaterial is PT symmetric or not, where P stands for parity symmetry flipping sign in real space (e.g., $\mathbf{r} \rightarrow -\mathbf{r}$) and T stands for time-reversal symmetry flipping sign in time ($t \rightarrow -t$). It should be noted that P does not account for 3D inversion. If so, the system will break PT symmetry. At the first glance, it seems that the effective Hamiltonian (5-25) is a non- PT symmetric system, since the matrix is formally asymmetric. On the contrary, this acoustic metamaterial preserves under PT symmetric operation. As a uniform rotating velocity $\mathbf{v}_0 = W r \hat{e}_\theta$, W changes sign under T operation but remains the same under P operation, i.e. $W(-\mathbf{r}, -t) = -W(\mathbf{r}, t)$. Apparently, the Hamiltonian (5-25) violates the commutator with either P or T operation. However, under the PT symmetric condition $H(\mathbf{p}, \mathbf{r}, t) = H^*(\mathbf{p}, -\mathbf{r}, -t)$ [39], it commutes with PT operator and leads to EPs while PT phase is broken.

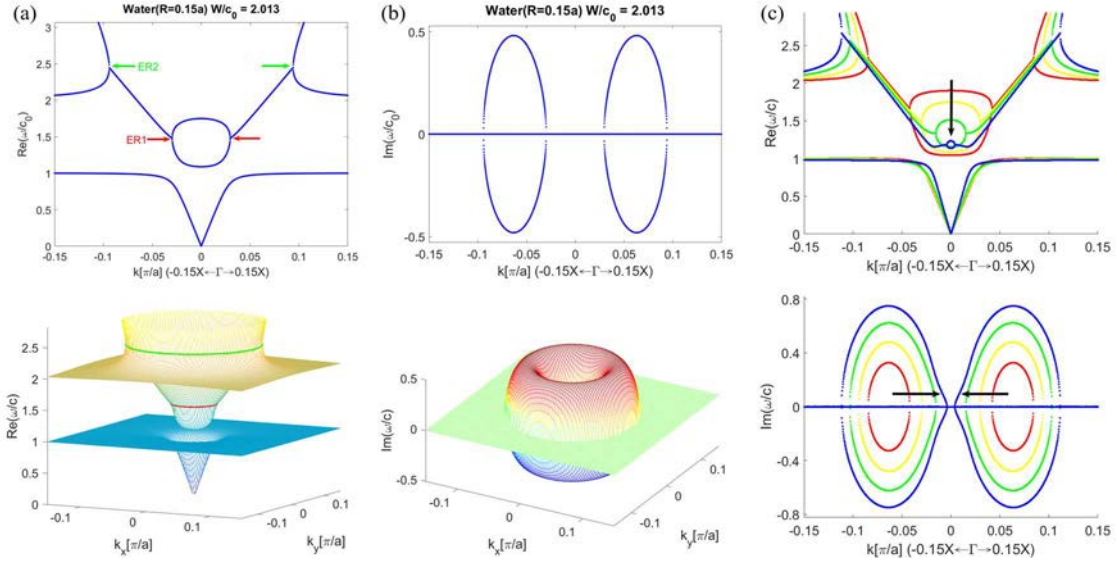


Fig. 5.4: A pair of ERs.(a) The real parts of a pair of exceptional rings calculated by the effective Hamiltonian. In the upper panel, the lowest band is similar to plasmonic dispersion exhibiting a resonant flat band. For second and third bands, the eigen-solutions predict the occurrence of band folding, matching the numerical results from MST. Apart from that, the red and green arrows indicate a pair of exceptional rings (ERs) where both the real and the imaginary parts are degenerate. 3D plots in lower panel give a clearer view of ER pair highlighted by red and green circles. (b) Two balanced imaginary parts are shown that implies a system with PT symmetry. In the lower panel, a torus of imaginary parts in the momentum space corresponds to the ER pair in (a). (c) Following the black arrows, the change band structure is given by tuning the radius from $0.1a$ to $0.25a$. The ER pair only moves in $k - \omega$ space as the radius increases.

Fig. 5.4a-b respectively show the real and imaginary part of eigen-frequencies resulted from solving Eq. (5-25). In Fig. 5.4a, the folding bands are connected between two ERs appearing around $(|\mathbf{k}|, \omega) = (0.030, 0.024)$ and $(0.094, 0.039)$ between the second and third bands. Fig. 5.4b shows an exotic donut-like imaginary distribution about the Brillouin zone centre. Within the PT broken region, the equivalent plus and minus imaginary parts provide another evidence of the existence of PT symmetry. Besides, when geometric parameters are tuned, the emergence of ER pairs exhibit the robustness against structure variances, since they are not spawned from the accidental Dirac degeneracy [42]. In Fig. 5.4c, we gradually increase the radius of cylinders from $0.1a$ to $0.25a$. The ER pairs remain regardless of the change of radius. Note that if the radius increases up to $0.3a$, the lowest region turns into a band gap. This stop band emerges because all propagating wavevectors \mathbf{k} are purely imaginary higher than this filling fraction.

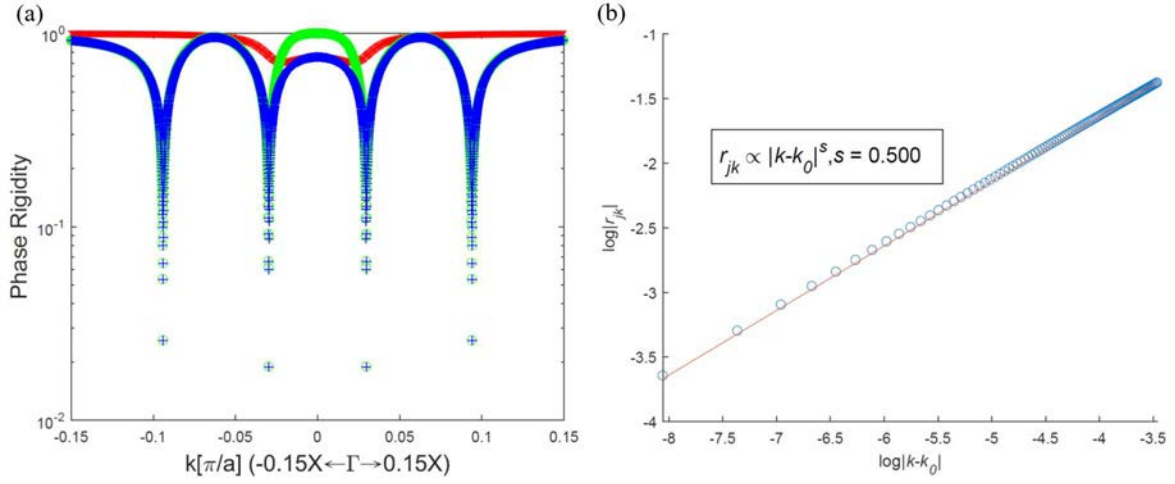


Fig. 5.5: Phase rigidity. (a) Phase rigidities of the states as a function of wavevectors for the first band (red), the second band (blue), and third band (green). Dips arising from the position of ERs are clearly shown. (b) The inset shows a log-log plot of phase rigidity versus $|k - k_0|$ for the exceptional points that indicate the order of EPs.

In addition, to clarify the order of singularity for ERs, a quantity r_{jk} called “phase rigidity” for all bands is defined as $r_{jk} = \langle \tilde{u}_{jk}^R | \tilde{u}_{jk}^R \rangle^{-1}$, where $|\tilde{u}_{jk}^R\rangle$ denotes the normalised right eigenstates [43]. Quantitative analysis provided by phase rigidity clarifies the mixing of two states near an exceptional point (EP). The magnitude of phase rigidity approaches zero near EPs in association with a power-law behaviour. For a normal-order (lowest-order) EP, it is well-known that the power order of the phase rigidity is 1/2; otherwise it is a high-order EP. Physically, a high-order EP results from the coalescence of several lower-order EPs. However, in our system the coalescence occurs only when the rotation vanishes. Owing to this conflict, it is unlikely for the proposed model to generate high-order ERs. To calculate the order, in Fig. 5.5a we plot the phase rigidity of all bands along the Brillouin boundary $\Gamma \rightarrow X$. Phase rigidities of the second and third bands merge and rapidly decrease to zero at $|\mathbf{k}| = 0.030$ as the phase rigidity for the states on the third and fourth bands merge and vanish at $|\mathbf{k}| = 0.094$. Fig. 5.5b illustrates the phase rigidity with log-log scale, and a slope of 1/2 is clearly shown.

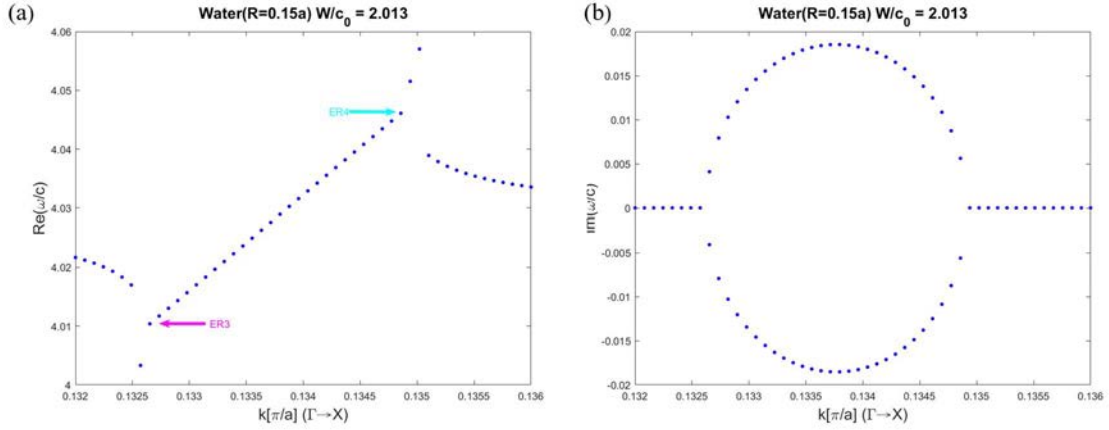


Fig. 5.6: Another pair of ERs. (a) An additional pair of exceptional rings located around $W/c_0 \sim 4$ and (b) its imaginary parts via scanning the complex frequency plane of Eq. (5-28).

If we take the region beyond the long-wavelength restriction into account, there exists additional ER pairs for high frequencies. Although above Hamiltonian is no longer valid in such region, one can have the dispersion relation expressed by

$$|\mathbf{k}|^2 = \frac{2\omega^2 \rho_e'^+ \rho_e'^-}{(\rho_e'^+ + \rho_e'^-) B_e'}, \quad (5-28)$$

where all the parameters have analytical forms given by the effective indices in ref. [75] rather than Eq. (5-23). As shown in Fig. 5.6a, after finding complex solution of Eq. (5-28), there is an extra ER pair near the real frequency $\omega/c_0 = 4$. As shown in Fig. 5.6b, an additional imaginary torus is illustrated. Despite the invalidity of long-wavelength limit, PT symmetry in the system retains so that a pair of symmetric imaginary part about k plane occurs which implies the mechanism of this ER pair is the same as preceding contents.

5-4: Chapter Summary

In summary, the pairs of ERs in acoustic metamaterials made by spinning rods has been studied. Resulting from anti-resonance in an open system, the asymmetric Hamiltonian leads

to interesting folded bands, and the complex dispersion relation exhibits multiple ERs between these bands around low-frequency region. Due to the fact $W(-r, -t) = -W(r, t)$, we construct P and TR symmetry operator and theoretically prove the Hamiltonian is PT symmetric. The corresponding eigenfrequency possessing a pair of balanced imaginary parts provides a solid evidence of a PT symmetric system. To verify the singularity of ERs, phase rigidity is introduced. Our result shows every ER has the lowest order 1/2 and unlikely merges into high-order ERs because of the resonance. Surprisingly, up to higher frequencies, extra pair of ERs is found even beyond the long-wavelength limit. In the final part, we introduce a feasible material and a possible experimental setup is proposed.

Chapter 6 Conclusion and Future Work

6-1: Conclusion

In summary, after outlining some essential background concepts, we theoretically proposed a mechanical crystal with honeycomb lattice that can possess topologically one-way edge states. The equations of motion are presented, and its band diagram shows, at K and K' points, several special degeneracies so-called Dirac points for mechanically vibrating modes. Likewise, as an infinitely long zigzag-edge strip with the identical geometry is taken into consideration, three types of edge states are found between energy bands. Furthermore, if the system is placed on a rotating frame, in the presence of Coriolis forces, TR symmetry will be broken, and then topologically non-trivial bandgaps are lifted. Within the non-trivial bandgap, topologically protected edge states can be observed in the projected band structure. On the other hand, if one initially stretches every spring with the same length, the pre-tension springs enables the mechanical crystals performs not only the original longitudinal but also transverse vibrations. After low-energy expansion around K points, the presence of transverse components can be considered as the effective Dresselhaus SOC term. By this extra contribution, spin-dependent wave-packet propagation is driven so that the elastic counterpart of spin-Hall effect is therefore observed.

In chapter four, we focused on the topological physics in periodically arranged elastic composites. Due to the decoupling of out-of-plane and in-plane modes in 2D elastic solids, we can be separately taken their phenomena into consideration. The out-of-plane modes, which is normally named as the pure shear modes, are mathematically equivalent to pressure acoustics and TE/TM electromagnetic fields since they are all governed by the same Helmholtz equation.

Therefore, by using ferrimagnetic rods as inclusions, we are able to generate topologically one-way transport of pure shear modes in elastic crystals. Apart from that, as the in-plane elastic modes are formed by coupled longitudinal and transverse components, the effective SOC terms emerge so long as one defines “spinor” as $\psi_{\pm} = (u_x \pm iu_y) / \sqrt{2}$. Moreover, through setting a zero-value bulk modulus, which implies $\lambda = -\mu$, two coupled elastic equations have the exactly same form in comparison with the 2D photonic topological insulators. Based on that, an elastic version of topological insulators is theoretically expected.

As presented in chapter three, rotation plays essential role in topological phenomena in classically vibrating waves. In chapter five we look further into the effect caused by rotation. Owing to the rotational Doppler effects, the frequencies across static and moving boundary are no longer the same. As a result, reconsidering the boundary condition originated from displacement continuity $u_1 = u_2$, the spinning non-dispersive material effectively transforms itself into a frequency-dependent one with respect to the angular velocity we apply. This rotation-induced-dispersive effect provides alternative approaches to realise acoustic metamaterials. Most interestingly, around the low-frequency region, effective medium theory shows there exists pairs of ERs with the unprecedented donut-like imaginary distribution. For the experimental realisation, we suggested a binary system made of spinning steel cylinders and water background that can be readily implemented in modern technology.

6-2: Future Work

In the future study, we plan to practically achieve theoretical predictions as proposed in preceding chapters. Firstly, the recent progress about effective SOC in mechanical systems [94] enable us to experimentally verify elastic spin-Hall effects. As shown in Fig. 6.1, every mass sphere hung by a string from top is properly connected by pre-tension springs in order to create

transverse components. By arranging the identical setup periodically, we can thus fabricate a mechanical graphene sample. Secondly, based on the results of realising 2D elastic topological insulator in Sec. 4-3. By setting $\lambda = -\mu$, 2D elastic topological insulators are anticipated. To experimentally verify it, the key step is to build up an effective bulk modulus whose has zero value around certain frequencies. Elastic metamaterials are applied in accordance with the results in ref. [75]. By means of filling soft matters like silicon rubbers in the porous structure, it is feasible to obtain zero-index bulk moduli on account of induced resonance.

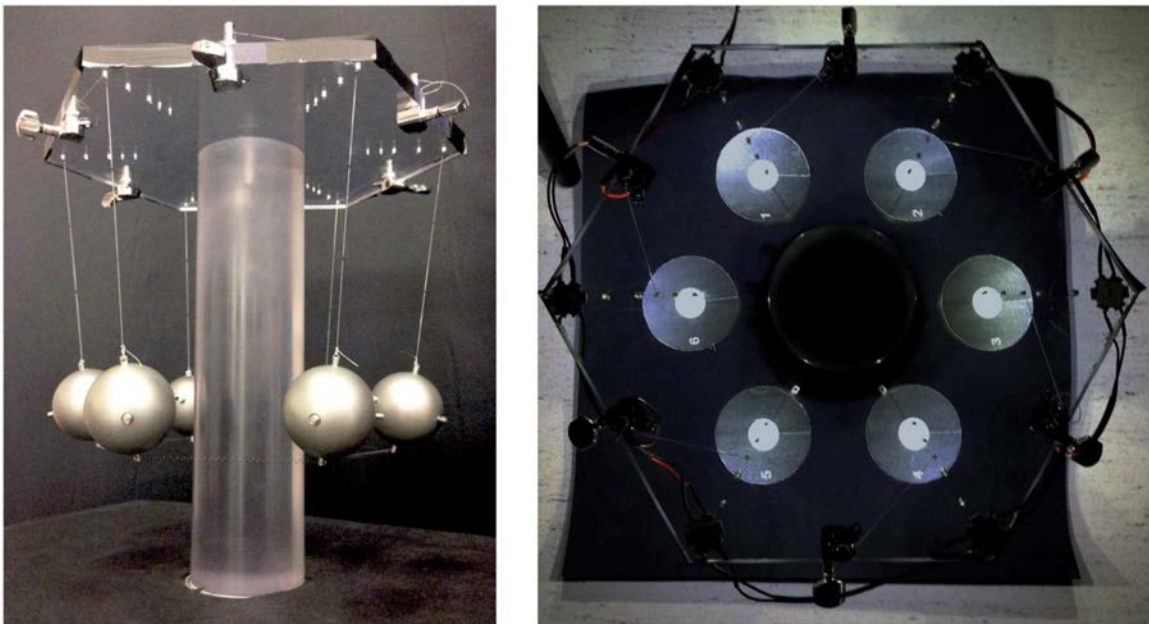


Fig. 6.1: A mechanical Benzene. The left figure demonstrates the experimental setup. The right figure is a snapshot while measuring the displacements of the pendula. [94]

Thirdly, we discuss the experimental realisation of the ER pairs. As stated in ref. [95-96], the shear waves are not negligible as the impedance contrast between inclusion and background is relatively small. Therefore, owing to its considerable contrast to background fluid, steel ($\rho = 7670 \text{ kg/m}^3$, $c = 6010 \text{ m/s}$) is a suitable candidate since we can treat the inclusion as fluid without loss of any generality. To implement Hamiltonian (5-25), it requires spinning steel rods which can be achieved by well-controlled electric motors. A suitable rotating speed range for our case roughly equals 3k-4k rad/s or 28k-38k rpm and it is commercially

supportable. Concerning the output power of motors, the lattice constant and the cylinder diameter is respectively set as 5 cm and 3 cm so as to construct lighter steel rods. The estimated wavelength in water is about 2 m as the angular velocity is set by 5k rad/s. At this structure scale, it is applicable for a $10 \times 3 \times 1$ m³ water tank to contain the entire acoustic metamaterial sample. In addition to the experimental realisation, the theoretical study regarding the physics within the PT broken region is still unclear. Unlike the conventional PT symmetric system, which is made of gain/loss coupled waveguides [97], the rotational PT symmetric effect arises from the occurrence of the centrifugal force. While the PT symmetry is broken, no enhanced transmitted wave is observed and that is different from the PT systems in optics. To study the phenomenon, we will apply the FDTD algorithm to see the instantaneous field pattern. Since the solutions in the broken PT region are complex conjugate pair of frequencies, a time-dependent algorithm can greatly help us reveal the underlying gain mechanism.

Apart from the practical observation discussed previously, here we suggest other possible studies of topological phenomena in classical vibration. Recent studies of phase modulations in elastic thin plates have provided a good platform to generate topologically one-way transport. Based on the Peierls substitutions, which replaces the hopping parameters by multiplying a phase factor, one can consider the system applied effectively by the uniform magnetic field via properly designing the structure of connections. However, normally the adjustment causes not only the change of phase factors but also the amplitude while the wave propagates through. This randomness of amplitudes will break topological phases such that it needs experiences regarding the structure engineering. In addition, the calculation of Chern numbers, which defines the topological order in the system, is tricky even though the formula has been long known for decades. The difficulty comes from the numerical calculation of eigenstates. Owing to the eigenfunction is gauge-dependent, every calculated eigenmode is

accompanied by an arbitrary phase so that it leads incorrect Chern numbers. To solve this problem, researchers proposed a replacement named “Wilson loops” whose expression is robust against the influence of random phases [98]. As my previous researches are highly linked to it, I have written a few programmes of Wilson loop calculation.

On the other hand, one of the main topics in topological physics is the search for Weyl [99] and Dirac points [100], but they have not yet been discovered in 3D elastic crystals. To find the topologically non-trivial degeneracies, the knowledge of group theory is required. Based on the group theory, a symmetry-protected degeneracy is guaranteed by the irreducible representation of little groups at certain high-symmetry points or lines. In accordance with the symmetry in real space, all these degeneracies can be sorted by its type of symmetry including universal symmetries (parity or time-reversal symmetry), point groups (symmorphic space group), and non-symmorphic space groups. Since the total number of space groups is 230, it is tedious but worth to categorise all the space groups in elastic crystals. Once the classification is built, it will make the search for Weyl or Dirac points become a straightforward task. Moreover, while considering non-symmorphic space groups, higher dimensional irreducible representations are generated that enables us to study the degeneracies beyond Weyl and Dirac points. Recent literature has shown that, in electronic crystals, there exist topologically non-trivial quasi-particles possessing the mathematic form distinguished from Weyl and Dirac equations. I believe similar phenomena can be observed in photonic and elastic crystals because both cases have plenty of degree of freedoms.

In addition to the topological elasticity, the topological mechanics is another thriving branch of topological physics. My studies have revealed that a periodic structure composed of simple springs and mass beads can achieve intriguing phenomena like topological mechanical edge states and the elastic spin-Hall effect. Other researchers have also shown the mechanical

crystals are capable of spawning mechanical Weyl points or topological insulating phases. For future works, I would like to introduce nonlinearity via replacing the linear springs with Kerr-type nonlinear ones. Since the Kerr nonlinearity can be related to the boson interaction in the quantum optics, it makes the mechanical crystal be equivalent to the strongly correlated electronic system, which is the origin of fractional quantum Hall states, and in the same manner, 2D topological mechanical solitons are intuitively expected. Unfortunately, it is unlikely to have commercial software that can emulate the nonlinear problems. Therefore, to solve problems, I plan to programme an iterating algorithm to look into the physics in nonlinear topological mechanics.

Bibliography

- [1] Klaus von Klitzing. "The quantised Hall effect." *Reviews of Modern Physics* 58.3 (1986): 519.
- [2] Hasan, M. Zahid, and Charles L. Kane. "Colloquium: topological insulators." *Reviews of Modern Physics* 82.4 (2010): 3045.
- [3] Xiao-Liang Qi and Shou-Cheng Zhang. "Topological insulators and superconductors" *Reviews of Modern Physics* 83.4 (2011): 1057.
- [4] AH Castro Neto, et al. "The electronic properties of graphene. " *Reviews of modern physics* 81.1 (2009): 109.
- [5] Charles L. Kane and Eugene J. Mele. "Quantum spin Hall effect in graphene." *Physical review letters* 95.22 (2005): 226801.
- [6] Charles L. Kane and Eugene J. Mele. " Z_2 topological order and the quantum spin Hall effect." *Physical review letters* 95.14 (2005): 146802.
- [7] F. D. M. Haldane and S. Raghu. "Possible realization of directional optical waveguides in photonic crystals with broken time-reversal symmetry." *Physical review letters* 100.1 (2008): 013904.
- [8] S. Raghu and F. D. M. Haldane. "Analogues of quantum-Hall-effect edge states in photonic crystals." *Physical Review A* 78.3 (2008): 033834.
- [9] Zheng Wang, et al. "Reflection-free one-way edge states in a gyromagnetic photonic crystal." *Physical review letters* 100.1 (2008): 013905.
- [10] Zheng Wang, et al. "Observation of unidirectional backscattering-immune topological electromagnetic states." *Nature* 461.7265 (2009): 772-775.
- [11] Alexander B. Khanikaev, et al. "Photonic topological insulators. " *Nature materials* 12.3 (2013): 233-239.
- [12] Mikael C. Rechtsman, et al. "Photonic Floquet topological insulators. " *Nature* 496.7444 (2013): 196-200.
- [13] Zhaoju Yang, et al. "Topological acoustics. " *Physical review letters* 114.11 (2015): 114301.
- [14] Yao-Ting Wang, Pi-Gang Luan, and Shuang Zhang. "Coriolis force induced topological order for classical mechanical vibrations. " *New Journal of Physics* 17.7 (2015): 073031.
- [15] Pai Wang, Ling Lu, and Katia Bertoldi. "Topological phononic crystals with one-way elastic edge waves. " *Physical review letters* 115.10 (2015): 104302.
- [16] Jairo Sinova, et al. "Spin hall effects." *Reviews of Modern Physics* 87.4 (2015): 1213.
- [17] Konstantin Y. Bliokh and Andrea Aiello. "Goos–Hänchen and Imbert–Fedorov beam shifts: an overview. " *Journal of Optics* 15.1 (2013): 014001.
- [18] Carl M. Bender and Stefan Boettcher. "Real spectra in non-Hermitian Hamiltonians having PT symmetry. " *Physical Review Letters* 80.24 (1998): 5243.
- [19] Carl M Bender, "Introduction to \mathcal{PT} -symmetric quantum theory." *Contemporary physics* 46.4 (2005): 277-292.

-
- [20] Christian E. Rüter, et al. "Observation of parity–time symmetry in optics." *Nature physics* 6.3 (2010): 192-195.
- [21] Eric W. Weisstein, "Gauss-Bonnet Formula." From *MathWorld*--A Wolfram Web Resource. <http://mathworld.wolfram.com/Gauss-BonnetFormula.html>
- [22] Figures are downloaded from the following URL: https://en.wikipedia.org/wiki/Hairy_ball_theorem
- [23] Michael V. Berry. "Quantal phase factors accompanying adiabatic changes." *Proceedings of the Royal Society of London A: Mathematical, Physical and Engineering Sciences*. Vol. 392. No. 1802. The Royal Society, 1984.
- [24] S. Pancharatnam, "Generalised Theory of Interference and Its Applications", *Proc. Ind. Acad. Sci.*, 44, 247 (1956)
- [25] J. Zak. "Berry's phase for energy bands in solids." *Physical review letters* 62.23 (1989): 2747.
- [26] Di. Xiao, Ming-Che Chang, and Qian Niu. "Berry phase effects on electronic properties." *Reviews of modern physics* 82.3 (2010): 1959.
- [27] D. J. Thouless, et al. "Quantised Hall conductance in a two-dimensional periodic potential." *Physical Review Letters* 49.6 (1982): 405.
- [28] Masatoshi Sato, et al. "Topology of Andreev bound states with flat dispersion." *Physical Review B* 83.22 (2011): 224511.
- [29] Kostya S. Novoselov, et al. "Electric field effect in atomically thin carbon films." *Science* 306.5696 (2004): 666-669.
- [30] A. Manchon, et al. "New perspectives for Rashba spin-orbit coupling." *Nature materials* 14.9 (2015): 871-882.
- [31] Gene Dresselhaus. "Spin-orbit coupling effects in zinc blende structures." *Physical Review* 100.2 (1955): 580.
- [32] Yu. A. Bychkov, and E. I. Rashba. "Properties of a 2D electron gas with lifted spectral degeneracy." *JETP lett* 39.2 (1984): 78.
- [33] F. Duncan M. Haldane. "Model for a quantum Hall effect without Landau levels: Condensed-matter realization of the" parity anomaly". " *Physical Review Letters* 61.18 (1988): 2015.
- [34] L. D. Landau and E. M. Lifshitz. *Course of Theoretical Physics Vol. 3 Quantum Mechanics*. Pergamon Press, 1958.
- [35] Liang Fu and Charles L. Kane. "Time reversal polarisation and a Z_2 adiabatic spin pump." *Physical Review B* 74.19 (2006): 195312.
- [36] Liang Fu, Charles L. Kane, and Eugene J. Mele. "Topological insulators in three dimensions." *Physical Review Letters* 98.10 (2007): 106803.
- [37] Haijun Zhang, et al. "Topological insulators in Bi_2Se_3 , Bi_2Te_3 and Sb_2Te_3 with a single Dirac cone on the surface." *Nature physics* 5.6 (2009): 438-442.
- [38] A. Guo, et al. "Observation of PT-symmetry breaking in complex optical potentials." *Physical Review Letters* 103.9 (2009): 093902.

-
- [39] Tsampikos Kottos. "Optical physics: Broken symmetry makes light work." *Nature Physics* 6.3 (2010): 166-167.
- [40] Xuefeng Zhu, et al. "P T-symmetric acoustics." *Physical Review X* 4.3 (2014): 031042
- [41] Ingrid Rotter. "A non-Hermitian Hamilton operator and the physics of open quantum systems." *Journal of Physics A: Mathematical and Theoretical* 42.15 (2009): 153001.
- [42] Bo Zhen, et al. "Spawning rings of exceptional points out of Dirac cones." *Nature* 525.7569 (2015): 354-358.
- [43] Kun Ding, et al. "Emergence, coalescence, and topological properties of multiple exceptional points and their experimental realization." *Physical Review X* 6.2 (2016): 021007.
- [44] Xueqin Huang, et al. "Dirac cones induced by accidental degeneracy in photonic crystals and zero-refractive-index materials." *Nature materials* 10.8 (2011): 582-586.
- [45] Wang, Yao-Ting, and Shuang Zhang. "Elastic spin-Hall effect in mechanical graphene." *New Journal of Physics* 18.11 (2016): 113014.
- [46] Yonatan Plotnik, et al. "Observation of unconventional edge states in 'photonic graphene'." *Nature materials* 13.1 (2014): 57-62.
- [47] Lev Davidovich Landau and E. M. Lifshitz. *Course of Theoretical Physics Vol. 1 Classical Mechanics*. Pergamon Press, 1958.
- [48] Bin Zhou. "Intrinsic anomalous Hall effect in spin-polarised two-dimensional electron gases with Dresselhaus spin-orbit interaction." *Physical Review B* 81.7 (2010): 075318.
- [49] Ming-Hao Liu and Ching-Ray Chang. "Anomalous spin Hall effects in Dresselhaus (110) quantum wells." *Physical Review B* 82.15 (2010): 155327.
- [50] Masaru Onoda, Shuichi Murakami, and Naoto Nagaosa. "Hall effect of light." *Physical review letters* 93.8 (2004): 083901.
- [51] Konstantin Yu Bliokh and Yury P. Bliokh. "Conservation of angular momentum, transverse shift, and spin Hall effect in reflection and refraction of an electromagnetic wave packet." *Physical review letters* 96.7 (2006): 073903.
- [52] Xiaobo Yin, et al. "Photonic spin Hall effect at metasurfaces." *Science* 339.6126 (2013): 1405-1407.
- [53] K. Yu Bliokh and V. D. Freilikher. "Polarisation transport of transverse acoustic waves: Berry phase and spin Hall effect of phonons." *Physical Review B* 74.17 (2006): 174302.
- [54] Alexey Kavokin, Guillaume Malpuech, and Mikhail Glazov. "Optical spin Hall effect." *Physical review letters* 95.13 (2005): 136601.
- [55] Charles Leyder, et al. "Observation of the optical spin Hall effect." *Nature Physics* 3.9 (2007): 628-631.
- [56] V. G. Sala, et al. "Spin-orbit coupling for photons and polaritons in microstructures." *Physical Review X* 5.1 (2015): 011034.
- [57] A. V. Nalitov, et al. "Spin-orbit coupling and the optical spin Hall effect in photonic graphene." *Physical review letters* 114.2 (2015): 026803.
- [58] Shuichi Murakami, Naoto Nagaosa, and Shou-Cheng Zhang. "Dissipationless quantum spin current at room temperature." *Science* 301.5638 (2003): 1348-1351.

-
- [59] Jairo Sinova, et al. "Universal intrinsic spin Hall effect." *Physical Review Letters* 92.12 (2004): 126603.
- [60] Y. K. Kato, et al. "Observation of the spin Hall effect in semiconductors." *Science* 306.5703 (2004): 1910-1913.
- [61] Lifa Zhang and Qian Niu. "Chiral phonons at high-symmetry points in monolayer hexagonal lattices." *Physical Review Letters* 115.11 (2015): 115502.
- [62] Toshikaze Kariyado and Yasuhiro Hatsugai. "Manipulation of Dirac Cones in Mechanical Graphene." *Scientific Reports* 5 (2015): 18107.
- [63] Riichiro Saito, G. Dresselhaus, and M. S. Dresselhaus. "Trigonal warping effect of carbon nanotubes." *Physical Review B* 61.4 (2000): 2981.
- [64] Sergey Konschuh et al. "Theory of spin-orbit coupling in bilayer graphene." *Physical Review B* 85.11 (2012): 115423.
- [65] Zhenhua Qiao, et al. "Microscopic theory of quantum anomalous Hall effect in graphene." *Physical Review B* 85.11 (2012): 115439.
- [66] Kejie Fang, Zongfu Yu, and Shanhui Fan. "Microscopic theory of photonic one-way edge state." *Physical Review B* 84.7 (2011): 075477.
- [67] Lev Davidovich Landau, and Eugin M. Lifshitz. *Course of Theoretical Physics Vol 7: Theory and Elasticity*. Pergamon Press, 1959.
- [68] Charles Kittel, "Interaction of spin waves and ultrasonic waves in ferromagnetic crystals." *Physical Review* 110.4 (1958): 836.
- [69] Ernst Schlömann, "Generation of Phonons in High-Power Ferromagnetic Resonance Experiments." *Journal of Applied Physics* 31.9 (1960): 1647-1656.
- [70] H. Matthews, and R. C. LeCraw. "Acoustic wave rotation by magnon-phonon interaction." *Physical Review Letters* 8.10 (1962): 397.
- [71] R. C. LeCraw and R. L. Comstock, "Magnetoelastic Interaction in Ferromagnetic Insulators," Chap. 4 in *Physical Acoustics*, Vol. IIIB, W. P. Mason, Ed., Academic Press, New York, (1965).
- [72] B. A. Auld, *Acoustic Fields and Waves in Solids*, Vol. I, p. 255, New York ; (Chichester): Wiley-Interscience (1973).
- [73] D. M. Pozar, *Microwave Engineering*, 4th ed., Wiley, New York, (2012).
- [74] Manvir S. Kushwaha, et al. "Theory of acoustic band structure of periodic elastic composites." *Physical Review B* 49.4 (1994): 2313.
- [75] Ying Wu, Yun Lai, and Zhao-Qing Zhang. "Effective medium theory for elastic metamaterials in two dimensions." *Physical Review B* 76.20 (2007): 205313.
- [76] Aaswath Raman, and Shanhui Fan. "Photonic band structure of dispersive metamaterials formulated as a Hermitian eigenvalue problem." *Physical review letters* 104.8 (2010): 087401.
- [77] Lev Davidovich Landau, and Eugin M. Lifshitz. *Course of Theoretical Physics Vol 6: Fluid Mechanics*. Pergamon Press, 1959.

-
- [78] Richard A. Shelby, David R. Smith, and Seldon Schultz. "Experimental verification of a negative index of refraction." *Science* 292.5514 (2001): 77-79.
- [79] Xiang Zhang, and Zhaowei Liu. "Superlenses to overcome the diffraction limit." *Nature materials* 7.6 (2008): 435-441.
- [80] Xingjie Ni, et al. "An ultrathin invisibility skin cloak for visible light." *Science* 349.6254 (2015): 1310-1314.
- [81] Shuang Zhang, et al. "Plasmon-induced transparency in metamaterials." *Physical Review Letters* 101.4 (2008): 047401.
- [82] Nicholas Fang, et al. "Ultrasonic metamaterials with negative modulus." *Nature materials* 5.6 (2006): 452-456.
- [83] Ping Sheng, et al. "Dynamic mass density and acoustic metamaterials." *Physica B: Condensed Matter* 394.2 (2007): 256-261.
- [84] Zhengyou Liu, et al. "Locally resonant sonic materials." *Science* 289.5485 (2000): 1734-1736.
- [85] Jensen Li, and C. T. Chan. "Double-negative acoustic metamaterial." *Physical Review E* 70.5 (2004): 055602.
- [86] D. Censor, and J. Aboudi. "Scattering of sound waves by rotating cylinders and spheres." *Journal of Sound and Vibration* 19.4 (1971): 437-444.
- [87] Martin PJ Lavery, et al. "Detection of a spinning object using light's orbital angular momentum." *Science* 341.6145 (2013): 537-540.
- [88] Ying Wu, et al. "Effective medium theory for magnetodielectric composites: Beyond the long-wavelength limit." *Physical Review B* 74.8 (2006): 085111.
- [89] F. Wahl, G. Schmidt, and L. Forrai. "On the significance of antiresonance frequencies in experimental structural analysis." *Journal of Sound and Vibration* 219.3 (1999): 379-394.
- [90] Christian Sames, et al. "Antiresonance phase shift in strongly coupled cavity QED." *Physical review letters* 112.4 (2014): 043601.
- [91] Boris, Luk'yanchuk, et al. "The Fano resonance in plasmonic nanostructures and metamaterials." *Nature materials* 9.9 (2010): 707-715.
- [92] Andrey E. Miroshnichenko, Sergej Flach, and Yuri S. Kivshar. "Fano resonances in nanoscale structures." *Reviews of Modern Physics* 82.3 (2010): 2257.
- [93] Shuang Zhang, et al. "Anti-Hermitian plasmon coupling of an array of gold thin-film antennas for controlling light at the nanoscale." *Physical review letters* 109.19 (2012): 193902.
- [94] Grazia Salerno, et. al. "Spin-orbit coupling in a hexagonal ring of pendula." *New Journal of Physics* 19 (2017): 055001.
- [95] Jun Mei, et al. "First-principles study of Dirac and Dirac-like cones in phononic and photonic crystals." *Physical Review B* 86.3 (2012): 035141.
- [96] M. Kafesaki, and Eleftherios N. Economou. "Multiple-scattering theory for three-dimensional periodic acoustic composites." *Physical review B* 60.17 (1999): 11993.
- [97] Christian E. Rüter, et al. "Observation of parity-time symmetry in optics." *Nature physics* 6.3 (2010): 192.

-
- [98] Rui Yu, et al. "Equivalent expression of Z_2 topological invariant for band insulators using the non-abelian Berry connection. " *Physical Review B* 84.7 (2011): 075119.
- [99] Su-Yang Xu, et al. "Discovery of a Weyl fermion semimetal and topological Fermi arcs. " *Science* 349.6248 (2015): 613-617.
- [100] Z. K. Liu, et al. "Discovery of a three-dimensional topological Dirac semimetal, Na_3Bi . " *Science* 343.6173 (2014): 864-867.